Satellite Cloud Property Retrieval in the O_2 A Band

Inclusion of Cloud Vertical Extinction Profiles

Sören Testorp

12.06.2018

Sören Testorp

Satellite Cloud Property Retrieval in the O_2 A Band - Inclusion of Cloud Vertical Extinction Profiles

Dissertation

12. Juni 2018

Betreuer: Prof. Dr. Jürgen Fischer

Freie Universität Berlin

Institut für Weltraumwissenschaften

Carl-Heinrich-Becker-Weg 6-10

12165 and Berlin

Freie Universität Berlin

Institut für Weltraumwissenschaften

Satellite Cloud Property Retrieval in the O_2 A Band - Inclusion of Cloud Vertical Extinction Profiles

Dissertation

zur Erlangung des akademischen Grades eines
Doktors der Naturwissenschaften
am Fachbereich für Geowissenschaften
der Freien Universität Berlin

Sören Testorp

1. Reviewer	Prof. Dr. Jürgen Fischer Institut für Weltraumwissenschaften Freie Universität Berlin
2. Reviewer	Prof. Dr. Ralf Bennartz Earth and Environmental Sciences Vanderbilt University
Betreuer	Prof. Dr. Jürgen Fischer
Dissertation	12. Juni 2018
Tag der Disputation	18. Juli 2018

Selbständigkeitserklärung

Hiermit erkläre ich an Eides statt, dass ich die vorliegende Arbeit selbständig und ohne fremde Hilfe angefertigt, keine anderen als die angegebenen Quellen und Hilfsmittel benutzt und die den benutzen Quellen wörtlich oder inhaltlich entnommenen Stellen als solche kenntlich gemacht habe. Diese Arbeit hat in gleicher oder ähnlicher Form noch keiner Prüfungsbehörde vorgelegen.

Berlin, 12. Juni 2018

Sören Testorp

Abstract

Clouds play a vital role in the Earth's energy balance through their interaction with radiation. Depending on the cloud properties the net effect on the climate can be either cooling or warming. In order to assess the role of clouds in a changing climate long-term measurement of clouds on a global scale are necessary. Satellite remote sensing meets the requirements to deliver such data sets, resulting in long term climate data records including more than 30 years of satellite measurements.
In this work the O_2 A band technique for the retrieval of cloud properties will be studied in regard to the vertical extinction profile of clouds. Therefore, a sensitivity study is performed, which focuses on the influence of cloud vertical extinction profiles towards the satellite measured signal. A parametrization of the vertical profile, decomposed into extent and distribution of cloud optical depth (mode), is introduced, leading to a measurement algorithm with four retrievable parameters: cloud top pressure/height, cloud optical depth, cloud vertical extent and distribution of cloud optical depth/mode.
The signal sensitivity is, for both newly introduced parameters, of a similar magnitude as for the cloud top height. However, the analysis of degree of freedom demonstrates that a simultaneous retrieval of all four variables is not feasible.
Further, a preprocessor to the cloud property retrieval is developed with the purpose to support the retrieval through better a priori knowledge of the measurement. Therefore, the texture of an imager pixel and its vicinity is analysed using the grey-level co-occurrence method. In a second step the derived textural features are utilized in a random forest classifier to assign a class, which is either based on classical cloud types or discrete groups of cloud vertical extent or mode.
On top of that, the newly developed cloud property retrieval was evaluated with the help of cloud radar measurements in the form of a case study. Special focus was on the quality of the retrieved cloud parameters under differing restraints for the retrieval. The impact of a priori known cloud top heights was compared to cases of no a priori knowledge and a retrieval with non-variable cloud vertical extinction profile. Here, the technique shows promising results for the retrieval of cloud vertical

extinction profiles, when the cloud top height is known from the start.
Also, a validation study regarding the top of atmosphere flux retrieval included in CC4CL against CERES measurements was performed, showing the impact of differing cloud properties on the retrieved fluxes.
Overall, this work studies the significant impact of vertical extinction profiles on the retrieval of cloud top heights as well as the possibility of a derivation of said profiles through passive remote sensing instruments.

Zusammenfassung

Wolken spielen, durch ihre Interaktion mit Strahlung, eine wichtige Rolle in der Energiebalance der Erde. Ob der Effekt von Wolken auf das Klima kühlend oder wärmend ist, hängt dabei von den jeweiligen Wolkeneigenschaften ab. Um die Auswirkungen von Wolken im Klimawandel zu beurteilen sind globale, Langzeitmessungen notwendig. Die Satellitenfernerkundung ist in der Lage diese Zeitreihen zu liefern, was bereits zu Klimadatensätzen geführt hat die mehr als 30 Jahre an Satellitenmessungen beinhalten.

In dieser Arbeit wird die Methode zur Ableitung von Wolkeneigenschaften mithilfe der O_2 A Bande untersucht, vor allem hinsichtlich des Einflusses des vertikalen Extinktionsprofils der Wolke.

Dafür wird zunächst eine Sensitivitätsstudie durchgeführt, die speziell den Einfluss der vertikalen Verteilung der Wolke hinsichtlich des Messsignals am Oberrand der Atmosphäre untersucht. Das Vertikale Profil wird dafür parametrisiert dargestellt durch die vertikale Ausdehnung der Wolke und die Verteilung der optischen Dicke.

Zeitgleich wird ein neues Ableitungsverfahren eingeführt, das im Gegensatz zum Klassischen O_2 A Band verfahren vier Parameter bestimmt: den Wolkenoberkantendruck, die optische Dicke, die vertikale Ausdehnung und die Verteilung der optischen Dicke dargestellt durch die Mode.

Hierbei zeigt sich, dass die Sensitivität des Signals zu den neu eingeführten Parametern eine ähnliche Größenordnung aufweist wie zum Wolkenoberkantendruck. Jedoch zeigt die Untersuchung der Freiheitsgrade, dass nicht alle vier Variablen mit dieser Methode gleichzeitig bestimmt werden können.

Außerdem wurde ein Präprozessor entwickelt, der das neue Ableiteverfahren mit besseren a priori Wissen über die Messung unterstützen soll. Dafür wird für jeden Messpunkt und seine direkte Umgebung eine Texturanalyse mithilfe der Grauwertematrix-Methode durchgeführt. Die somit erhaltenen Textureigenschaften dienen als Eingabe für einen "Random-Forest" Klassifikator, der jeder Messung eine Klasse zuweist, die entweder auf klassischen Wolkentypen basiert oder durch diskrete Werte von vertikaler Ausdehnung oder Mode gegeben ist.

In einem nächsten Schritt wird das neue Ableiteverfahren für Wolkeneigenschaften unter Zuhilfenahme von Messungen eines satellitenbasierten Wolkenradars evaluiert. Vor allem wird hierbei das Augenmerk auf die Qualität der abgeleiteten Wolkenparameter für verschiedene Einschränkungen des Verfahrens gerichtet. Dafür wird zum einen die Höhe der Wolkenoberkante durch das a priori Wissen als bekannt vorausgesetzt, zum anderen wird das Verfahren mit nur zwei veränderlichen Parametern

durchgeführt, indem die Variabilität des vertikalen Profils entfernt wird. Als dritte Variante wird das Ableiteverfahren ohne Einschränkungen und Vorwissen durchgeführt. Die Ableitung des vertikalen Extinktionsprofils zeigt dabei vielversprechende Ergebnisse falls die Wolkenoberkantenhöhe vorher bereits bekannt ist.
Außerdem werden die Strahlungsflüsse, die durch das Verfahren von CC4CL hergeleitet werden, am Oberrand der Atmosphäre mit CERES Messungen validiert. Dabei wird der Einfluss von unterschiedlichen Wolkenprodukten auf die Ableitung von globalen Strahlungsflüssen verdeutlicht.
Insgesamt handelt diese Arbeit von dem Einfluss vertikaler Wolkenextinktionsprofile auf die Ableitung von Wolkenoberkantendrücken, verbunden mit der Untersuchung nach einer Ableitung jener Profile mit Satellitenfernerkundungsmessungen.

Contents

1 Introduction **1**

1.1 Earth's Energy Budget 1
1.2 Representation of Clouds in Climate Models 3
1.3 Climate Data Records 6
1.4 Thesis Outline 7

2 Fundamentals **9**

2.1 Satellite Remote Sensing 9
2.1.1 MODIS 10
2.1.2 Cloud Profiling Radar 10
2.1.3 CALIOP 11
2.1.4 AATSR 11
2.1.5 MERIS 12
2.1.6 OLCI 12
2.2 Radiative Transfer Equation 13
2.3 Mie-Theory and Cloud properties 15
2.4 Radiative Transfer Model 19
2.5 O_2 A Band retrieval 21
2.6 Inverse Problem 24

3 Sensitivity Study **27**

3.1 Parametrization of Vertical Extinction Profile 27
3.2 Jacobian and Sensitivity 29
3.3 Radiative Transfer Simulation 30
3.4 Central Wavelength of the Instrumental Channels 32
3.5 Cloud Vertical Extinction Profile 36
3.6 Degrees of Freedom 41
3.6.1 Central Wavelength and Cloud Top Pressure 42
3.7 Conclusion 44

4 Classification of Clouds based on Texture Analysis **47**
4.1 Introduction . . . 47
4.2 Method . . . 48
4.2.1 Grey-Level Co-Occurrence Matrix . . . 49
4.2.2 Random Forest Classification . . . 50
4.3 Data Basis . . . 51
4.4 Analysis . . . 53
4.4.1 Window Size and Resolution . . . 54
4.4.2 Maximum Number of Grey-Levels . . . 56
4.4.3 Inter-Pixel Distance . . . 57
4.4.4 Importance of Texture Features . . . 58
4.4.5 Classification into Cloud Types . . . 59
4.4.6 Estimating Cloud Vertical Extinction Profile . . . 60
4.5 Impact of Surface Types . . . 64
4.6 Conclusions . . . 67

5 Intercomparison of Cloud Property Retrievals and Evaluation of an OLCI Prototype Algorithm **71**
5.1 Cloud Top Pressure Retrieval . . . 71
5.2 Validation of FAME-C . . . 72
5.2.1 Validation of Cloud Fraction . . . 74
5.2.2 Validation of Cloud Top Height . . . 75
5.3 Evaluation of OLCI Cloud Retrieval . . . 78
5.3.1 Qualitative Analysis of OLCI Cloud Properties . . . 79
5.3.2 Points of Non-Convergence . . . 85
5.3.3 Quantitative Evaluation of Cloud Properties . . . 86
5.4 Conclusion . . . 90

6 Validation of CC4CL Top of Atmosphere Fluxes **93**
6.1 CERES . . . 93
6.2 CC4CL & BUGSrad . . . 94
6.3 Point Spread Function . . . 94
6.4 Shortwave and Longwave TOA Annual Means . . . 96
6.5 TOA Instantaneous Shortwave and Longwave Fluxes . . . 100
6.6 Summary . . . 103

7 Summary & Outlook **105**

A Appendix **109**

Bibliography 117

List of Figures 131

List of Tables 139

Danksagung 141

1 Introduction

> *Warming of the climate system is unequivocal, and since the 1950s, many of the observed changes are unprecedented over decades to millennia. The atmosphere and ocean have warmed, the amounts of snow and ice have diminished, sea level has risen, and the concentrations of greenhouse gases have increased.*
>
> **— IPCC 2013**
> (Summary for Policy Makers)

The warming of Earth's atmosphere, due to rise in anthropogenic greenhouse gases, has various effects which can not be ignored. Changes in weather systems can lead to the destruction of ecosystems, coupled with extinction of animal and plant species. Regional food and water shortages and natural disasters are possible outcomes.
In the last decades monitoring climate change and understanding the driving factors has become one of the most important tasks for earth observation scientist worldwide.

1.1 Earth's Energy Budget

Ideally, the Earth is in an equilibrium of incoming and outgoing radiation and connected with it thermal energy. When this equilibrium is disturbed by human actions, less energy is emitted from Earth than is incoming from the sun, causing a warming of the coupled earth-atmosphere-system. In the last decades, satellite based instruments Earth Radiation Budget Experiment (ERBE, Barkstrom et al. (1990)), Scanning Radiometer for Radiation Balance (ScaRab, Kandel et al. (1998)) and Clouds and the Earth's Radiant Energy System (CERES, Wielicki et al. (1996)) monitored the Earth's energy budget, increasing the knowledge about the driving forces of climate. A recent study by Stephens et al. (2012) determined the annual mean

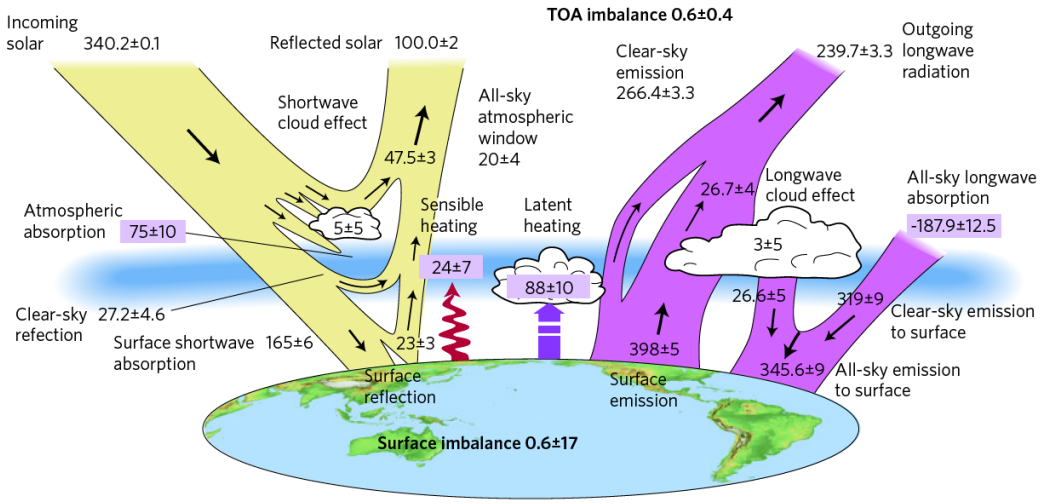

Fig. 1.1.: Global annual mean energy budget of Earth for the years 2000-2010. All fluxes are in W/m^2 (Stephens et al., 2012).

global imbalance of the energy budget, based on the years 2000-2010, to be at $(0.6 \pm 0.4)W/m^2$, which was inferred from ocean heat content (OHC) information. That means, on average $0.6W/m^2$ more radiative energy enters the Earth's system than is emitted. The detailed radiative fluxes are presented in figure 1.1. The imbalance is constructed of the total incoming solar radiation ($340.2W/m^2$) minus the reflected solar ($100W/m^2$) and the outgoing longwave radiation ($239.7W/m^2$). The total uncertainty of satellite measured top of atmosphere (*TOA*) fluxes is around $\pm 4W/m^2$, which mainly is a result from calibration errors of the associated instruments and is nearly 10 times the magnitude of the imbalance from OHC.

Clouds play an important role for the energy balance of the Earth. They cover around 70% of the globe at all times (Stubenrauch et al. (2013): 68%; Wylie et al. (2005): 75%) and impact transport of heat in the atmosphere and ocean as well as being a major part in the earth's hydrological cycle trough condensation and precipitation of water vapour. Due to their high reflectivity in the visible spectrum, they are responsible for $47.5W/m^2$ (or 47.5%) of the directly reflected shortwave radiation, which is called the cloud albedo effect. However, clouds also trap longwave radiation in the atmosphere, which is their greenhouse effect with a mean annual magnitude of $26.7W/m^2$. The greenhouse effect is determined through difference between the outgoing radiation without clouds (clear-sky) and the outgoing radiation in the presence of clouds (all-sky). In total, clouds are estimated to reduce the Earth's energy budget by $-21.1W/m^2$ and thus have a cooling effect on the Earth's system. This is called the cloud radiative forcing (CRF) or cloud radiative effect (CRE). The

CRF of each individual cloud is dependent on its properties. Optical properties of a cloud are generally described by the following parameters:

- cloud top and bottom heights/pressure/temperature
- cloud optical thickness
- cloud liquid/ice water path
- cloud droplet effective radius
- cloud thermodynamic phase
- cloud fraction/cover

Regarding the global radiation budget, high and optically thin clouds have a warming effect on the atmosphere. Clouds emit radiation as a black body, i.e. the emitted energy is dependent on the temperature of the cloud. Thermal radiation from the surface is absorbed by clouds and due to their low temperature high clouds re-emit less thermal radiation into space. Low clouds on the other hand have a temperature closer to the surface temperature and therefore posses a similar thermal emission as the surface. Additionally, low clouds often have a higher optical depth, which is the decisive property for the amount of reflected shortwave radiation. Ramanathan et al. (1989) used ERBE measurements and found, that the CRF can reach values of $50 - 100 W/m^2$ in regions with extensive cirrus clouds. Additionally, their study showed that the cloud radiative effect can exceed $-100 W/m^2$ in the mid-latitudes for regions with deep convective clouds and extensive stratus decks. Hence, longwave radiative forcing is mainly determined by the cloud height, while the shortwave CRF is a function of the ice- and water content of the clouds. It is still uncertain how the changing climate affects the distribution and properties of clouds on a global change.

1.2 Representation of Clouds in Climate Models

An important tool to understand and predict climate change are global climate models (GCM). However, the representation of clouds and their processes in GCMs

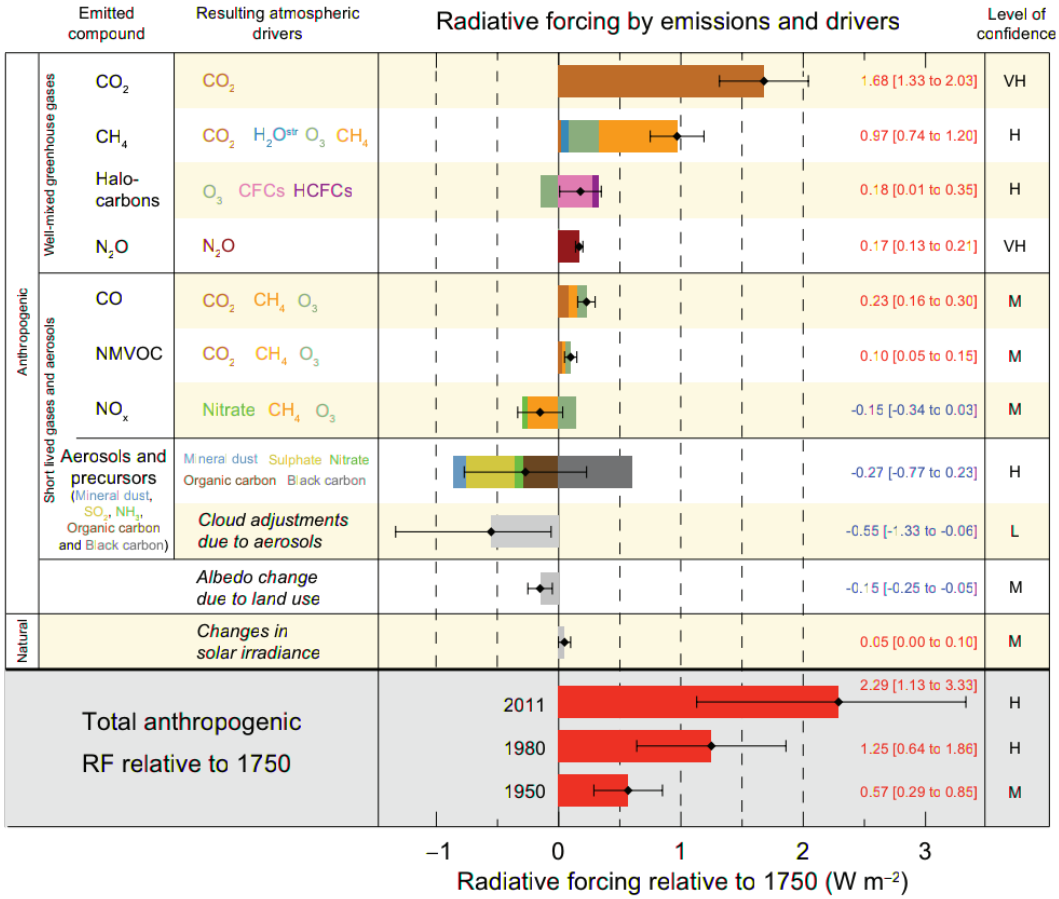

Fig. 1.2.: IPCC AR5: Global average radiative forcing estimates for 2011 relative to 1750. The cloud adjustments due to aerosols form the largest uncertainty in the determined radiative forcing (IPCC, 2013).

are still a source for uncertainty. Usually, global climate model have a horizontal spatial resolution of 100km, while clouds can vary considerably on a much smaller scale. Thus, cloud processes cannot be resolved by those models and have to be included by parametrizations. Gleckler et al. (1995) found, that the poor resolution of clouds leads to inaccuracies in the poleward transport of heat in the ocean for numerous climate models, i.e. the implementation of parametrizations is decisive for the performance of the model. Here, the global coverage of cloud measurements provided by satellites is vital for improving the representation of cloud processes in models.

Another problem of clouds in models is the poor representation of vertical distribution. Passive satellite sensors only provide optical cloud properties as an integral over the atmospheric column, but the vertical distribution of clouds and therefore radiant

energy is important information for climate models. Since 2006, the Cloud-Aerosol Lidar and Infrared Pathfinder Satellite Observation (CALIPSO) and the CloudSat mission provide near global coverage of vertical profiles of clouds and aerosols. Taking advantage of this unprecedented information, the vertical distribution of hydrometeors in models is evaluated in several studies (Stein et al. (2015), Bodas-Salcedo et al. (2011), Naud et al. (2010)). Presently, both mission are far beyond their planned lifetime of 22 months for CloudSat and 36 months for CALIPSO and are coming to an end. Since February 2018 CloudSat is no longer operational, prohibiting the availability of vertical profiles of the atmosphere from combined lidar and cloud radar measurements. Therefore, it is of interest to develop techniques using the numerous passive imagers orbiting Earth to retrieve vertically resolved climate data.

Another source for uncertainties in models is the interaction between clouds and aerosols, known as the aerosol indirect effect. The aerosol indirect effect can be separated into two contributors. The first aerosol indirect effect refers to the increase of low level cloud albedo due to an increase of cloud droplet numbers coupled with a decrease in droplet radii, caused by aerosol contamination providing an increased number of condensation nuclei (Twomey, 1977). The second aerosol indirect effect describes the change in precipitation characteristics caused by the increased cloud droplet number and the accompanied change in liquid water path, cloud lifetime and cloud cover (Albrecht, 1989). According to the Intergovernmental Panel on Climate Change (IPCC, 2013) the aerosol-cloud radiative forcing is the most uncertain parameter when considering climate change, with a net effect of $-0.55W/m^2$ and an uncertainty ranging between $-1.33W/m^2$ and $0W/m^2$ (see fig. 1.2).
Another, much discussed topic are feedback effects in global climate models. A feedback effect is here defined as a change in an atmospheric parameter caused by the increase in global mean surface temperature, which entails an amplification or attenuation of said temperature change. For some climate variables the GCMs agree in the sign of the feedback, whether positive or negative, e.g. for the increase in water vapour due to rising global mean surface temperatures. Water vapour is a greenhouse gas and rising concentrations in the atmosphere will have a positive effect on Earth's radiation budget, i.e. increase in the rate of warming. Similarly, the shrinking of Earth's cryosphere leads to less reflected shortwave radiation, further increasing the temperatures. The impact of other atmospheric properties on the global mean temperature response, differs between GCMs. The temperature lapse rate in the troposphere can have either a positive or negative feedback depending on the vertical distribution of the atmospheric warming. For example, if the upper levels of the troposphere experiences a stronger warming than the lower levels, the

radiative feedback will be negative, since the emission of longwave radiation into space will be more effective. Regarding clouds, the value of the feedback effect can be either positive or negative depending on the caused changes in cloud properties by an increase in global mean temperature, which are still uncertain. As mentioned in section 1.1, an increase in global mean cloud height would lead to a positive feedback, whereas an increase in mean cloud albedo contributes to negative radiative forcing. Moreover, the magnitudes of the mentioned feedback effects show large spreads in climate models, which was studied by Colman (2003). Therefore, the feedback effects in several global circulations models were examined and the standard deviation of some feedback effects was found to be at 120% (for the lapse rate) of the mean feedback value, including changes in the sign for cloud and lapse rate feedback.

1.3 Climate Data Records

Improvement of climate models is largely based on insights in atmospheric processes gained by satellite measurements. Especially, sustained satellite observations are important to find tendencies in data and constraint models with realistic feedback mechanisms. To identify reliable climate trends the quality of the time-series has to be consistent. Stability inside long-term satellite climate data records is the decisive property, causing several challenges. On the one hand, single satellite data records often only cover time spans of up to 10 years, which can be to short a period to indentify climate trends. On the other hand, climate variable data sets from several satellites have to overcome the difficulties of intercalibration, degradation of the satellites over time, different orbit overpass times (including orbital drifts during the satellite lifetimes) and spatial resolutions as well as alternative retrieval techniques. Several projects are working towards creation of such long-term climate data records. International Satellite Cloud Climatology Project (ISCCP) started in 1983 with the aim "to collect and analyze satellite radiance data to infer the global distribution of cloud radiative properties in order to improve the modeling of cloud effects on climate" (Rossow and Schiffer, 1999). ISCCP provides spatially averaged data on various grid sizes (for clouds: 30km mapped pixel as well as 280km equal-area grid) with 3-hourly or monthly temporal resolutions depending on the product.
The creation of long time series of essential climate variables (ECVs) is also the aim of the European Space Agency's Climate Change Initiative (ESA_CCI) (Hollmann et al., 2013). For 13 out of 50 ECVs, defined by the Global Climate Observing System

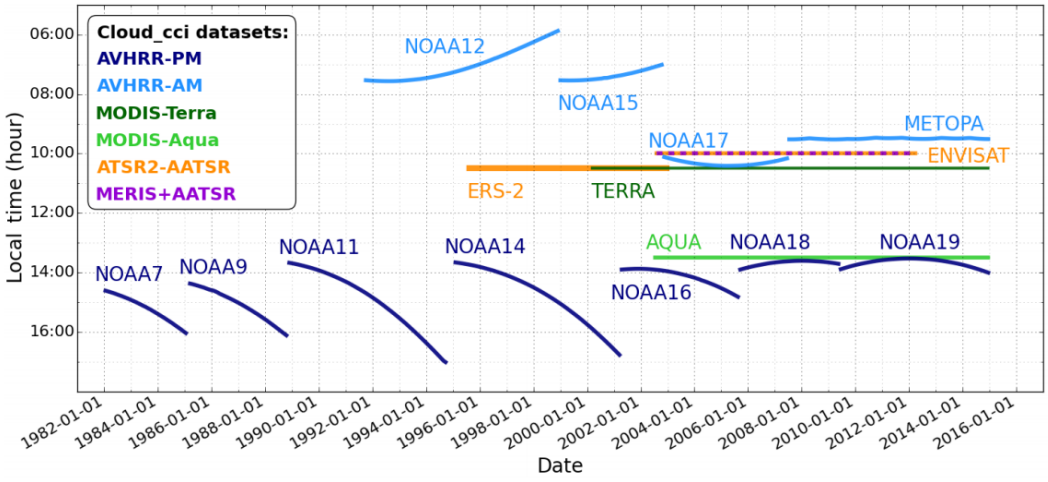

Fig. 1.3.: Time frames for the different satellite based instruments contributing to ESA's Cloud_CCI climate data record, from Stengel et al. (2017). The NOAA (AVHRR) morning and afternoon satellite measurements are also collected in the PATMOS-x dataset.

(GCOS), a project in the CCI framework exists, covering atmosphere, ocean and land. The climate data record of Cloud_CCI includes 30 years (see fig. 1.3) of cloud parameter retrievals, based on five different instruments mounted on several Earth observing satellite generations. The Pathfinder Atmospheres-Extended (PATMOS-x, Foster and Heidinger (2013)) is part of the climate data record of National Oceanic and Atmospheric Administration (NOAA) and is a collection of the Advanced Very High Resolution Radiometer (AVHRR) data sets concerning atmospheric parameters (clouds and aerosols) starting in 1978. Those climate data records are an important contribution to the understanding of the Earth's climate, while providing large amounts of data for instrument inter-comparison and evaluation exercises.

1.4 Thesis Outline

This thesis is dedicated towards the improvement of satellite remote sensing algorithms for cloud property retrievals with the O_2 A band method. This passive remote sensing technique in the near infrared spectrum has shown to be sensitive towards the assumed vertical profile of the cloud (Fischer and Grassl, 1991). Therefore, providing improved a priori knowledge of the retrieved atmospheric state can support the determination of cloud properties significantly and will reduce uncertainties. Moreover, previous work by Carbajal Henken et al. (2015) has shown that the cloud

top height retrieved in the near infrared spectrum carries some information about the vertical structure of clouds when compared to the cloud top height from infrared measurements, caused by differing penetrations depths into the cloud. The approach of this work will be based on two different principles. First, to improve cloud top height retrievals by simultaneously retrieving a parametrized cloud vertical profile by including additional spectral information into the known O_2 A band cloud top height retrieval, made possible by the increased number of spectral measurements by the Ocean and Land Colour Instrument (OLCI).
Second, development of a preprocessing algorithm to support the retrieval with a priori estimates about the profile of vertical extinction inside the cloud. Most of this work was done within the framework of the ESA Cloud_CCI project.

In Chapter 2 the used instruments for the studies are presented, together with the theoretical basis of radiative transport in the atmosphere. Also, the basics behind the retrieval algorithm and the radiative transfer simulations are introduced.

In Chapter 3 the sensitivities of OLCI are analyzed. Main emphasis is the sensitivity towards the vertical profile of the cloud and the amount of information that is obtainable through measurements in the oxygen absorption band A. This study is based solely on synthetic data from radiative transfer simulations.

In Chapter 4, the texture of clouds is studied regarding cloud classification purposes. Cloud are classified into well-known cloud types as well as into classes based on the vertical structure through a second order statistical analysis with the grey-level co-occurrence matrix and a random forest classification algorithm.

The performance of the advanced cloud property retrieval for OLCI as well as the established Freie Universität Berlin AATSR MERIS Clouds (FAME-C) algorithm are evaluated with the help of data products from active instruments in chapter 5.

Chapter 6 presents the comparison of a top of the atmosphere radiative flux retrieval by Christensen et al. (2016) against fluxes retrieved by NASA's CERES, for instantaneous retrievals as well as annual global means.

Finally a summary and brief outlook for further research activities is given in chapter 7.

2 Fundamentals

In this chapter the theoretical foundation of this thesis is presented. Each of the following sections is important for more than one chapter. Specialized information regarding a single part of this work will be introduced separately at the necessary time.

2.1 Satellite Remote Sensing

Since the dawn of meteorological satellites, starting in 1961 with the first Television and InfraRed Observation Satellite-1 (TIROS-1), the amount of Earth observing weather satellites and thus the variance of remote sensing instruments has greatly increased. Today, most national and international space agencies maintain various satellite systems orbiting Earth for weather and climate applications, monitoring land masses, ocean and atmosphere.
Earth observing satellites are usually categorized into two types based on their respective orbits. Polar-orbiting satellites are on a low Earth orbit, i.e. the altitude is below $1200km$. They circle the Earth from north to south and vice versa and achieve global coverage through Earth's rotation. Often, the orbit is chosen to be sun-synchronous, meaning the satellite crosses the equator when ascending (south to north) and descending (north to south) at the same local time.
The second type are geostationary satellites on a high Earth orbit at approximately $35.786km$, viewing the same region on the Earth at all times and providing important insights into dynamic processes.
In the following, the remote sensing instruments on weather satellites employed in this work are introduced. All of the utilized instruments are based on polar-orbiting satellites.

2.1.1 MODIS

One of the most known passive remote sensing instruments is the Moderate-Resolution Imaging Spectroradiometer (MODIS) onboard NASA's two earth-observing Satellites Aqua and Terra. NASA's Terra satellite was launched on December 18, 1999 and two and a half year later on May 4, 2002 Aqua followed. Both satellites are on a sun synchronous, near polar orbit at $705km$ height, from where MODIS with a $\pm 55°$ scanning pattern covers a swath of $2330km$. Terra has a descending orbit with equator crossing at 10:30 a.m. and Aqua an ascending orbit with a crossing time around 1:30 p.m. This leads to a global coverage in 1-2 days for each MODIS instrument. Both instruments are essentially identical, featuring 36 spectral bands ranging from $0.4 - 14.4\mu m$ with a spatial resolution of either $250m$, $500m$ or $1km$, depending on the spectral band. Based on the MODIS measurements NASA provides several official data products including Earth system variables for land, water, cryosphere and atmosphere in temporal resolution of instantaneous measurements as well as daily and monthly averages.
While the MODIS Terra instrument provides the science community with important climate measurements, the Aqua satellite is of special interest, because of its part in the afternoon train (A-Train). The A-Train is a constellation of, at this moment, six earth observing satellites (EOS) on the same orbital track. All satellites cover the same ground track within seconds to minutes of each other with different measurement principles, but overlap in the retrieved climate variables. Thus, allowing in depth studies of Earth's climate, synergy based products as well as validation studies and comparison of different retrieval techniques for various properties of the Earth system.

2.1.2 Cloud Profiling Radar

The Cloud profiling radar (CPR) on board the CloudSat satellite is one of the active remote sensing instruments in the A-Train. CloudSat was launched on 28th of April 2006 and joined the A-Train shortly after. The CPR was the first satellite-based millimeter radar ever. It operates at a frequency of $94 - GHz$ with a nadir viewing angle close to $0°$. With an integration time of 0.16sec the resolution is at $1.7km \times 1.4km$ (along- $\times$ across-track) with a vertical resolution of $240m$ and a minimum detectable signal of $-30dBZ$. The objective of the CloudSat mission is to further the understanding of clouds and precipitation in order to improve their representation in weather prediction and climate models (Stephens et al., 2002).

Special focus is hereby on the vertical distribution of clouds, which is still a source of uncertainty in those models.
The official CloudSat products are supported by MODIS and CALIOP measurements, which can be found in detail in the respective process description and interface control document (PDICD) of each data set at `http://www.cloudsat.cira.colostate.edu/data-products/`.

2.1.3 CALIOP

The Cloud-Aerosol Lidar and Infrared Pathfinder Satellite Observation (CALIPSO) was launched together with CloudSat in 2006 and trails it with a few seconds of delay in the A-Train. CALIPSO features a nadir viewing lidar measuring at $532nm$ and $1024nm$: the Cloud-Aerosol Lidar with Orthogonal Polarization (CALIOP). CALIOP has a footprint size of $333m \times 100m$ and a vertical resolution of $30m - 60m$. Similar to CloudSat, CALIPSO's advantage is to resolve the atmosphere vertically, whereby the mission is more oriented towards aerosol, clouds and their interaction. The LIDAR is more sensitive towards small optical depth, allowing the detection of aerosol clouds, which are optically thinner than water clouds. The sensitivity comes with the disadvantage of a saturated signal for higher optical depth which can be caused by optically thick clouds, leading to no information for parts of the vertical column.

2.1.4 AATSR

The Advanced Along-Track Scanning Radiometer (AATSR) on board of the Environmental Satellite (ENVISAT) was designed to establish continuity of the Along Track Scanning Radiometer (ATSR) 1 and 2 with measurements of the sea surface temperature during the day and night. ENVISAT was operational far beyond its nominal lifetime of 5 years, from 2002 until 2012. The secondary scientific objective was to perform land observations, giving estimates of the state of vegetation. Further, the thermal infrared channels at $10.85\mu m$ and $12\mu m$ as well as the visible channel at $665nm$ and the near infrared at $1.6\mu m$ are suited for the retrieval of cloud macro- and micro physical properties.
The instruments was designed to have two near simultaneous viewing directions through a conically scanning mirror, channeling radiation from the nadir and forward

viewing apertures into the radiometer. The multi-viewing instrument was a design choice, in order to remove atmospheric effects from the sea surface temperature measurements. At nadir, the spatial resolution was approximately $1km \times 1km$ and the total swath width was 512 pixels.

2.1.5 MERIS

The Medium Resolution Imaging Spectrometer (MERIS) was a so called "push-broom" radiometer on board of ENVISAT, measuring radiation in 15 spectral channels in the visible and near infrared spectrum. It consisted of 5 cameras, spanning a field of view of $68.5°$, which corresponds to a swath width of $1150km$. The full spatial resolution at nadir is dependant on the surface. For soundings over coastal zones and land surfaces at $300m$ resolution is achieved, while the reduced resolution of $1.2km$ (4x4 pixel binned) is generated continuously. Main objective for MERIS were ocean colour observations, retrieving information about organic and inorganic materials in the oceans. However, some spectral bands were chosen to be also viable for atmospheric and land observations. Utilizing MERIS channels 10 ($753.75nm$) and 11 ($760.625nm$) enables the retrieval of cloud top height and cloud optical depth by the O_2 A band method.

2.1.6 OLCI

The Ocean and Land Colour Instrument (OLCI) is a push-broom imaging spectrometer and the successor to MERIS. OLCI is flying on the European Space Agencie's (ESA) EOS Sentinel-3A since February 16, 2016 and was joined y Sentinel-3B with OLCI-B on the 6th of April 2018 in the same orbit for the time of the commissioning phase (around 4 month). The tandem configuration will enable calibration of the B-units based on the already aquired knowledge from Sentinel-3A. OLCI consists of 5 identical cameras spanning a field of view of $68.5°$, which is tilted by $12°$ westwards to reduce sun-glint over the ocean, leading to an effective swath of $1300km$. OLCI products are provided in a sub-satellite point spatial resolution of approximately $300m \times 300m$ (FR) for land and coastal regions. If no charted land is in $300km$ distance to the nominal swath, the products are provided in reduced resolution mode (RR) of approximately $1.2km \times 1.2km$. Each OLCI camera is equipped with an optical grating leading to 21 simultaneous spectral measurements in the visible and near-infrared. The spectral bands are programmable in flight. All operational

spectral band of OLCI-A are shown in table 2.1. While mainly designed as an ocean colour and land sensor OLCI's spectral bands allow remote sensing of Earths atmosphere. For clouds parameter retrievals, the channels 12-15, situated at and in the oxygen absorption band A (O_2 A band), can be used.

2.2 Radiative Transfer Equation

The retrieval of atmospheric variables through satellite remote sensing is complicated by signal contributions from differing sources, which are not easily separated. When studying clouds the measurement is always contaminated by radiation reflected at the surface, contributions from gaseous absorption and scattering in the atmosphere. The measurement can not be directly related to the sought atmospheric state, making a two-step approach necessary. Therefore, in a first step a suitable forward model is used to simulate possible measurements and in a next step an inversion technique is employed to find the best approximation of the real measurement from all the prepared simulations. The applied forward model can be a radiative transfer model, which is provided with all the necessary atmospheric parameters to simulate the measurement.
In Order to simulate the radiative transfer with a satisfactory accuracy several processes have to be considered. Incident light interacts with the particles in our atmosphere, which can change the light. Comparing the incident towards the altered light field can yield information about the kind of matter that took part in the interaction. This process of light travelling through the atmosphere is described by the radiative transfer equation (RTE). In this work, the presentation of the RTE is limited to the 1-dimensional plane parallel atmosphere, which discards any variation of the atmospheric state in the horizontal plane. Only vertical variations are of importance in this model, which is a good approximation in most cases since variations along the horizontal usually appear on a much larger scale than vertical variations. Therefore, highly horizontally variable cloud fields like cumulus clouds are not as well represented by the plane parallel assumption as others. Also, the plane parallel atmosphere has no earth curvature, which only holds if the angle of incoming radiation is far from $90°$ towards the zenith (Petty, 2006).
The plane parallel radiative transfer equation yields:

$$\mu \frac{\partial I(\mu, \phi)}{\partial \tau} = I(\mu, \phi) - J(\mu, \phi) \tag{2.1}$$

Band	λ centre [nm]	Width [nm]	Function
Oa1	400	15	Aerosol correction, improved water constituent retrieval
Oa2	412.5	10	Yellow substance and detrital pigments (turbidity)
Oa3	442.5	10	Chl absorption max., biogeochemistry, vegetation
Oa4	490	10	High Chl, other pigments
Oa5	510	10	Chl, sediment, turbidity, red tide
Oa6	560	10	Chlorophyll reference (Chl minimum)
Oa7	620	10	Sediment loading
Oa8	665	10	Chl, sediment, yellow substance/vegetation
Oa9	673.75	7.5	For improved fluorescence retrieval and to better account for smile together with the bands 665 and 680 nm
Oa10	681.25	7.5	Chl fluorescence peak, red edge
Oa11	708.75	10	Chl fluorescence baseline, red edge transition
Oa12	753.75	7.5	O2 absorption/clouds, vegetation
Oa13	761.25	2.5	O2 absorption band/aerosol corr.
Oa14	764.375	3.75	Atmospheric correction
Oa15	767.5	2.5	O2A used for cloud top pressure, fluorescence over land
Oa16	778.75	15	Atmos. corr./aerosol corr.
Oa17	865	20	Atmos. corr./aerosol corr., clouds, pixel co-registration
Oa18	885	10	Water vapour absorption reference band.
Oa19	900	10	Water vapour absorption/vegetation monitoring (max. reflectance)
Oa20	940	20	Water vapour absorption, atmos./aerosol corr.
Oa21	1020	40	Atmos./aerosol corr.

Tab. 2.1.: Operational spectral bands of Sentinel-3A OLCI. Taken from `https://sentinel.esa.int/web/sentinel/user-guides/sentinel-3-olci/overview/heritage/`.

with $I(\mu, \Phi)$ being the scalar intensity of the radiation, without polarization. $J(\mu, \Phi)$ is the source function for scattering and emission and μ is given by $cos(\theta)$, θ being the angle of incoming radiation. On the left side, the partial derivative of the intensity $I(\mu, \Phi)$ to the optical depth τ is formed. The optical depth, also called optical thickness, is given by:

$$\tau(z) = \int_z^\infty \beta_e(z')dz' \tag{2.2}$$

with β_e as the volume extinction coefficient, which is defined as the sum of absorption β_a and scattering β_s coefficients. The source function can be expressed as a part for emission and one for scattering and is given by:

$$J(\mu, \Phi) = (1-\omega)B(\lambda, T) + \frac{\omega}{4\pi}\int_0^{2\pi}\int_{-1}^{1} P(\mu, \phi; \mu'\phi')I(\mu'\phi')d\mu' d\phi'. \tag{2.3}$$

The single scattering albedo ω is given by the ratio of scattering- to extinction coefficient.

$$\omega = \frac{\beta_s}{\beta_e} = \frac{\beta_s}{\beta_s + \beta_a} \tag{2.4}$$

B is the temperature dependent emission of black body radiation given by the Planck law as:

$$B(\lambda, T)dAd\lambda = \frac{2\pi hc^2}{\lambda^5}\frac{1}{e^{(\frac{hc}{\lambda kT})} - 1}dAd\lambda \tag{2.5}$$

and $P(\mu, \phi; \mu'\phi')$ is the phase function, which describes the angular redistribution of light due to scattering. The phase function is normalized, meaning that in the case of purely elastic scattering all light will be scattered into some angular direction.

2.3 Mie-Theory and Cloud properties

Clouds consist of concentrated liquid or solid water in form of droplets or crystals, respectively. Light interaction with those particles can, for liquid cloud droplets, be described by the Mie theory for scattering and absorption of light with spherical particles. A full derivation of the Mie theory can be found in (Bohren and Nevitt, 1983). One, important result of the Mie theory is the phase matrix $P_{ij}(\theta)$ describing the wave scattering amplitudes as a function of the scattering angle θ between incident and scattered light. The phase matrix is reduced to the so called phase function, $P(\theta)$, when polarization is neglected. The form of $P(\theta)$ depends on the

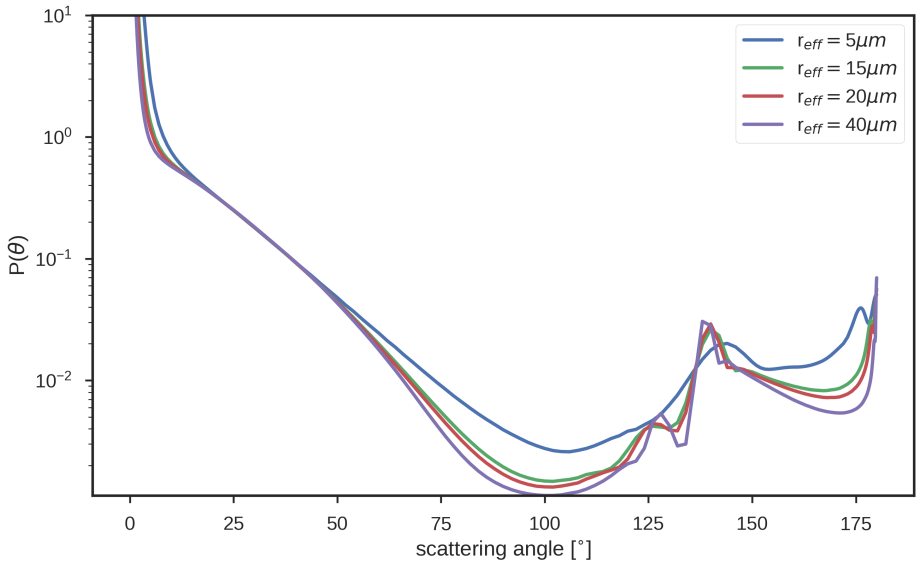

Fig. 2.1.: Scattering phase function for different size distributions for water clouds.

size of the scattering particle r and the wavelength λ of incident light, which is combined to the size parameter χ.

$$\chi \equiv \frac{2\pi r}{\lambda} \tag{2.6}$$

The radius of the hydrometeor is usually between $1\mu m - 50\mu m$ for liquid particles and $20\mu m - 2000\mu m$ for ice particles, whereby ice can occur in different shapes, where the Mie-theory is no longer valid. All clouds are made up by a mixture of different sized drops, described by the droplet size distribution $n(r)$, which integrated over all droplet radii gives the droplet number concentration N:

$$N = \int_0^\infty n(r)dr \tag{2.7}$$

The droplet number concentration is restricted by the number of cloud condensation nuclei (CCN) and the amount of available water vapour in the atmosphere. Aerosols function as condensation nuclei, and the size distribution is largely given by the amount and type of aerosols. If the amount of available water in the atmosphere is constant, a pristine atmosphere, has smaller number of nuclei and therefore the formed cloud droplets are larger. The higher the pollution of the atmosphere the smaller the resulting cloud droplets will be.

It is not feasible to treat a cloud analytically including each cloud droplet radius in the calculations, i.e. compute a phase function for each particle size and each wavelength of interest. However, it is common to describe a distribution by statistical parameters like mean, variance or the moments of the function. According to Hansen and Travis (1974) the particle size distribution can be described by an effective radius r_{eff} given by:

$$r_{eff} = \frac{\int_0^\infty r^3 n(r) dr}{\int_0^\infty r^2 n(r) dr}, \tag{2.8}$$

which is the ratio of the third moment to the second moment of the particle size distribution. Using the effective radius, the optical depth of a liquid cloud can be described by:

$$\tau \approx \frac{3LWP}{2\rho_l r_{eff}}. \tag{2.9}$$

Here, LWP is the so called liquid water path and is the special case of the cloud water path (CWP) for liquid phase clouds. The CWP measures the condensed water in the atmospheric column and is given by:

$$CWP = \int_{z_{base}}^{z_{top}} \rho_w(z) dz = \int_0^\infty \frac{4\pi}{3} n(r) \rho_l r^3 dr. \tag{2.10}$$

Here, $\rho_w(z)$ is the cloud water density or cloud water content and ρ_l is the density of water $\sim 1000 kg/m^3$. The optical depthτ of equation 2.9 can either be representative for the complete cloud or only for a part of it, depending on the integral limits in equation 2.10 and the related particle size distribution for the respective part of the cloud. This means every cloud can be divided into N adjacent cloud layers, not to be confused with multi-layer clouds, where the individual cloud layers are separated by cloud free atmosphere. Each of the N cloud layers has it's own particle size distribution and liquid water content and therefore a specific optical depth τ_i. The sum of all τ_i yields the total optical depth of the cloud:

$$\tau = \sum_i^N \tau_i. \tag{2.11}$$

That goes to show, that the optical properties of a cloud don't have to be uniform throughout the cloud's vertical extent and generally will vary strongly. In the following, this vertical profile of cloud optical depth will be referred to as the vertical extinction profile.

In figure 2.1 the phase function of liquid particles of different size distributions is presented. The droplet size distribution is given by a gamma-Hansen distribution (Hansen, 1971) and characterized by the effective radius r_eff. Water and ice clouds

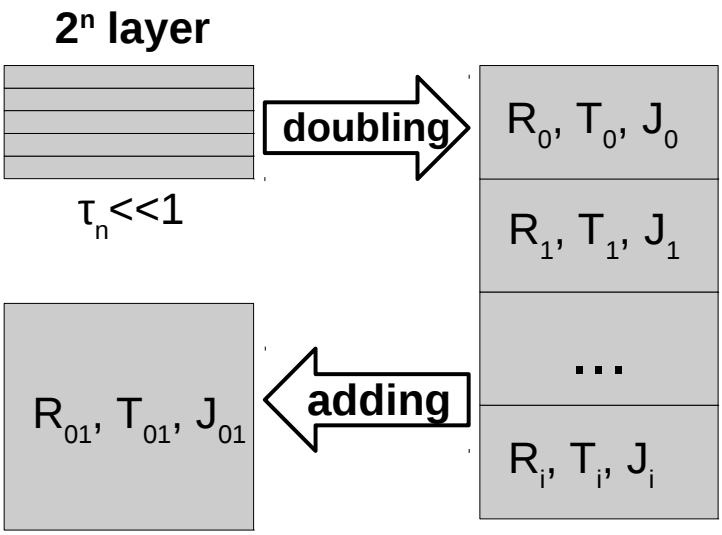

Fig. 2.2.: Schematic of adding and doubling in MOMO. Each original layer is divided in 2^n elementary layers, which are than added to retrieve R, T and J. By applying the adding method for each original layer the matrix operators for the complete atmosphere are retrieved.

(not shown here), exhibit a strong forward peak at $\theta \approx 0°$ and a smaller backward peak at $\theta \approx 180°$ in the phase function. Liquid particles also have the characteristic primary and secondary rainbows, visible at $137°$ and $130°$, respectively. Clouds are highly reflective in the visible spectrum making them appear white to the human eye. This is caused by the imaginary part of the refractive index for water in this spectral region being close to zero, i.e. most of the incident light is scattered and only a small portion will be absorbed, which is in terms of the single scattering albedo (see eq. 2.4) $\omega \approx 1$. In the near infrared spectrum $\omega < 1$, meaning the absorption of radiation from cloud particles can not to be neglected. For example at a wavelength of $\lambda = 1.7\mu m$ the single scattering albedo for liquid clouds is higher as for ice clouds leading to distinctive differences in the intensity of reflected radiation because of the higher absorption by ice clouds.

2.4 Radiative Transfer Model

All radiative transfer simulations used in this work were performed by the Martix operator model (Plass et al., 1973) (MOMO) by Fell and Fischer (2001). MOMO is a monochromatic radiative transfer model assuming a 1-D plane parallel atmosphere developed and constantly improved by the Institute for Space Sciences of the Freie Universität Berlin. The radiative transfer calculations are vertically and angularly resolved. MOMO is able to numerically solve the radiative transfer equation for wavelength between $0.2nm - 100\mu m$ (Doppler et al., 2014a) and is able to account for processes like Raman-scattering (Von Bismarck, 2016), polarization (Hollstein, 2013) and fluorescence. The method is based on the interaction principle stating, that the outgoing light field at the boundary layer of a scattering, absorbing and emitting medium is linearly related to the incident light and the radiation generated inside the medium. For upward (-) and downward (+) facing radiation the interaction principle gives:

$$L_0^- = R_{01}L_0'^+ + T_{10}L_1'^- + J_{10}^- \tag{2.12}$$

$$L_0^+ = R_{10}L_1'^- + T_{01}L_0'^+ + J_{01}^+, \tag{2.13}$$

where R, T and J are the reflection, transmission and source operators for the medium with boundary optical depth τ_0 and τ_1. Incident radiation is denoted by a prime. Each operator is given by a $k \times k$ Matrix, where k is given by the angular resolution chosen for the simulations. Also, derived from the interaction principle is the doubling and adding method. The doubling algorithm dictates how the reflection, transmission and source operators are combined for two identical homogeneous vertical layers. For MOMO an arbitrary number of vertical layer is defined for which the radiative transfer is calculated. Every vertical layer can differ from its neighbours but is in itself assumed to be homogeneous, i.e. the optical properties are constant within each layer. Each individual layer is divided into 2^n elementary layers, with τ being small enough that multiple scattering can be neglected (see also figure 2.2). Through the doubling algorithm the matrix operators for two adjacent elementary layers is derived from the single layers properties. This step is repeated n-times, resulting in R_n, T_n and J_n of the original layer. Afterwards the adding method is applied to retrieve the combined matrix operators from two layers with arbitrary optical properties. In the end the radiation field at each layer interface can be computed. The matrix operator model has to treat the radiative transfer from the bottom of the atmosphere, since for the radiation field at the boundary between two

layers the up-welling radiance from the lower layer has to be known.
To simulate the radiation field several input parameters are necessary:

- The vertical profile of the atmosphere has to be known. This includes temperature and pressure profile as well as gas and particle concentrations. The vertical profiles can either be user defined or taken from the well-known standard atmospheres by McClatchey et al. (1972). In a pre-processing step, the standard atmospheres are interpolated on the desired vertical resolution.

- The gaseous absorption in the atmosphere is provided by the Coefficient of Gas Absorption (CGASA, Doppler et al. (2014a)) algorithm. CGASA uses the defined vertical profile of the atmosphere and calculates the transmission spectra in the desired wavelength regime. The basis is formed by the High-Resolution Transmission molecular absorption database (HITRAN, Rothman et al. (2013)), providing position of molecular absorption lines as well as the full-width at half maximum and the amplitude. The transmission for each atmospheric level is then calculated by fitting a Voigt line to each absorption line of HITRAN. The water vapour continuum absorption is handled by the Mlawer, Tobin-Clough, Keizys-Davies (MT-CKD, Mlawer et al. (2012)) coefficients. In order to speed up the runtime of MOMO line-by-line simulations are avoided. The k-distribution of the Institute for Space Sciences (KISS) (Bennartz and Fischer (2000), Doppler et al. (2014b)) is used to perform radiative transfer simulations for larger spectral intervals. In the case of line-by-line calculations each spectral subinterval (of reasonable width, no change in optical properties in the subinterval) has to be simulated individually. When using the uncorrelated k-distribution through KISS the spectral dependent transmission coefficients are sorted by the absorption strength and divided into the so called k-bins. The absorption inside each k-bin are assumed to be the same and the number of k-bins for the spectral interval depends on the targeted accuracy. The spectral interval of the radiative transfer simulations can not be too large, since the uncorrelated k-distribution assumes no interaction between the gases and optically relevant and spectral dependent parameters. Therefore, the spectral interval has to be chosen in a way that the solar irradiation and the surface albedo can be assumed as constant.

- The phase function, single scattering albedo and normalized extinction coefficient of all scattering particles in the atmosphere has to be known. This can be done using a Mie algorithm for spherical particles, resulting in the Rayleigh

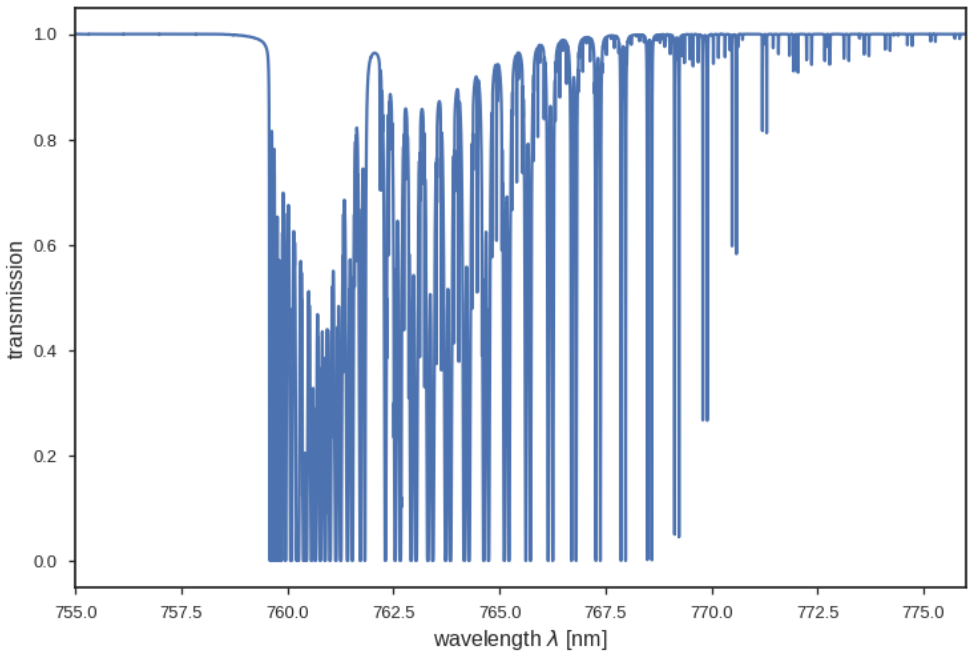

Fig. 2.3.: CGASA transmission calculations of the oxygen absorption band A.

scattering properties of the atmosphere as well as the optical characteristics of water clouds.

The output of a MOMO simulation are the up- and downwelling radiances at each layer boundary as well as at the top and bottom of the atmosphere. The output is in terms of radiances for each calculated k-bin and a mapping function, which is given by KISS, can be used to convert back into the wavelength representation. MOMO can be used including the solar irradiance or not, leading to true radiances or normalized radiances as a result. In this work, only normalized top of atmosphere radiances are used.

2.5 O_2 A Band retrieval

The application of remote sensing for the retrieval of the cloud top pressure was already proposed by Hanel (1961) after the TIROS campaign sparked the interest of scientists for satellite remote sensing. Hanel suggested to make use of a CO_2 band at $2\mu m$. In a response Yamamoto and Wark (1961) suggested the use of the O_2 A band.

As mentioned before, radiation interacts with the particles in different ways leading to light containing the information about the atmospheric state. The O_2 absorption band A (see. figure 2.3) starting at $\lambda \approx 760nm$ and going to $\lambda \approx 775nm$ is a spectral region where, due to interaction with oxygen, the remote sensing of cloud properties is possible.
Oxygen, in molecular form, is a well mixed gas in the atmosphere, i.e. there are almost no variations, vertically as well as horizontally, in the proportion of oxygen in the air (20.9%). No other gases absorb in this spectral region, thus the radiance measurements in the O_2 A band are governed by the surface albedo and the total airmass along the path sun-target-satellite. The amount of absorption by oxygen is a good measure for the mean photon path length l and is therefore directly related to the mean position in the atmosphere, where most of the radiation is reflected in the direction of the measuring instrument. The retrieval principle for cloud top pressure is a differential absorption technique, which makes use of the ratio between at least one measurement inside the absorption band and one at a close wavelength, without considerable atmospheric absorption. The absorbed radiance is reduced as a function of the traversed air mass, given by the sun and viewing zenith angle (sza/vza), while the window channel shows no dimming beyond scattering effects. When the surface albedo is well-known or the cloud optical depth is high enough to suppress surface influences the ratio between window and absorbing measurement

$$r = \frac{L_a}{L_w}, \tag{2.14}$$

can be indirectly related to a cloud top pressure. The ratio r is always $r < 1$ and is a function of the viewing geometry, surface albedo and cloud properties. For a non-reflective surface, r is smaller the lower the cloud is in the atmosphere, but cloud properties create ambiguities in the retrieval. Cloud optical depth τ controls the mixing between signal associated with the surface and cloud, while cloud vertical extinction profile, consisting of cloud geometrical thickness and vertically resolved cloud extinction, determines the penetration depth of radiation inside the cloud. While the cloud optical depth can be retrieved with a good accuracy from the intensity of the window channel alone, the retrieval of the vertical profile is problematic for passive imagers, which as a result leads to larger uncertainties and errors in the retrieved cloud top height. The O_2 A band method was shown to be effective, when retrieving low and optically thick clouds, where the variations on the vertical extinction profile are potentially on a smaller scale as for high clouds. Sensitivity studies of the MERIS cloud top pressure retrieval by Preusker and Lindstrot (2009) showed, that the geometrical extent is the most important cloud property besides

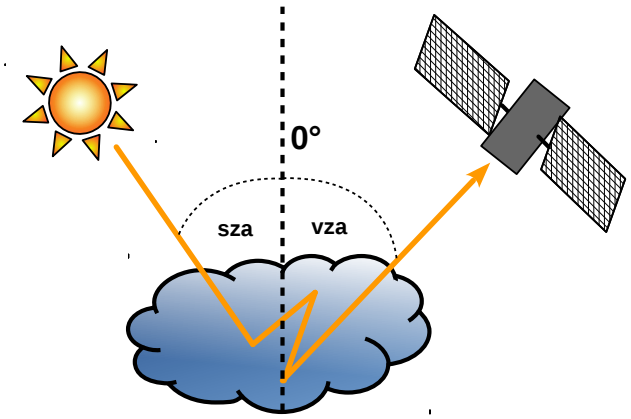

Fig. 2.4.: Schematic of photon path length extension due to in cloud multiple scattering. The penetration depth determines the probability of multiple scattering taking place

the cloud top pressure and the cloud optical depth for the top of atmosphere signal. Further, the problematic case of multi-layer clouds was studied, yielding that this method fails when more than one cloud layer is apparent. Only in cases where one of the two cloud layers was optically very thin a satisfactory CTP was retrieved. Airplane measurements by Lindstrot et al. (2006) using a LIDAR revealed that the cloud top pressure of low level single-layer clouds over Germany could be retrieved with MERIS O_2 A band channels, with an accuracy of $24hPa$ and a systematic bias of $-22hPa$. However, for optically thinner and geometrically thicker clouds the retrieval tend to yield cloud top pressure inside the actual cloud. The cause was found by Saiedy et al. (1967) to be multiple scattering inside the clouds. In figure 2.4 the process is shown schematically. The cloud vertical extinction profile determines the mean penetration depth of photons into the cloud. With deeper penetration depths, the probability of multiple scattering rises and the photon path length becomes larger than in the assumed single scattering event. In most retrievals the cloud is either assumed to be vertically homogeneous or multiple scattering inside the cloud is neglected. Theoretical studies have shown that the impact of the cloud vertical profile is important when retrieving the CTP with the oxygen A band method(Fischer and Grassl (1991), Rozanov and Kokhanovsky (2004)). Other retrieval methods for the cloud top pressure exhibit different sensitivities. Cloud radar and lidar are active instruments, which are employed for cloud property retrievals. Those kind of instruments show a higher sensitivity to hydrometeors than

passive remote sensing instruments. Therefore, already optically very thin parts of clouds can be detected, leading to a retrieved cloud top height which is generally higher than the retrieved by passive imagers. In addition, the signal from active sensors contains more information enabling a direct derivation of the vertical profile of clouds. Other common methods for the determination of cloud top height are based on measurements in the spectral region of the thermal infrared, where the penetration depth of radiation into the cloud is smaller than in the visible/near-infrared spectrum. Thus, the sensitivity towards the vertical extinction profile of those methods is smaller than the O_2 A band methods sensitivity. On one hand this reduces the information about the vertical structure contained in the signal, but on the other hand knowledge about this vertical structure is not as necessary for an accurate retrieval of the cloud top height. One drawback of those techniques are their sensitivity towards the assumed vertical profile of atmospheric temperature, from which the O_2 method does not suffer. Those differences in the retrieval techniques leads also to different understandings in the cloud top height. While for active sensor the cloud top will be found at very small optical depths, thermal infrared based techniques will place the top of the cloud generally lower, which is even more true for the O_2 A band method when the penetration depth is not taken into account. The measured cloud top pressure is therefore an instrument specific CTP, where the radiation has penetrated an optical depth τ inside the cloud, where τ depends on the sensitivity of the instrument and the spectral region.

2.6 Inverse Problem

This section is based on description of inverse theory by Rodgers (2000) and for a complete review of inverse problems in atmospheric soundings the source material should be considered.
Scientific observations are an inverse problem, which describes the derivation of a state $\vec{x}$ from a measurement $\vec{y}$. In the terms of atmospheric remote sensing, one or multiple atmospheric parameters are retrieved by measuring the electromagnetic radiation. The function relating the state of the atmosphere towards the measurement is called the forward model $F(x)$:

$$\vec{y} = F(\vec{x}) + \epsilon. \tag{2.15}$$

ϵ denotes the measurement error, combining errors from the forward model, due to approximations, systematic errors and random errors (signal noise). The forward

model describes the process of the state leading to the measurement and in this case it is given by the radiative transfer model and the measurement vector consists of the combination of measured radiances and auxiliary data like viewing geometry, surface albedo, surface pressure and others. The sensitivity of the measured signal towards the state vector is given by the Jacobian also known as weighting function matrix K.

$$K = \frac{\partial F(\vec{x})}{\partial \vec{x}} \tag{2.16}$$

K maps the state $\vec{x}$ onto the measurement $\vec{y}$

$$\vec{y} = K\vec{x} + \epsilon \tag{2.17}$$

and has the form $m \times n$. When $m < n$ the problem is under determined since there are fewer measurements than unknown states. Problems with $m > n$ are over determined, having more measurements than unknowns. The aim is to find the inverse mapping function, which relates the measurement to the state. Therefore, the measurement is described by its probability density function (pdf) $P(y)$, of Gaussian form with mean $\bar{y}$ and variance σ_y^2, which is mapped by the inversion onto the state space. Similarly, the state is defined by $P(x)$ and the forward model maps the state pdf into the measurement space. The error covariance matrix S_ϵ can be defined with the components:

$$S_{ij} = \varepsilon[(y_i - \bar{y_i})(y_j - \bar{y_j})] \tag{2.18}$$

with ε being the expected value operator. The diagonal elements of S_y contains the variances of each measurement, while the off diagonal elements describe the correlation between errors. The mapping in both direction between measurement space and state space is ambiguous, i.e. a point in the measurement space can originate from an entire area in the state space due to the measurement error. Also, two different points in the state space can map to the same measurement by under-determination of the problem. Since we made the change to a probability density function we can apply Bayes' theorem to derive the most likely $\vec{x}$ for the given $\vec{y}$. The sought quantity is the probability of x given y $P(x|y)$. From the forward model we know the pdf $P(y|x)$ of $\vec{y}$ given an $\vec{x}$ and can make an estimate of the state before the measurement is done, the so called prior state $P(x)$. Bayes' theorem gives us:

$$P(x|y) = \frac{P(y|x)P(x)}{P(y)}, \tag{2.19}$$

with $P(y)$ being the prior knowledge of the measurement, which is in most cases only necessary for normalization. Applying Bayes' theorem for Gaussian pdfs yields the cost function χ^2:

$$\chi^2 = [\vec{y} - K\vec{x}]^T S_\epsilon^- 1[\vec{y} - K\vec{x}] + [\vec{x} - \vec{x}_a]^T S_a^- 1[\vec{x} - \vec{x}_a], \tag{2.20}$$

with index S_ϵ denotes the measurement covariance matrix and x_a and S_a are the a priori state and its error covariance matrix respectively. This relation only holds, if the environment of the state is linear. The aim is to minimize χ^2,which in turn maximizes $P(x|y)$ and yields the state $\vec{x}$, which most-likely belongs to the measurement $\vec{y}$.
There are several ways to iterate through the states to reduce the cost function. In this work the Gauss-Newton method is used.

$$x_{i+1} = x_i + (S_a^{-1} K_i^T S_\epsilon^{-1} K_i)^{-1} [K_i^T S_\epsilon^{-1} (y - F(x_i)) - S_a^{-1}(x_i - x_a)] \tag{2.21}$$

Here, the iteration starts at point x_i and is corrected by the second term in each step. The iteration runs for a predefined number of steps or until a convergence criterium is fulfilled. The method using the inverse theory to find the best state to a respective measurement assisted by a priori knowledge is called optimal estimation.
The application of the forward, model for remote sensing, at each iteration step in order to find the state corresponding to the measurement can be computationally expensive depending on the employed radiative transfer model. Hence, the look up table (LUT) approach is often applied. Here, a limited amount of simulations is performed and all the results are saved in a multidimensional table. The radiative transfer model is then replaced as forward model by an multidimensional interpolation in the look up table.

3 A Sensitivity Study Regarding Remote Sensing of Cloud Properties using the Oxygen A Band

The vertical structure of clouds can impact the retrieval of cloud top height and cloud optical depth. Therefore, the impact of small changes in cloud parameters towards the measured top of atmosphere signal (TOA) has to be considered. This quantity is known as the sensitivity of the signal towards an input parameter. The interaction of those cloud properties regarding the top of atmosphere signal can be quite complex, but can be studied through radiative transfer simulations. In the following study, OLCI's sensitivities to changes in cloud properties are examined.

3.1 Parametrization of Vertical Extinction Profile

The retrieval in the O_2 A band is based on the relation of mean photon path length towards the cloud top pressure. However, the cloud top pressure is not the only property influencing the path length. The amount of in-cloud scattering depends on the vertical extinction profile, which can lead to a significant increase of mean photon path length and therefore has to be considered in the framework of a cloud top pressure retrieval.
A cloud property retrieval including an extinction profile with CloudSat like vertical resolution is beyond the capabilities of the O_2 A band. Therefore, a suitable simplification of the vertical profile has to be found, which is a satisfactory reflection of reality while describing the variations with few free variables. The conceived parametrization in this work is given by two variables representing the geometrical extent and the distribution of the cloud vertical extinction profile, which will be called extent and mode/mode of optical depth. In figure 3.1 both parameters are visualized. In this representation the extent is given by a real number $ext = (0, 1]$

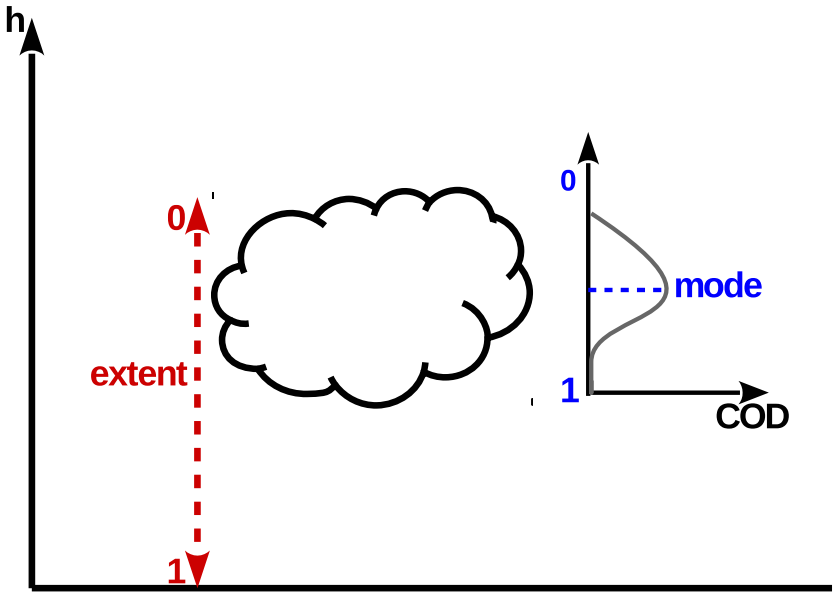

Fig. 3.1.: Visualization of cloud extent and cloud mode. The extent (red) is the relative part of the atmosphere ranging from cloud top to surface covered by the cloud. The mode (blue) is the relative coordinate of the maximal optical depth inside the cloud, h denotes the height.

and characterizes the relative part between cloud top and surface occupied by the cloud, i.e. $ext \approx 0$ denotes an infinitely narrow cloud, while $ext = 1$ represents a cloud ranging from the respective cloud top to the Earth's surface. Similarly, the mode represents the vertical position of maximal optical depth inside the cloud. It is given by the relative position between cloud top and bottom ($mode = [0, 1]$) and defines the applied beta probability distribution function for the distribution(β_{pdf}):

$$\beta_{pdf} = \frac{x^{a-1}(1-x)^{b-1}}{B(a,b)} \tag{3.1}$$

$$mode = \frac{a-1}{a+b-2} \tag{3.2}$$

with B being the beta function depending on the relative position x inside the cloud and a and b as the two shape parameters. For the applied distribution $b = 3$ and a is given through the chosen mode according to eq. 3.2. For extent and mode the abbreviations *ext* and *moi* (mode index) will also be used.

3.2 Jacobian and Sensitivity

Quantification of the sensitivity of the top of atmosphere radiance in the O_2 A band to changes in cloud parameters is based on radiative transfer simulations, performed with MOMO. The produced LUTs are also the basis to the cloud parameter retrieval, which is applied in the following chapters. As already mentioned in section 2.6, the Jacobian introduced in equation 2.16 gives the sensitivity of the signal towards the state and can be retrieved directly from the LUT by the partial derivative of the signal towards each forward model parameter. The produced look up table has nine dimension containing the viewing geometry (sun zenith angle, viewing zenith angle and relative azimuth angle), the central wavelength of the instrument channel, the surface albedo and surface pressure, and the cloud properties (cloud top pressure, cloud optical depth, cloud vertical extent and mode of cloud optical depth).
The sensitivities from the Jacobian depend on the absolute scale of each parameter, complicating the direct quantitative comparison. For this reason, the sensitivity in this study is defined similar to Preusker and Lindstrot (2009), as the partial derivative of the natural logarithmic of signal to the natural log of the parameter value times the change of the examined parameter in relative magnitude,

$$\xi_P = \frac{\partial\, ln(r)}{\partial\, ln(P)} \delta P. \tag{3.3}$$

and for absolute changes of the parameters

$$\xi_P = \frac{\partial\, ln(r)}{\partial\, P} \Delta P \tag{3.4}$$

Here, the studied signal is given by the ratio r of window and absorbing channel, P denotes the examined parameter and δP and ΔP are the relative and absolute change of the parameter, respectively. The studied parameters are the cloud top height, cloud vertical extent, optical depth and mode of optical depth as wells as surface albedo. Further, to increase comparability all sensitivities towards properties, that can be expressed in pressure units, are based on a change of $+10hPa$. The sensitivity toward changes of cloud optical depth and the surface albedo are based on an increase by 10%. Therefore, the sensitivity of both is subject to the respective absolute value. This work will mainly focus on the sensitivity towards the vertical profile of the cloud, i.e. the sensitivity towards cloud vertical extent and mode of optical depth will be compared to ξ_{ctp}. All variations underlying the calculated sensitivities are summarized in table 3.1.

parameter	$\delta P/\Delta P$
cloud top pressure	10hPa
cloud optical depth	10%
mode	10hPa (absolute position)
extent	10hPa (absolute extent)
suface albedo	10%

Tab. 3.1.: Summary of the changes in each parameter underlying the calculated sensitivities.

Slight misalignments as well as imperfections of the optical parts of an instrument can lead to displacements of the beam path, which subsequently can affect the bandwidth and centre wavelength of a channel. A change of the centre wavelength of a channel over the detector array (spatial pixel) is often referred to as "smile effect", which also affects OLCI as can be seen in figure 3.2. Since the variation of the bandwidth along the across-track directions for the O_2 A band channels is rather small this particular sensitivity was not examined here. However, the variations in centre wavelength are around $1nm$ and has to be considered, when studying all other sensitivities.

3.3 Radiative Transfer Simulation

Basis for the sensitivity study are the radiative transfer simulations with MOMO. The vertical resolution of the atmosphere was set to 50 levels between the surface and $65km$ or in pressure units from $1013hPa$ to $0.1hPa$, whereby the tropospheric levels are evenly spaced in the pressure space with $\Delta p = 20hPa$. Pressure and temperature gradient as well as gas concentrations are according to the US-Standard Atmosphere (McClatchey et al., 1972). The Rayleigh optical depth of the atmosphere is at $\tau_r = 0.026$. Only water clouds were simulated with an effective radius of cloud droplets at $r_{eff} = 10\mu m$ emerging from a modified Gamma Hansen distribution for the cloud droplet size with $r \in [0.12\mu m, 80\mu m]$. The surface was assumed to be a Lambertian reflector with varying albedo. The simulations were split into two spectral intervals, one for the window channel ranging from $745nm$ to $760nm$ and a second part from $753nm$ to $773nm$ for the absorption band channels. The gas absorption coefficient by CGASA were distributed into 6 and 70 k-bins for window and absorption channels, respectively. The simulations were performed without the solar constant, resulting in normalized TOA radiances for the 19 azimuth as wells as 35 solar- and viewing zenith angles. The mapping of the k-bins onto the wavelength

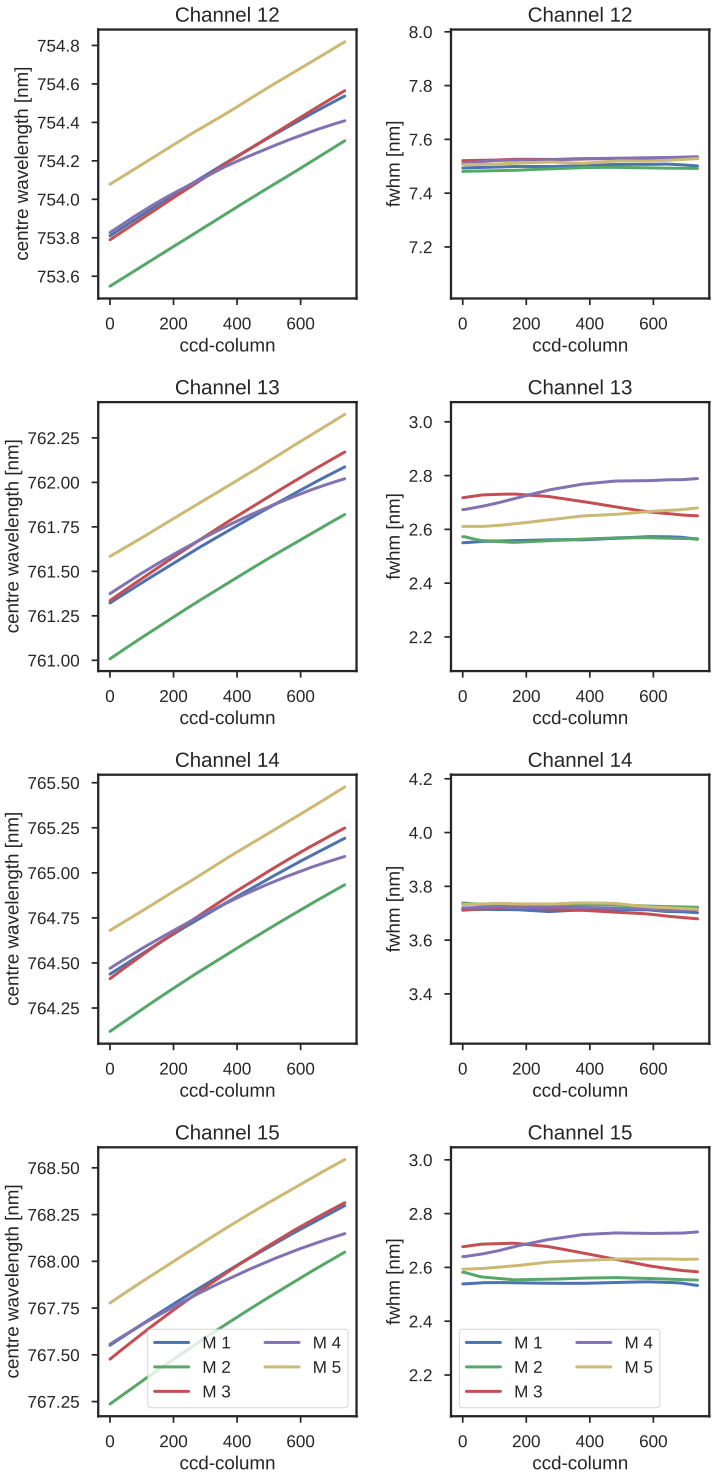

Fig. 3.2.: Left: OLCI central wavelength of instrument response function for channels 12 to 15 (top to bottom) as a function of the spatial ccd column for all 5 camera modules (M1-M5). Right: full width at half maximum for the same channels.

parameter	unit	simulation points
cloud top pressure	hPa	975, 900, 750, 500, 350, 100
cloud optical depth	-	1, 10, 50, 100, 150
mode of optical depth	-	0.1, 0.3, 0.5, 0.7, 0.9
vertical extent	-	0.1, 0.3, 0.5, 0.7, 0.8
surface albedo	-	0.02, 0.1, 0.6, 0.7
surface pressure	hPa	850, 950, 1013, 1050

Tab. 3.2.: Simulation points for MOMO as basis for the OLCI cloud parameter retrieval. Every permutation of the shown grid points was used for a simulation.

are done in a post processing step, where also the convolution with the instrument response functions is performed.
The aforementioned smile effect is considered during the convolution of the simulations and the instrument's spectral response by shifting the central wavelength of each OLCI channel. A consolation of the smile effect as exhibited by OLCI is the nearly constant behaviour for all camera modules, i.e. the same spatial pixel demonstrates a nearly identical spectral shift for all cameras and all channels. Therefore, all bands can be convoluted with the same spectral shift, reducing the number of dimensions in the LUT greatly. The full list of simulated scenarios can be found in table 3.2.

3.4 Central Wavelength of the Instrumental Channels

The central wavelength of the respective OLCI channels can have a large impact on the signal, since the amount of absorbed radiation by oxygen can vary strongly over a small spectral interval. For OLCI, four of the five modules exhibit a nearly constant displacement of the channel position with spatial pixel number, except for module 4, where the strength of the smile is reduced for pixel number > 350 (see fig. 3.2), which was neglected in the underlying simulations. The smile effect causes a shift in central wavelength of up to $1.0nm$ for the O_2 A band channels. Therefore, the central wavelength has to be considered when studying the sensitivities of the signal towards the atmospheric state. To gain a qualitative understanding of the impact of central wavelength towards the measurement sensitivities several cases close to the LUT's edges are studied. A variation of the central wavelength ranging between $-1nm$ and $+2.4nm$, towards the nominal wavelength of each channel, was

assumed. The interval of possible wavelength shifts was prepared larger than strictly necessary, since early calibration results of OLCI-A showed ongoing changes in the spectral response during commissioning phase.
In figure 3.3, the sensitivity depending on the central wavelength, for a low cloud at $ctp = 700hPa$, with an optical depth of $\tau = 10$, a vertical extent $ext = 100hPa$ and a mode of $moi = 0.1$ over dark ocean surface with $\alpha = 0.02$ is depicted, which are typical values for prevalent low-level water clouds like stratocumulus. For such a cloud, the top of atmosphere signal is most sensitive towards the cloud top pressure, with a change of up to -1.2% in the measured 13/12 channel ratio caused by a change of $+10hPa$ in cloud top. Followed by the mode of optical depth with $\xi_{moi}(\lambda) \geq -0.95\%$ and the cloud vertical extent with a sensitivity of up to $\xi_{ext}(\lambda) \geq -0.5\%$. There is only small sensitivity towards the albedo and the cloud optical depth. However, these low sensitivities are partly caused by the fact, that albedo and *cod* are varied by a relative amount and have low values to begin with. As expected, all sensitivities are reduced with increasing wavelength due to decreasing absorption by oxygen. For channel 15, the sensitivity to each property is very small and with a shift of the central wavelength by $+1nm$ nearly at zero. The cause is the channel's position close to the end of the O_2 A band, where the absorption of oxygen is greatly diminished. The cloud top pressure, extent and mode all cause a decrease in TOA signal with increasing values, since the pressure is inverse proportional towards the height and a change by $+10hPa$ corresponds to a lowering of the cloud. The negative sensitivity of the signal towards the surface albedo can be explained by the enhancement of the mean photon path length in the presence of a thin cloud. A brighter surface reflects more sunlight in the window and absorption channel, leading to the TOA signal having a larger contribution from the surface, which leads to an increase in the mean photon path length. Simplified, the total mean photon path length l_{tot} can be expressed as a mixture of surface and cloud contribution. When l_s is the mean photon path length for light reflected at the surface and l_c reflected at the cloud:

$$l_{tot} = w_c * l_c + w_s * l_s \tag{3.5}$$

where w_c and w_s are the proportions of the measured signal originating from the cloud and surface respectively and are mostly determined by the optical depth of the cloud and the surface albedo. Hence, an increase in cloud optical depth acts as a counterpart to the variations in surface albedo, by increasing the cloud's contribution to the signal. This effect more pronounced in the comparison of the same cloud above dark surface and bright surface with an albedo of $\alpha = 0.6$ as presented in figure 3.4.

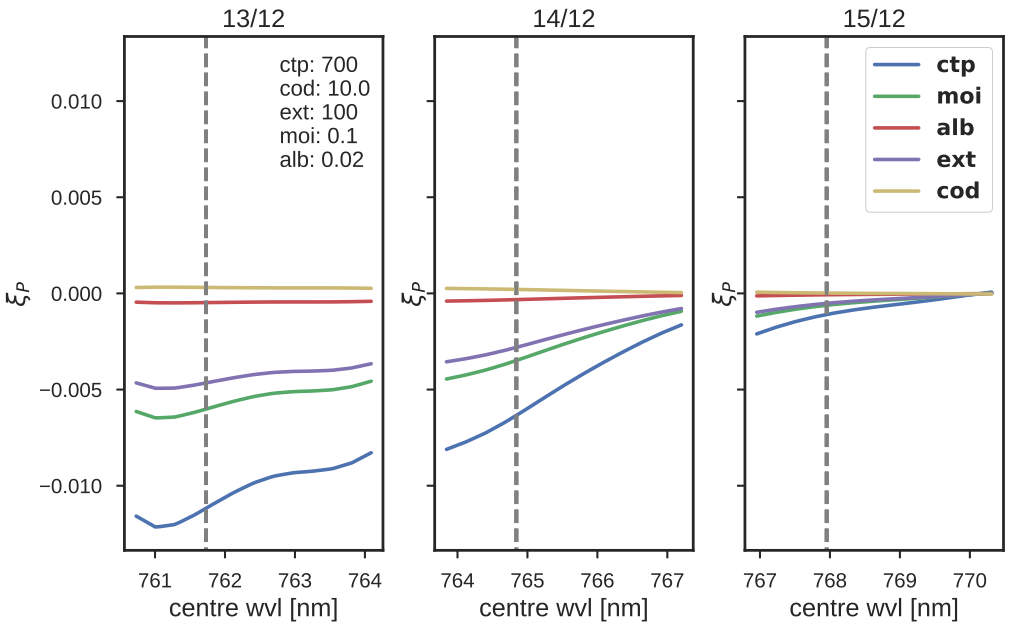

Fig. 3.3.: Sensitivity of the channel ratios (13/12; 14/12; 15/12, from left to right) towards changes in the atmospheric state, dependent on the central wavelength of the absorbing channels. The grey dashed line represents the nominal centre wavelength.

Here, a change in the surface albedo by 10% leads to a signal change of up to -2.5%. The increase of magnitude of the sensitivity is mainly caused by the underlying change in albedo being 30 times larger than in figure 3.3. The effect of changes in the cloud optical depth is also increased by the higher surface albedo, because now the optical depth also affects the proportion of the upwelling signal from the surface. The sensitivity towards changes of the cloud top and vertical profile is decreased slightly, due to a larger portion of the signal not originating from the cloud itself. Channel 15 is not responding at all to changes in *ctp*, *ext* and *moi*. If the same cloud is now lifted to a top pressure of $200hPa$, the sensitivity for the surface albedo and *cod* increases further, due to a larger part of the atmosphere being below the cloud, as shown in figure 3.5. The sensitivity of the signal towards changes in the albedo is quite significant with -4% for channel 13 and decreases to -1% for the nominal wavelength of channel 15.

However, for an optically thicker cloud of $\tau = 100$, shown in figure 3.6, the sensitivity towards surface albedo is reduced, since a large part of the light is reflected in the upper cloud layers and never reaches the surface. This is true for the low (fig. 3.6, top) as well as the high cloud (3.6, bottom), but with weaker O_2

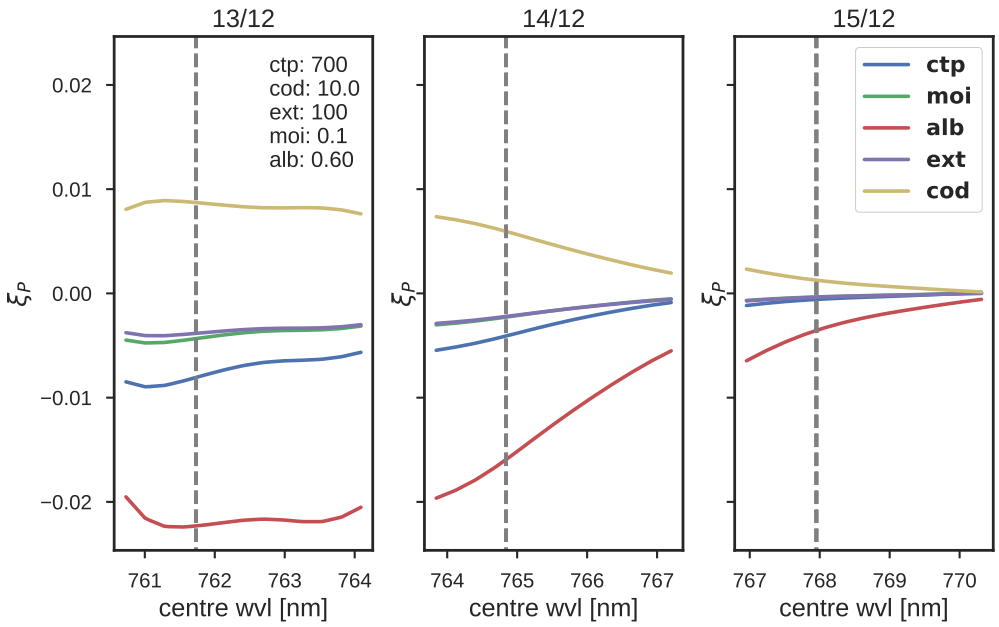

Fig. 3.4.: Similar to figure 3.3, but with an surface albedo $\alpha = 0.6$.

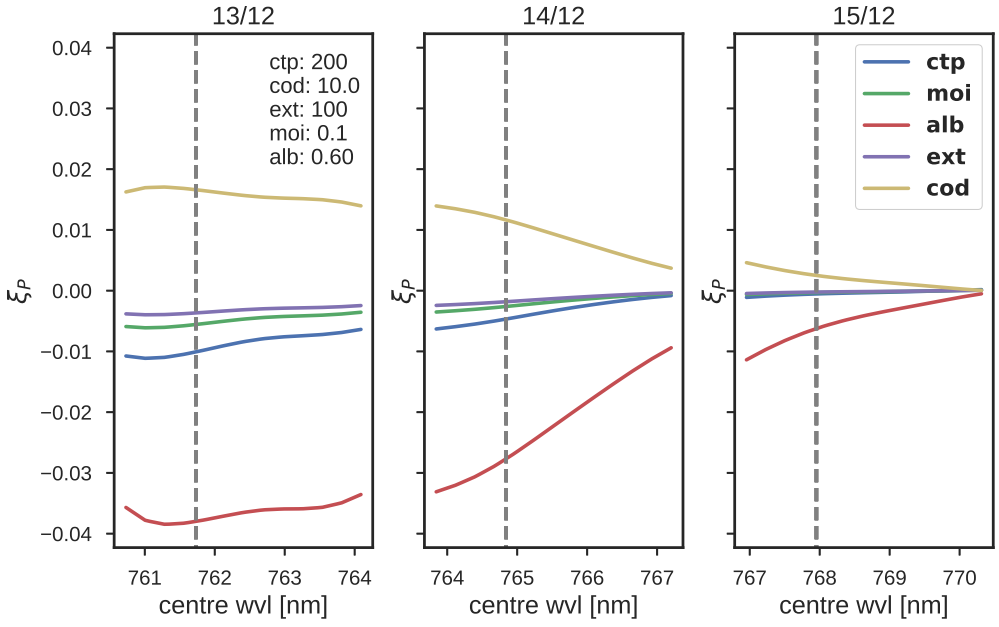

Fig. 3.5.: Similar to figure 3.4, but with an cloud top pressure of $ctp = 200hPa$.

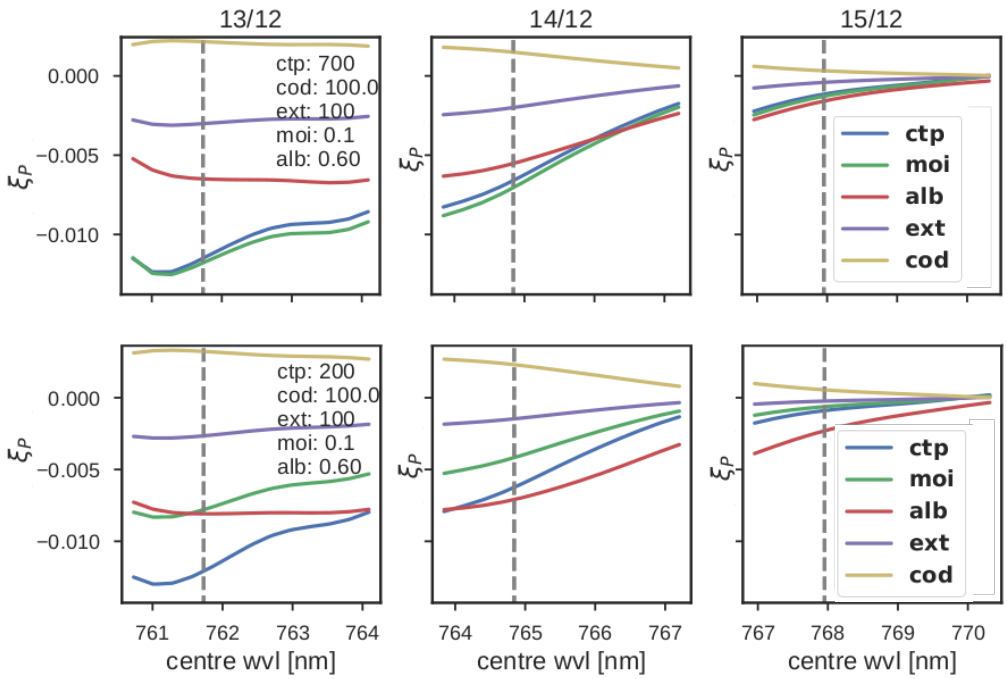

Fig. 3.6.: Sensitivities for low (700hPA, top) and high (200hPa, bottom) cloud with surface albedo $\alpha = 0.6$ and cloud optical depth of $\tau = 100$.

absorption the surface albedo becomes again the most significant parameter for the measured signal (see channel ratios for 14/12 and 15/12).
For the low cloud at $ctp = 700hPa$ the mode is the parameter with the highest sensitivity. The impact of the cloud optical depth on the signal is quite low, due to the saturation of the cloud albedo, i.e. the top of atmosphere radiation is nearly unchanged for a cloud with $\tau = 110$ compared to a cloud with $\tau = 100$. In this optically thick regime the actual value of *cod* does not matter, but its distribution is quite important.

3.5 Cloud Vertical Extinction Profile

Retrieval of a cloud vertical extinction profile, here parametrized by the cloud vertical extent and the mode, requires a sensitivity towards these variables. Further, a change in the vertical extinction profile has to be distinguishable from a change in cloud top pressure by having different impact on the utilized spectral channels. In section 3.4 we did see, that in the presented cloud scenarios, the sensitivity can be as high for the mode as for the *ctp* and roughly half as high for the cloud vertical extent. In

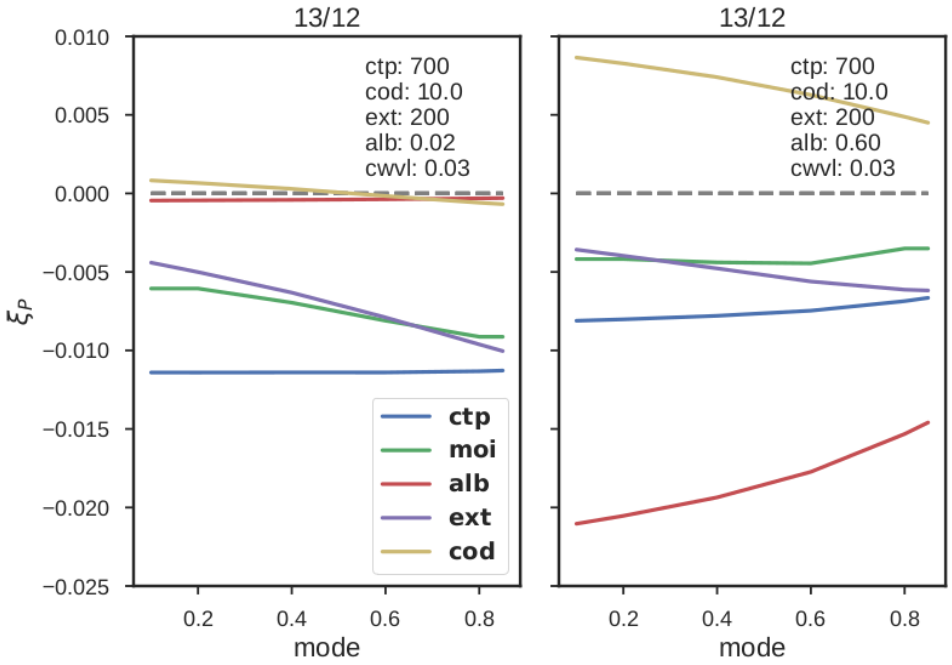

Fig. 3.7.: Sensitivities of TOA radiances depending on the vertical distribution of cloud optical depth for a cloud with $ctp = 700hPa$, $\tau = 10$, a vertical extent $ext = 200$ and an underlying surface with $\alpha = 0.02$ (left) and $\alpha = 0.6$ (right).

a next step, the sensitivity of all parameters is studied as a function of the mode, which is presented in figure 3.7.

The applied variations underlying the calculated sensitivities are the same as in section 3.4 and the sensitivities are in regard to the nominal centre wavelength of the channels, i.e. change of wavelength $cwvl = +0.03nm$, which is the nearest grid point in the look up table. All parameter sensitivities exhibit a similar behaviour across all channels and only differ in magnitude, therefore only the sensitivities for the ratio of channel 13 to 12 are presented, the other channel ratios are depicted in the appendix A.1 to A.4. In figure 3.7 a low cloud with top at $700hPa$ and bottom at $900hPa$ with an optical depth of $\tau = 10$ is depicted. On the left side the sensitivities belong to a cloud scenario above dark surface with $\alpha = 0.02$ and on the right to a bright surface with $\alpha = 0.6$. Comparison of both figures emphasizes the impact of the surface albedo on the sensitivity of cloud optical depth. The impact of the magnitude of the mode is contrasting for the cloud parameters. For the scenario with a dark surface, the sensitivity towards cloud vertical extent and mode increases when the distribution of optical depth is shifted lower in the clouds, i.e. with rising mode values. While a change of mode and extent by $10hPa$ induces a change of

-0.5% at the top of atmosphere signal for a cloud with the bulk of optical depth in the upper part of the cloud, the same change leads to decrease in TOA signal by up to 1%, when the optical depth is concentrated in the lower part of the same cloud. The change of sensitivity to the cloud extent can be explained by the position of the mode limiting the relative part of the extent affecting the measurement. For example, in the extreme case of an optically thick cloud with next to all optical depth concentrated at the coordinate of the mode, nearly all measured radiation would originate from scattering at this pressure level and therefore the vertical extent of the cloud below this point would be inconsequential to the measurement.
Moreover, the mode of optical depth is a relative parameter and a small change in the extent, which defines the sensitivity, also causes a shift in the absolute position of the mode. Thus, the sensitivity of the extent is made up by two parts, by the change in extent itself and by causing the mode to change as well, where the magnitude of the latter depends on the relative position of the mode. The sensitivity towards the extent for a cloud with mode $moi \approx 0$ would be made up solely by the expansion of the cloud, if the optical depth would allow any of the change in extent to be recognized. In this study, cloud optical depth is more evenly distributed as in the thought experiment, whereby the variation of extent not only modifies the mode but alters the distribution of *cod* inside the cloud further complicating the sensitivities. The sensitivity towards cloud top pressure as well as surface albedo is independent of the mode, while optical depth exhibits a minor decrease in sensitivity up to $moi = 0.6$, where the sign of the sensitivity switches. However, it should be noted that the sensitivity towards the optical depth is nearly non-existent in this scenario.

For the bright surface, the impact of mode on the albedo and cloud optical depth is more prominent. Both parameters experience a decrease in sensitivity with increasing mode of around $\Delta\xi_{alb} = 0.5\%$ and $\Delta\xi_{cod} = -0.5\%$. Also, the cloud top pressure shows a minor decrease in sensitivity by $\Delta\xi_{ctp} = 0.05\%$, while the sensitivity towards the mode is largely independent of the value itself in the range $moi \in [0.1, 0.6]$, followed by a small decrease by $\Delta\xi_{moi} = 0.06$ for higher mode values. The sensitivity to the cloud vertical extent has a smaller dependency on the mode as for the dark surface scenario with $\Delta\xi_{ext} = 0.25\%$. The sensitivities for a high cloud at 200hPa show similar behaviour as can be seen in the appendix figure A.5.
In figure 3.8 the sensitivities are depicted in dependence of the cloud vertical extent. In contrast to the mode of optical depth, when considering sensitivities for different cloud vertical extents, the cloud top pressure is affected. Where ξ_{ctp} did show minor to no response to different distributions of the optical depth, the geometrical thick-

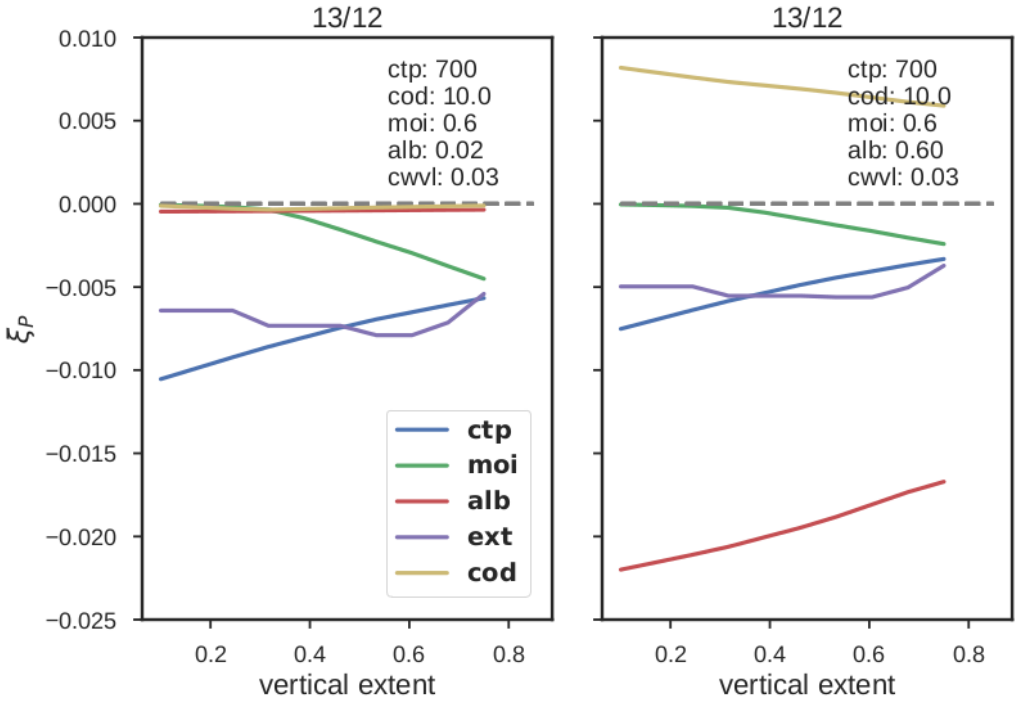

Fig. 3.8.: Sensitivities of TOA radiances depending on the vertical extent for a cloud with $ctp = 700hPa$, $\tau = 10$, a vertical extent $ext = 200$ and an underlying surface with $\alpha = 0.02$ (left) and $\alpha = 0.6$ (right).

ness has a significant impact on the TOA signal change accompanied by a change in *ctp*. In both scenarios, dark and bright surface, ξ_{ctp} decreases by $\approx 0.5\%$ with increasing geometrical thickness from $70hPa$ (*ext*=0.1) to $225hPa$ (*ext*=0.75). When neglecting the vertical extent in the forward model of a cloud top height retrieval the signal change with height will be overestimated, leading incorrect *ctp* values. Further, with increasing cloud extent the signal demonstrates a higher sensitivity towards a change in mode, but it should be noted again, that the absolute position of the mode depends on the vertical extent and therefore for each extent the absolute position of the mode is slightly different, while the relative position is constant at *moi*=0.6. Sensitivity ξ_{ext} shows a small increase at first with the highest sensitivity at *ext* $= 0.6$ and followed by a decrease in signal response. The step like behaviour of ξ_{ext} and ξ_{moi} can be contributed to the discrete nature of the atmosphere in the radiative transfer simulations, resulting in the cloud occupying the same amount of atmospheric layers for similar extent values. For example, if there are three atmospheric layer between cloud top and surface in the model, extents between 0 and 0.33 would always yield a cloud with an geometrical thickness corresponding to the

thickness of a single layer. This artefact is more pronounced for low clouds, where the same relative extent is coupled with a lower absolute geometrical thickness.
The results so far clearly demonstrate, that the measurement have significant sensitivities towards the cloud vertical profile, which depending on the cloud scenario can even exceed the sensitivity towards cloud top height. In a next step the feasibility of a retrieval of one or more parameters based on the information content of the spectral measurements has to be examined.

3.6 Degrees of Freedom

The degrees of freedom of a measurement indicates the amount of independent parameters that can be determined by the retrieval method for a specific state of the atmosphere. It provides information about practicability of a retrieval and can be used to optimize measurement instruments and the retrieval itself. The theoretical basis for the calculation of the degrees of freedom is provided by the inverse theory (see sec. 2.6). Here, only a brief overview of the theoretical basis is presented, for an exact derivation of the degrees of freedom Rodgers (2000) can be viewed.

Equation 2.17 describes the transition from the atmospheric state $\vec{x}$ to the measurement $\vec{y}$ by the Jacobian K. For the OLCI retrieval, the contents of $\vec{x}$ and $\vec{y}$ are presented in table 3.3. In a retrieval the aim is to find the state $\vec{x}$ that explains the measurement the best. Which is, for a Gaussian linear case, the state which minimizes the cost function:

$$\chi^2 = (\vec{x} - \vec{x}_a)^T S_a^{-1} (\vec{x} - \vec{x}_a) + \epsilon^T S_\epsilon^{-1} \epsilon. \tag{3.6}$$

with $\vec{x}$ and $\vec{x}_a$ as the state and the prior estimate of the state and S_a and S_ϵ the error covariance matrix of the prior knowledge and the instrumental noise, respectively. At the minimum the expected value of χ^2 is the degrees of freedom, which can be split into degrees of freedom for signal and a degrees of freedom for the noise.

$$d_s = \varepsilon(\vec{x} - \vec{x}_a)^T S_a^{-1} (\vec{x} - \vec{x}_a) \tag{3.7}$$

$$d_n = \varepsilon(\epsilon^T S_\epsilon^{-1} \epsilon) \tag{3.8}$$

Here, ε denotes the expected value operator. This can be further transformed by eliminating the state and prior state, yielding:

$$d_s = tr([K^T S_\epsilon K + S_a^{-1}]^{-1} K^T S_\epsilon^{-1} K) = tr(A). \tag{3.9}$$

vector	parameter
$\vec{x}$	*ctp*, *cod*, *moi*, *ext*
$\vec{y}$	normalized radiance of channel 12; radiance ratio of 13/12, 14/12, 15/12

Tab. 3.3.: State- and measurement vector of the OLCI cloud property retrieval.

The matrix A is called the averaging kernel and the trace of A yields the degrees of freedom for the retrieval.
The value of d_s depends on the prior uncertainties and the presumed noise of the signal, as well as on the state itself through the Jacobian. In theory, it is possible, that for some atmospheric states the retrieval can yield more parameters than for another atmospheric state. In the following results the degrees of freedom will show a distinct dependency on the underlying atmospheric and instrumental parameters.

3.6.1 Central Wavelength and Cloud Top Pressure

The study of the degrees of freedom for the OLCI cloud property retrieval is based on a synthetic state vector, where prior knowledge of *ctp*, *cod*, *ext* and *moi* is given together with the affiliated uncertainties S_a. In the case of all other parameters perfect knowledge of their quantity is assumed. The prior information is given by the arithmetic mean of each dimension, with the standard deviation as variances, which is not ideal for the cloud top height since mid-level clouds around 500hPa are the least common type. For the retrieval the cloud optical depth is given in by the logarithm to the base 10, which yields the as mean $\bar{\tau} \approx 10$. In figure 3.9 the degrees of freedom depending on the position of the central wavelength and the cloud top pressure are given. The regarded clouds had an optical depth of $\tau = 1.3$ and the surface underneath has an albedo of $\alpha = 0.01$. In all cases the degrees of freedom are the highest for low clouds and a shift of the central wavelength by $d_{wvl} = -1nm$. Higher values for mode and vertical extent leads to a more uniform dependence of the degrees of freedom on the wavelength and *ctp*. The degrees of freedom are nearly constant around a value of $d_s = 2$, i.e. two independent parameters can be determined when measuring an optically thin cloud above dark surface. For an optically thicker cloud with $\tau = 10$, the degrees of freedom are presented in figure 3.10. Here, d_s reaches values of up to 2.3, while the gradient along the (x,y)-plane is higher than for the thin cloud, ensuing that for optically thicker clouds the determinable number of parameters strongly depends on the cloud scenario. For even thicker clouds the degrees of freedom of the measurement can go as high as 2.4 (see app. A.6).
Analysis of the importance of surface albedo towards d_s is performed for two cloud top heights, at $800hPa$ and $200hPa$, with $ext = moi = 0.5$ at nearly nominal channel wavelength ($d_{wvl} = 0.03nm$) as presented in figure 3.11. Naturally, the impact of the surface albedo is most pronounced for optically thin clouds and close to non-

existent for clouds with $\tau = 100$ (purple lines). These results demonstrate, that a cloud retrieval with the oxygen A band can be complicated for optically thin clouds over bright surface, e.g. cirrus clouds over snow and ice, where $d_s(\alpha = 0.6) = 1.2$ indicates, that an accurate and simultaneous retrieval of cloud top pressure and optical depth is not possible.

The degrees of freedom demonstrate clearly, that for most cases a retrieval of more than two independent parameters will not be feasible. Furthermore, a retrieval of cloud extent and mode in addition to cloud top pressure and optical depth is even for the best case scenario impossible. However, since *ctp*, *ext* and *moi* are not independent properties some knowledge may be estimated if the conditions allow it. Also, cloud scenarios, where the sensitivity towards extent and mode is at a

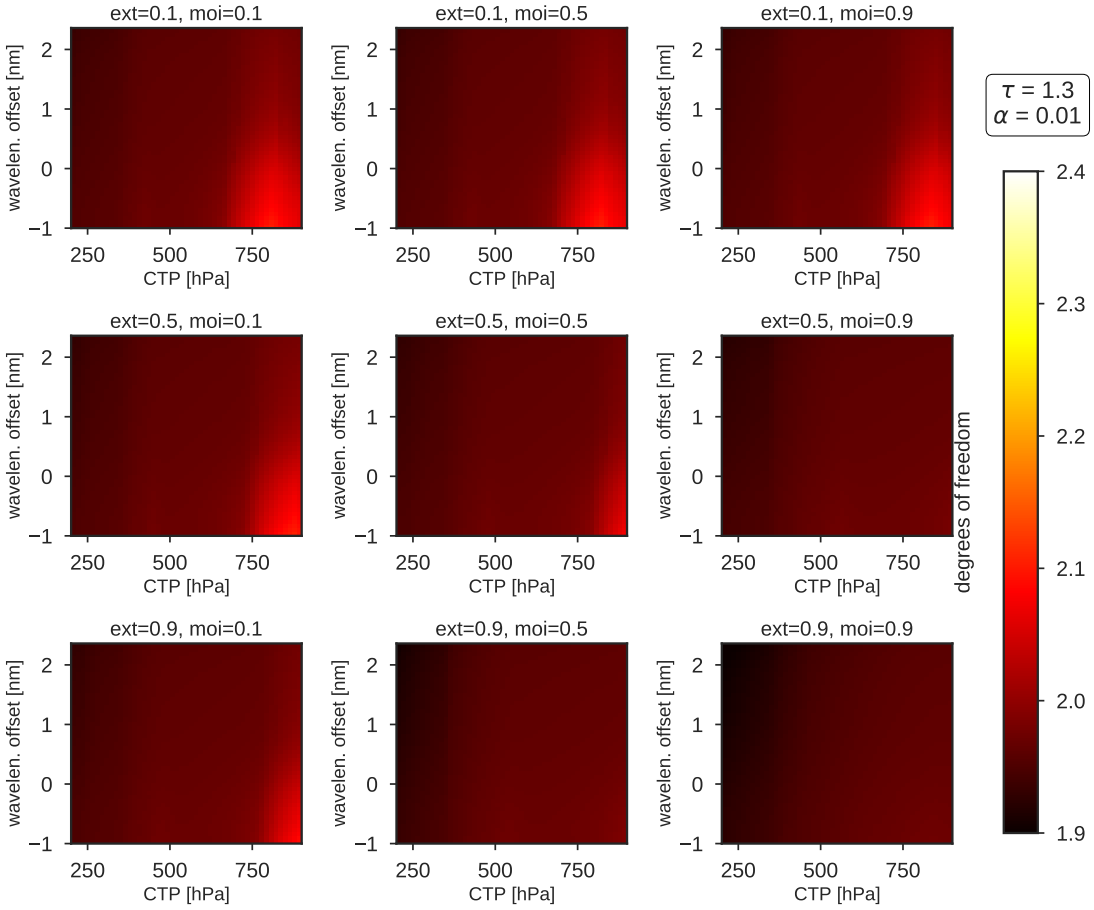

Fig. 3.9.: Degrees of freedom for a measurement of a cloud with $\tau = 1.3$ and surface albedo $\alpha = 0.01$ depending on the central wavelength of the OLCI channels as well as the cloud top pressure. The degrees of freedom are presented for different combinations of cloud vertical extent and mode of optical depth.

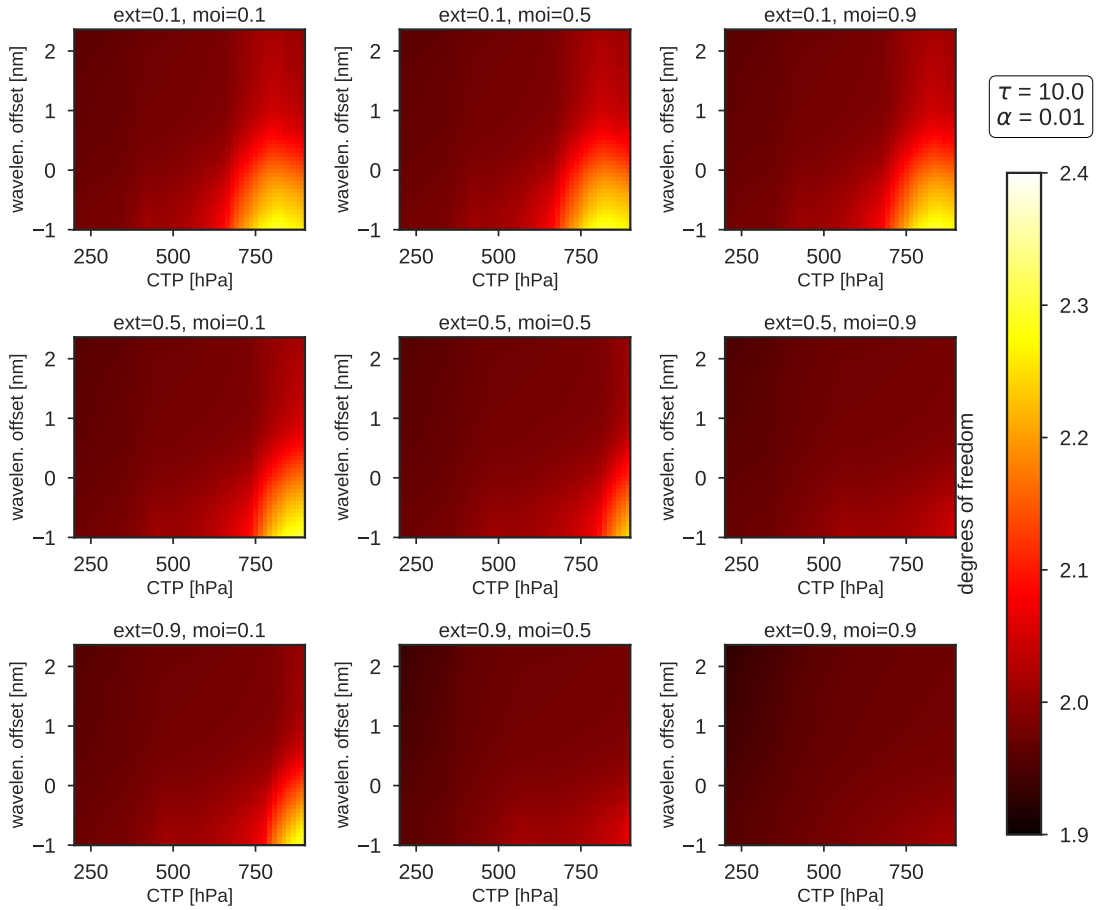

Fig. 3.10.: Degrees of freedom for a synthetic measurement of a cloud with $\tau = 10$ and surface albedo $\alpha = 0.01$ depending on the central wavelength of the OLCI channels as well as the cloud top pressure. The degrees of freedom are presented for different combinations of cloud vertical extent and mode of optical depth.

maximum, e.g. *ext* ≈ 0.6 and high values of moi, have degrees of freedom of $d_s \approx 2$ with almost no dependency to *ctp*, *cod* and central wavelength.

3.7 Conclusion

Sensitivities of the OLCI cloud property retrieval in the O_2 A band were studied regarding the impact of different cloud vertical profiles and central channel wavelength by means of radiative transport simulations. The applied parametrization for cloud vertical profiles introduced two additional parameters, mode and extent,

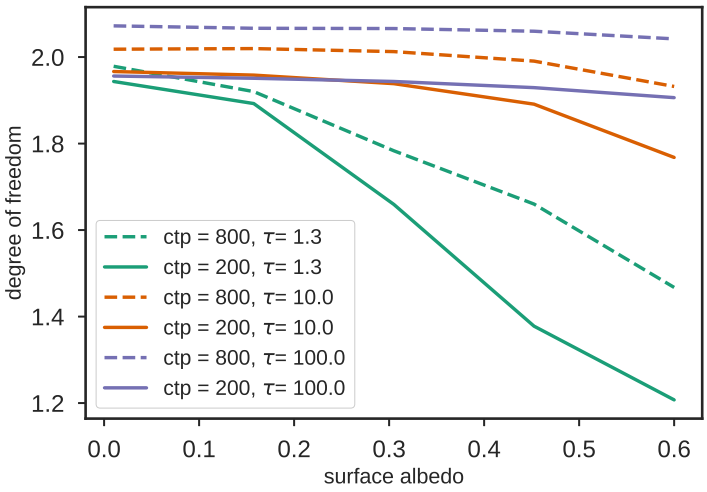

Fig. 3.11.: Degrees of freedom for a measurement of a cloud with varying τ and *ctp* depending on the surface albedo α. The degrees of freedom are presented for $ext = moi = 0.5$ and nominal channel wavelength ($d_{wvl} = 0$). Colors represent different cloud optical depth, while the solid and dashed lines are the cloud top heights of $200hPa$ and $800hPa$, respectively.

which create additional ambiguity in the retrieval. Here, the sensitivity of the measured top of atmosphere signal to the distribution of cloud optical depth inside the cloud was found to be nearly as high as the sensitivity towards the cloud top height. Both are important parameters, which have to be considered, even if the *ctp* is only of interest, since the effective cloud top pressure for OLCI is a combination of *ctp*, *ext* and *moi*. The sensitivity towards the cloud vertical extent was found to be in the order of $0.5\% - 1\%$ for channel ratio of 13/12 and is, depending on the cloud scenario, the parameter with the least impact on the top of atmosphere signal. However, the sensitivity towards the extent of the cloud depends strongly on the mode of optical depth and can, for high mode values ($moi > 0.7$), be as large as ξ_{ctp} and ξ_{moi}. Also, the sensitivity towards changes in *ctp* depends on the vertical extent of the cloud. If the assumed extent is to low in the retrieval and the underlying radiative transfer simulations, the channel ratio will be underestimated, leading to errors in the retrieved *ctp*.

Furthermore, the sensitivity towards surface albedo can be relatively large, especially for high and optically thin clouds, and thus uncertainties in the surface albedo can lead to large error in the cloud parameter retrievals. This can be especially a large source of error for regions with large annual deviations in the albedo. The use of

climatoligies is insufficient in those cases.
A degree of freedom analysis was performed, to obtain the number of independent parameters which can be retrieved with this method. The studied cloud scenarios indicated, that for most scenarios a maximum of two independent parameters can be retrieved. For low and optically thick clouds the degree of freedom reaches values of up to $d_s = 2.4$, demonstrating, that even in the best case scenario more than two independent parameters can not be retrieved. Further, the brightness of the underlying surface can have a strong effect on the degrees of freedom. Thus, the retrieval for optically thin clouds over a bright surface with $\alpha = 0.6$, exhibits degrees of freedom between $d_s(200hPa) = 1.2$ and $d_s(800hPa) = 1.5$, already complicating the simultaneous retrieval of cloud optical depth and cloud top height. However, cloud top pressure, vertical extent and mode are not independent parameters and some additional information may be retrievable. Also, the retrieval can be supported by additional measurements, e.g. in the thermal infrared, where the sensitivity towards the vertical profile is lower, which will be discussed further in chapter 5.

4 Classification of Clouds based on Texture Analysis

4.1 Introduction

In the last decades, the measurement of essential climate variables with satellite remote sensing has improved considerably. Thus, providing near real-time weather observations and long-term climate data records on a global scale with continuously improving accuracy. Especially, vertically resolved information about the atmosphere became available, because of the satellite based Cloud Profiling Radar (CPR) and the Cloud-Aerosol Lidar with Orthogonal Polarization (CALIOP) on board of CloudSat and CALIPSO, respectively. These two, combined with several other remote sensing instruments as payload on the satellite convoy A-train, increased the understanding of atmospheric processes greatly, supporting the development of weather prediction and climate models. However, even with ever improving instruments, the development of a remote sensing algorithm can be a challenge. The produced retrievals are still limited by the instrumental constraints as well as ambiguities in the origins of the signal change and varying sensitivities towards the parameter of interest depending on the atmospheric state.

The O_2 A band method for the retrieval of cloud top height and cloud optical depth was implemented as a prototype algorithm for the Medium-Resolution Imaging Spectrometer (MERIS) on board ESA's Environmental Satellite (ENVISAT)(Preusker et al., 2010). The accuracy of this remote sensing technique depends on the assumed vertical extent and vertical distribution of water inside the cloud (vertical extinction profile). In the past, the vertical extinction profile was often, due to a lack of opposing data, assumed to be homogeneous. This can lead to an incorrect cloud top pressure, because the proportion of in cloud scattering will be, depending on the actual profile, under- or overestimated. A study by Carbajal Henken et al. (2013) showed the impact on cloud top height retrieval when assuming an inhomogeneous vertical profile of cloud extinction from a CloudSat based climatology. Further, the possibility to exploit this dependency, by pairing O_2 A band measurements with

cloud top pressures from the thermal infrared, to estimate the vertical profile of the cloud has been investigated by Carbajal Henken et al. (2015).
MERIS successors the Ocean and Land Colour Instrument (OLCI) A and B on board ESA's Sentinel 3A and 3B feature the MERIS heritage channels, at $753.75nm$ and $761.25nm$, necessary for the cloud retrieval. Also, two additional channels inside the O_2 absorption band are available at $764.4nm$ and $767.5nm$ (see tab. 2.1).
Therefore a new cloud parameter retrieval using all the available OLCI channels inside the absorption band is in development. The capabilities of the advanced OLCI cloud property retrieval are studied in this thesis. In this chapter a predictor is presented, created to support the OLCI cloud parameter retrieval by delivering a priori estimates of the cloud vertical structure. This estimation is performed by the means of texture analysis of the vicinity of cloudy pixels in collaboration with a classification scheme providing a label related to specific cloud vertical parameters. This study is based on CloudSat retrievals of the vertically resolved cloud optical depth as well as CloudSat based cloud classifications and MODIS calibrated and georeferenced top of atmosphere radiances.
In section 4.2 the texture analysis with the grey-level co-occurrence matrix is described and the random forest based classification method will be introduced. The underlying data products are presented in section 4.3. Further, in section 4.4, the performance of the classification into well-known cloud types and into cloud vertical profiles is analysed, with focus on the optimization of the classification accuracy. Finally, in section 4.6 conclusions are given.

4.2 Method

The texture of an image can be described as the spatial order of colours or intensities and is a widely used metric for analysis of images as it describes the variation of physical quantities in optical as well as non-optical, like MRI, images. There are multiple statistical methods to retrieve parameters describing the texture of an image and several studies have been performed to detect and distinguish clouds through one or more of these image statistics in satellite remote sensing (Kittler and Pairman, 1985)(Ebert, 1987)(Ebert, 1989)(Welch et al., 1988) and with ground based instruments (Heinle et al., 2010). In the past of satellite remote sensing, especially grey-level difference vector (GLDV)(Khazenie and Richardson, 1993), grey-level co-occurrence matrix (GLCM)(Haralick et al., 1973) and Fourier transform analysis (Augusteijn et al., 1995) were successfully applied to perform land cover

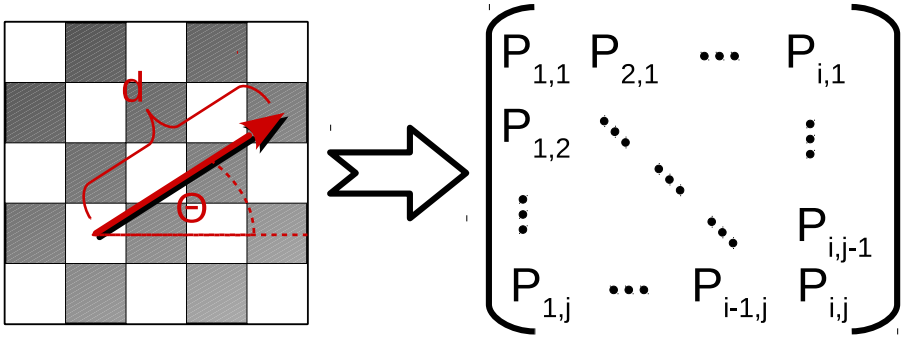

Fig. 4.1.: Schematic for grey level co-occurrence matrix calculation. The GLCM is always a quadratic matrix with i=j and maps the co-occurrence of the grey level values at distance d and angle θ towards each other.

and cloud classifications. The results of this study are based on the grey-level co-occurrence matrix method. In section 4.2.1 the basic theory of the GLCM will be presented and in section 4.2.2 the applied classification scheme of a random forest algorithm is introduced.

4.2.1 Grey-Level Co-Occurrence Matrix

The GLCM (Haralick et al., 1973) method is a second order statistical measure mapping the paired grey-level occurrences of an image, or part of an image, resulting in an $(m \times m)$ Matrix. The dimension m of the quadratic matrix M is given by the number of possible grey-levels in the image. The individual matrix elements $P_{i,j}(d,\theta)$ are representing the frequency of intensity i occurring next to intensity j under the condition of distance d and angle θ between both points in the image(see figure 4.1). Depending on the applied convention, the GLCM can be calculated considering the spatial order of the pixel i.e. $\theta \neq \theta + \pi$. If the spatial order is ignored, the GLCM is always a symmetrical matrix $P_{i,j} = P_{j,i}$. The main diagonal of M represents image pixels of the same intensity appearing under the set conditions, while each parallel running diagonal at a distance k contains all pixel with grey-level difference of $i - j = k$. In the literature one often finds the normalized grey-level co-occurrence matrix, which normalizes the co-occurrence frequencies with the

number of image pixels, yielding values between 0 and 1. An advantage of this form is, that co-occurrence values can be interpreted as probabilities.
Another variable impacting the texture parameters is the window size w, defining the part of the image for which a GLCM is calculated. In this context window size means the size of the applied mask around the examined pixel. Is the chosen window size too small, large scale textural features of clouds may be omitted. A window, which is to large, can include other cloud types contaminating the texture parameters. Both cases can lead to misinterpretation by the classification algorithm. There seems to be no window size which is effective for every scene. Different window sizes were tested in this study. For convenience, quadratic window sizes were used. The results will be presented in section 4.4.1.
The co-occurrence matrix records the texture of an image but is too bulky for further evaluation. Instead, several texture properties can be calculated for a GLCM, condensing the amount of information in a suitable form:

$$energy = \sqrt{\sum_{i,j=0}^{m-1} P_{i,j}^2} \tag{4.1}$$

$$contrast = \sum_{i,j=0}^{m-1} P_{i,j}(i-j)^2 \tag{4.2}$$

$$homogeneity = \sum_{i,j=0}^{m-1} \frac{P_{i,j}}{1+(i-j)^2} \tag{4.3}$$

$$correlation = \sum_{i,j=0}^{m-1} P_{i,j}[\frac{(i-\mu_i)(j-\mu_j)}{\sqrt{(\sigma_i^2)(\sigma_j^2)}}] \tag{4.4}$$

$$dissimilarity = \sum_{i,j=0}^{m-1} P_{i,j}|i-j|. \tag{4.5}$$

Here, μ_i, μ_j denotes the means along the respective column/row and σ_i^2, σ_j^2 the affiliated standard deviations.

4.2.2 Random Forest Classification

Classification algorithm are a common tool in science, if it is convenient to sort data based on a set of features. Several well-established classification techniques

exist and are supported in the most common software repositories like, naive Bayes, decision trees, random forest, k-nearest neighbours and support vector machines, just to name a few examples. Classification methods usually makes use of a set of training data, which includes the features and the already known labels for each data point, establishing a model based on the training set, which can be used to predict new objects. In this study a random forest classifier (Breiman, 2001) was applied to assign each cloudy pixel a cloud class or a cloud vertical extinction profile based on associated texture parameters. The random forest algorithm, is an ensemble learning method for classification and regression based on decision trees. One of the virtues of this classification method is, that it is robust to overfitting the data. While for decision trees overfitting can be a problem, the creation method of random forests prevents it. In principle, for a random forest classifier, n decision trees are created, each with a random generated subset of the training data. The order of decision nodes is, similar to decision trees, determined by a best split method like information gain or gini impurity. However, since only a random subset of features is used in setting up the forest, the sequence of nodes will vary from tree to tree. In this study the used split function was the gini impurity, which is defined as:

$$I_G(p) = 1 - \sum_{i=1}^{J} p_i^2. \tag{4.6}$$

Where J is the number of classes going into the classification and p_i is the probability of an item with label i being chosen. Smaller gini impurities for a feature at a node means, that the possibility of wrongly classifying the item based on this feature is lower. Therefore, the feature order for the nodes is going from smallest gini impurity, for the first node, to largest gini impurity, for the last node.
For training 70% of the available pixel were used, the remaining 30% were reserved for testing.

4.3 Data Basis

As basis for the study level-1b granules of the MODIS instrument on board the Aqua satellite were used. The scenes are limited to the northern Atlantic in the year 2008 for the main part of the study, but include different surface types distributed over the globe for section 4.5, where the influence of the cloud texture background is evaluated.
The used spectral channels are Band 1 at $620nm - 670nm$ and a spatial resolution

of 250m and channel 17 at $890nm - 920nm$ with a spatial resolution of 1km. In this study, we limited the spectral region to the visible and near infrared, since the algorithm, as an OLCI CTP preprocessor, can only make use of the available wavelength between $400nm - 1020nm$.
Information about the vertical structure of the clouds and the cloud class are based on the CloudSat products 2B-TAU (Polonsky et al., 2008) and 2B-CLDCLASS release version 4 (Sassen and Wang, 2008), respectively. Both satellites are part of the Afternoon Train (A-Train) constellation with a temporal shift of 2.5 minutes between each other. CloudSat's TAU products provides the total optical depth, the mean effective radius of hydrometeors in the atmospheric column, as well as optical depth distributed for 125 atmospheric layers based on the radar back scatter, MODIS up-welling reflectivity at the top of atmosphere and auxiliary data. The vertical resolution of the product is at 240m, however it should be noted that for the 4-5 bins above surface, which is normally at bin 104/105, the radar sensitivity is greatly reduced due to surface clutter. Therefore, measurements up to height of $1km$ have to be used with caution, especially over land.
The CLDCLASS product categorizes clouds into in one of the following 8 classes: stratus (St), stratocumulus (Sc), cumulus (Cu), nimbostratus (Ns), altocumulus (Ac), altostratus (As), deep convective, or high clouds (cirrus) based on radar backscatter as wells as MODIS measurements and the European Centre for Medium-Range Weather Forecasts (ECMWF) predictions. Further product details can be found in the product process description (Wang and Sassen, 2007). Of important note is, that the cloud classification is partly based on textural features derived from MODIS. Therefore, a cloud typing based on texture alone, with CloudSat as truth, can not be a proof of concept, but will be used as a safety check and benchmark for optimization of the implementation for further studies. Moreover, in the considered regions for the time period no clouds were classified as stratus (St) by CloudSat.
Since we are using CloudSat data as reference, we are limited to near nadir viewing angles for the MODIS radiances and only classifications for the nearest neighbour pixels are performed. The maximum allowed distance between Cloudsat and MODIS measurement is given by half the spatial resolution of the latter.
Since the focus of this work is a possible classification of cloudy pixels into a cloud class and a cloud vertical extinction profile only cloudy pixels were studied. However, this means that the pixel of interest (center pixel of applied mask) in each analysis step has to be cloudy, inside the applied mask all pixel, whether cloudy or not, were included in the analysis. The applicability of this method as means for cloud detection was already studied extensively in the past e.g. (Schröder et al., 2002). Therefore, we used the cloud optical depth as provided by the CloudSat

2B-TAU product as a proxi cloud mask. For processing only points where $\tau > 0$ are considered.

4.4 Analysis

From the grey-level co-occurrence matrix multiple texture describing features can be calculated, which is computationally the most time-consuming part of the analysis. Therefore, a major concern when working with GLCM is computational effort. In order to speed up processing times and optimize classification performance the impact of all settings on the performance of the GLCM has to be examined. Finding a set of optimal parameters means, ensuring good classification results while shortening algorithm runtime. This can be achieved by either reducing the surveyed pixels by keeping window sizes for the GLCM small, reducing the employed spatial resolution of the original image, reducing the radiometric resolution of the raw data or identifying and removing unimportant texture features for the classification. In section 4.4.1 the influence of the chosen window size for MODIS Band 1 and 17 is studied regarding the classification accuracy of image pixels in cloud types. Further, the impact of spatial resolution is observed by artificially increasing the pixel size of Band 1 from $250m$ to $1km$.
As mentioned, the maximum number of grey-levels of the image directly scales the size of the GLCM. A high signal resolution often leads to a large matrix with a small portion of elements being non-zero. Therefore, a reduction of grey-levels can be performed with minor loss of information. The impact of grey-level reduction is examined in section 4.4.2.
The distance between pixel as basis for the calculation of the grey-level co-occurrence matrix was studied in section 4.4.3. Moreover, the classification into cloud types is viewed in detail in section 4.4.5 followed by the classification into classes with distinct cloud vertical extinction profiles in sec. 4.4.6. Performance is rated on the basis of the average (total) classification accuracy, given by the mean accuracy of prediction:

$$R^2 = 1 - \frac{\sum_i^n (y_i - f(\vec{x}_i))^2}{\sum_i^n (y_i - \bar{y}_i)^2}, \tag{4.7}$$

with y, $\bar{y}$ being the true labels, mean of true labels and $f(\vec{x}_i)$ the predicted labels based on the feature vector $\vec{x}_i$. Furhter, the individual hit rate for the corresponding classes will be examined in detail.

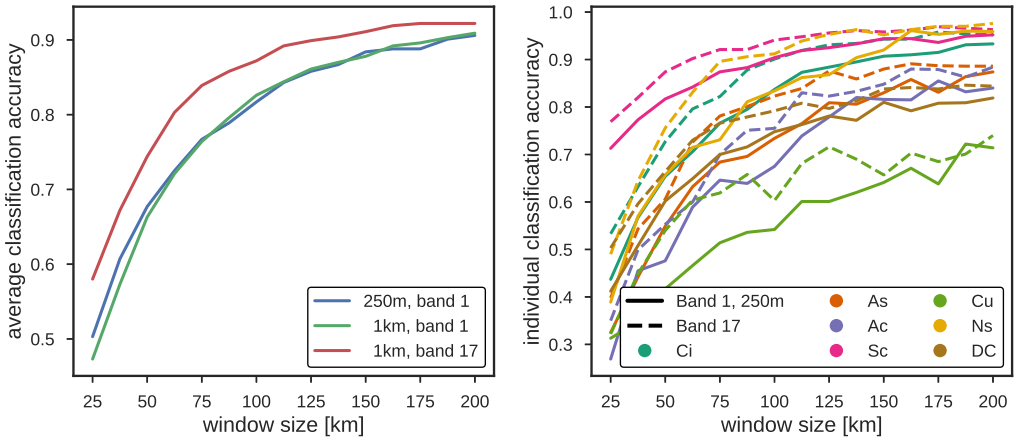

Fig. 4.2.: Left: Total classification accuracy for different window sizes. Classification was performed for Band 1 250m (blue), artificially binned 1km (orange) resolution and Band 17 (green). All grey-level co-occurrence matrices are calculated with $d = 2$, $\theta = 0$ and $g = 8$. Right: Classification accuracy separated for each cloud type.

4.4.1 Window Size and Resolution

For the described method of the GLCM an image region for the texture analysis has to be defined. The used size w has not only an effect on the further classification accuracy, but also reduces the amount of data to be processed. When applying this method image pixel at a distance towards the image border, smaller than half the window size are lost in processing, since the mask can not be applied to these regions. Thus, the processable image is smaller than the original. In this work only the nadir view of MODIS and it's direct vicinity is examined, leading to loss of pixel only in the along track direction.

Window size investigation has been performed for MODIS band 17 in its $1km$ spatial resolution and for band 1 in 250m full resolution as well as a reduced resolution of 1km. The coarser resolution was acquired through interpolation of the band 1 radiance on the 1km$\times$1km geolocation grid for MODIS Aqua.

Figure 4.2 shows the results for all three spectral channels with regard to the applied window. The maximum number of grey-levels m was reduced to $m = 8$ and the distance between pixels was set to $d = 2$. All GLCMs in this study were calculated for $\theta = 0$, since no angular dependency for the classification could be determined in advance. The angular independence of the grey-level co-occurrence matrix for cloud classification was also found in another study by Khazenie and Richardson (1993).

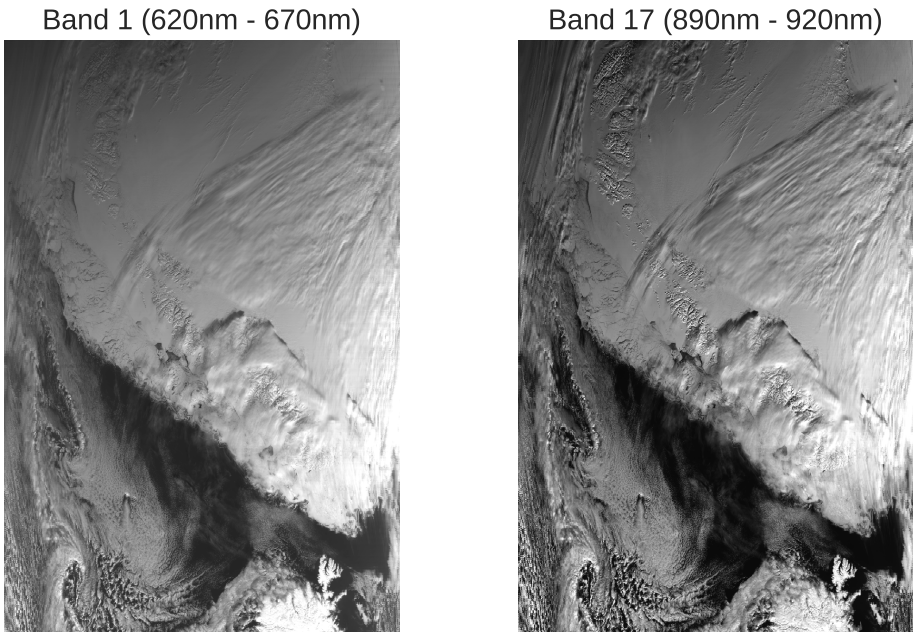

Fig. 4.3.: Comparison of grey-level image of MODIS Aqua Band 1 (left) and Band 17 (right) over snow covered surface. Band 17 exhibits a higher contrast especially around clouds. Coarse parts of the images are caused by saturation of the instruments channels.

The spatial resolution of $250m$ from band 1 demonstrates no classification benefit at all window sizes towards the $1km$ binned version. Overall, Band 17 exhibits the highest total classification accuracy, which we hypothesize to be caused by the water vapour structures visible through the H_2O absorption band around $900nm$. When comparing the grey-level images of band 1 and 17 in figure 4.3 for a cloud scene above snow, the increased contrast for clouds in the image taken at $900nm$ is easily visible with the eye. The higher contrast is attributed to the increased water vapour in the vicinity of clouds and influence the retrieved texture parameters improving differentiation between cloud types. The percentage of right predicted classes is around $50\% - 60\%$ for small window sizes of around $25km$ and increases rapidly with growing edge length. At a size of around $120km$ the total hit scores begin to saturate around $85\% - 90\%$ correctly classified clouds, depending on the used spectral band. With an edge length of 120km already 7.5% of the image have to be

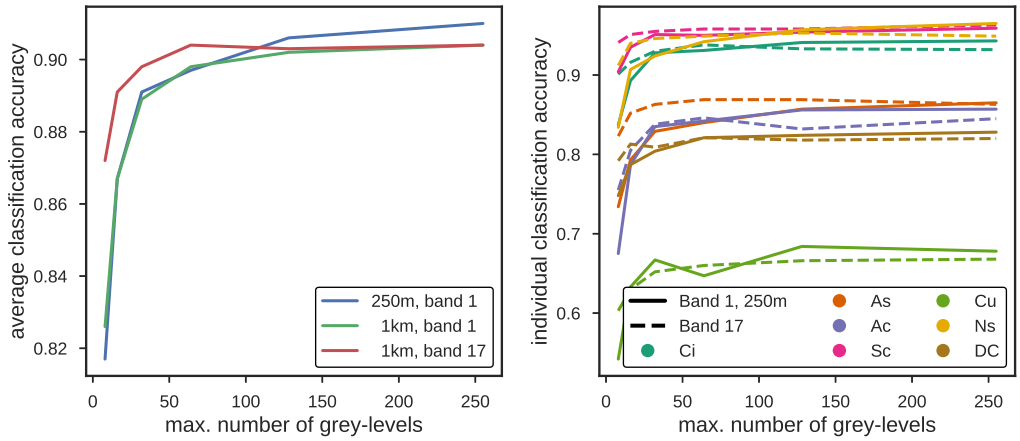

Fig. 4.4.: Classification accuracy for band 1 and band 17 depending on the maximum number of grey-levels (left). Individual classification accuracy for each cloud type. Solid lines represent the classification with texture parameters from band 1 in full resolution, dashed represent band 17.

disregarded for analysis as border pixels.

In detail, the hit scores for the seven cloud classes varies strongly. On the right panel in figure 4.2 the classification performance is separated. The solid lines depict classification based on band 1 ($250m$), while the dashed lines represent band 17. The difference between band 1 and band 17 is consistent with behavior of the total hit scores for all cloud classes. The random forest classifier displays a hit score around 60% for cumulus clouds, which is by far the smallest for all cloud scenarios.

4.4.2 Maximum Number of Grey-Levels

MODIS provides the radiance measurements for each channel as a scaled integer ranging between $0-32767$, while the employed grey-level co-occurrence Matrix from the python module sklearn (http://scikit-learn.org/) can only handle a maximum number of grey-levels of 256. As mentioned above, exploiting the complete range in grey-levels leads to a matrix of the size 256×256 for each pixel of the image. Therefore, to further reduce computational effort the impact of grey-scale resolution towards classification is examined. Using the best set of parameters previously found, the maximum number of grey-levels is artificially reduced to find a compromise between classification accuracy and algorithm run-time.

In figure 4.4 the associated classification results are depicted. The impact of grey-level range is more pronounced for band 1, where a maximum of classification score is reached when exhausting the algorithms limits. For $g < 90$ the use of the full resolution yields no advantage for the classification of cloud types. However, when using more than $g \approx 90$, a minor difference between full and reduced resolution of band 1 becomes apparent, whereby image statistics on a spatial resolution of $250m$ leads to a slight increase in classification accuracy by up to 1% at $g = 256$. Band 17 on the other hand shows an increase with rising numbers of grey-levels below $g = 64$, beyond that the hit score is nearly constant. Looking at the individual classification accuracy the impact of grey-level resolution is noticeable for band 1 based classifications (solid lines). While for most clouds types the classification accuracy increases with larger number of grey-levels, with the largest impact for Ns, As and Ac types, the band 1 classification for cumulus clouds exhibits a local minimum at $g = 64$. Based on these results $g = 64$ is a sufficient brightness resolution for band 17 and is only slightly worse in terms of classification score ($< -1\%$) as band 1 with $g = 256$. For band 1, a resolution of at least 128 different grey-levels should be chosen, to avoid the drop off in classification for cumulus clouds and still have a similar total accuracy to band 17. This leads to bigger GLCMs, by a factor of 4, slowing down processing times considerably.
A parameter, which could not be studied in this work is the viewing geometry of the satellite. Due to CloudSat as reference viewing angles are limited to the nadir view and a change in observed texture by different viewing angles can therefore not be observed. The observed cloud texture is not only caused by the horizontal structure but also by the verticality and 3D effects could impact the dynamic range of grey-levels for cloudy pixels and can change the optimal number of grey-levels for the classification depending on the viewing angles.

4.4.3 Inter-Pixel Distance

The last adjustable parameter for the grey-level co-occurrence matrix to be considered is the spacing between grey-level pairs. For highly structured images the distance can have strong positive or negative effects based on the orientation of the texture. In the case of texture analysis of cloud fields the scenes are very variable with no constant distance in structures visible. Therefore, the distance should have a negligible influence on the texture parameters and thereby on the random forest classification. Figure 4.5 left panel depicts the average accuracy in dependence of the inter-pixel distance. Here, the spatial resolution is the decisive value. The

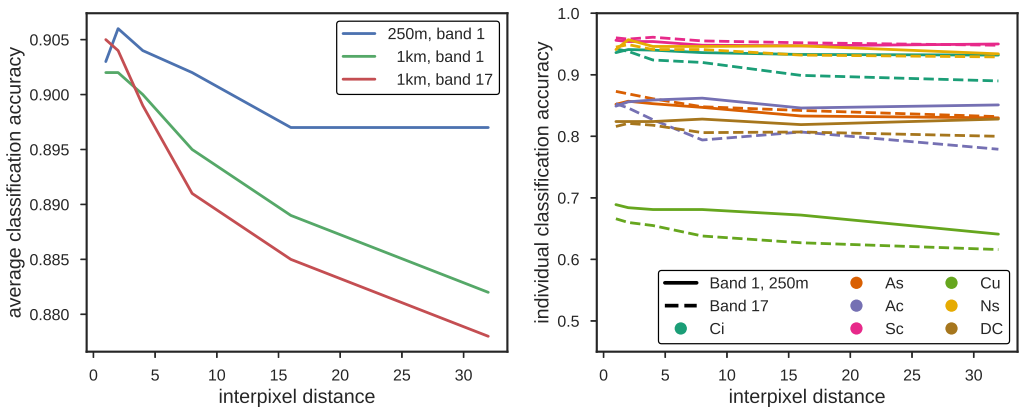

Fig. 4.5.: Classification accuracy for band 1 and band 17 depending on the inter-pixel distance (left). Individual classification accuracy for each cloud type. Solid lines represent the classification with texture parameters from band 1 in full resolution, dashed lines represent band 17.

radiance measurements with a spatial resolution of $1km$ exhibit a stronger decrease in classification accuracy than the $250m$, for which the inter-pixel distance is not as important. While smaller distances seem to perform better for all spectral bands the range of variation is around 2% for the 1km data between distances of 1 pixel and 32 pixel. Making the inter-pixel spacing by far the parameter with the smallest impact in this study. The individual cloud types, as shown in figure 4.5 right panel, depend only slightly on the inter-pixel distance. The importance of inter-pixel distance is stronger for cumulus clouds as for the other classes with a difference of up to 5% between $d = 1$ and $d = 32$. For cases with cumulus clouds the results suggest the use of small spacing to improve classification accuracy by several percents.

4.4.4 Importance of Texture Features

Up to this point all of the texture parameters introduced in equation 4.1-4.5 were included in training and testing of the random forest. However, not all parameters may have the same significance to the classification, which is examined in the following.

The importance of a textural feature for the classification can be derived through the so called gini importance. It is defined as the decrease in impurity (missclassifications) of a decision node averaged over all trees for each feature. Higher values represent a more important feature for the decision trees, because those features

	feature importance				
Band	energy	contrast	homogeneity	correlation	dissimilarity
1 (250m)	0.211	0.192	0.193	**0.231**	**0.173**
1 (1km)	0.230	0.193	0.197	**0.230**	**0.171**
17	0.216	0.198	0.197	**0.216**	**0.183**

Tab. 4.1.: Feature importance for the previously found optimal set of window size, inter-pixel distance and grey-levels. Each feature importance is normalized. The highest and lowest feature importance of each band is presented in bold.

reduce the number of missclassification the most. The calculated feature importance are presented in table 4.1 as normalized values, i.e. the sum of all feature importances is 1. In this study, the order of importance is independent of the used spectral band. The correlation between grey-levels is always the most important feature, followed by the energy, the contrast, the homogeneity and the least important feature is the dissimilarity. Moreover, all features have similar gini importances, i.e. no value is low enough to warrant dismissal of the feature all together. Therefore, all texture features (eq. 4.1-4.5) will be included for the remainder of this study.

4.4.5 Classification into Cloud Types

Running the classification algorithm with the previously found set of optimal parameters leads to very similar results for band 1 and band 17. In figure 4.6 (left) the classification results based on band 17 ($g = 64$, $d = 2$, $w = 125km$) are presented. Prominent features are the missclassification of every type towards stratocumulus and deep convective clouds (horizontal lines), i.e. in most cases, where the random forest classifier and the CloudSat cloud class don't agree, the random forest algorithm tends to classify those scenes to be either Sc or DC. As seen before, the cloud typing of cumulus clouds is the most uncertain of all classes, where around 22% are classified as Sc and 6% as deep convective clouds. DC in itself is the second worst classified cloud type in this study with a classification accuracy of 82%. One possible explanation for that could be, that deep convective clouds in their dissipating stage, occur along with cirrus clouds leading to a mix of textural features retrieved from both types, challenging the classification algorithm.
In figure 4.6 (right) the differences in performance between band 1 and band 17

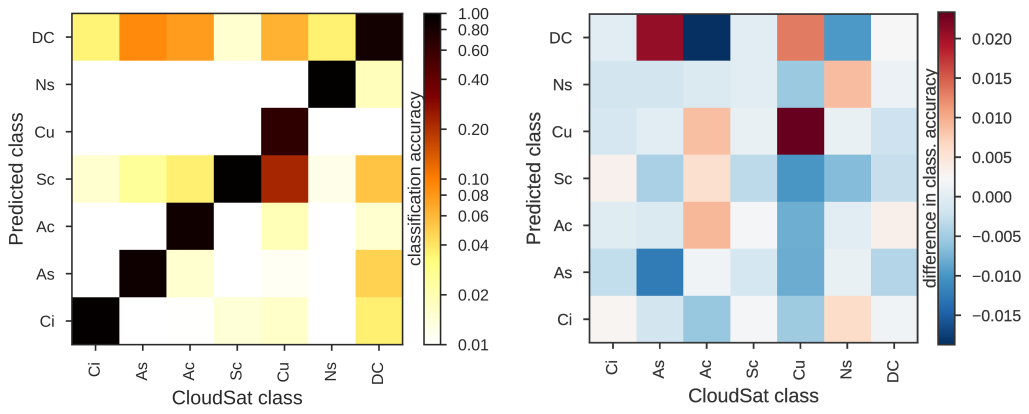

Fig. 4.6.: 2D-histogram of texture based cloud typing. Left: classification scores for classification by radiation from band 17. The CloudSat cloud type is along the x-axis, the predicted class through the random forest classifier along the y-axis and the classification score is shown in colour. The histogram is normalized for each column. Right: difference in classification accuracy for band 1 and band 17. Positive values (red) correspond to higher hit scores for band 1 negative (blue) to higher scores for band 17

classification is visible. For the most part both spectral channels lead to similar results, except for cumulus clouds, where classification based on band 1 textural features is 2.4% more accurate. The combination of both spectral channels and the associated textural features has shown no improvement in classification. Following the classification is performed into cloud classes based on the vertical extinction profile, as measured by CloudSat.

4.4.6 Estimating Cloud Vertical Extinction Profile

The cloud typing results demonstrate, that we can reproduce CloudSat's classification without making use of vertical information with a satisfactory accuracy. Cloud vertical structure is an important property for passive cloud top height/pressure retrievals and a major source of uncertainty. Active remote sensing techniques have a high sensitivity to small optical depths and therefore sense the cloud top height when few hydrometeors being present. Often retrievals of the passive kind refer to an effective cloud top height taking into account the penetration depth into the cloud of the respective method. Depending on the vertical extinction profile of a cloud the effective cloud top height can vary, while the actively sensed cloud top may remain the same. In order to correct the effective cloud top height, knowledge of

the vertical structure is needed. While a reliable cloud typing into the ISCCP classes (Rossow and Schiffer, 1999) and associated standard vertical extinction profiles is a possibility, all of the 9 ISCCP cloud types show large variations in their vertical structures (Carbajal Henken et al., 2014). In our proposed method, we skip the classification into cloud classes and directly link the horizontal structure of clouds to the vertical profile identical to the work in section 4.4.5.

For this part of the thesis, the cloud vertical extinction profiles are retrieved from CloudSat's 2B-TAU product. We included only cases, where at least 3 adjacent vertical bins had a cloud optical depth of $\tau > 0.1$. In order to reduce the dimensionality of the problem we used the parametrized description of the vertical extinction profile given by a relative vertical extent and the mode of the distribution of cloud optical depth based on a beta function (see. section 3.1 for a detailed description). This representation together with the condition of at least 3 cloudy layer often leads to clouds with $moi = 0.5$.

Further simplification is performed by clustering all cases into classes based on their extent and mode. The clustering was performed using the k-means method as well as a manual discretization. The difference in clustering of the data points is shown in figure 4.7 (right column). In the case of 3 distinct classes, rather than separating classes along cloud modes or along the extent, the k-means method creates non-intuitive separations: one class for modes ranging from 0 to ≈ 0.5 containing all vertical extents and 2 smaller classes for $moi > 0.5$ split into small and large vertical extents. In contrast to the unsupervised scheme, the manual separation was performed once at evenly spaced values between minimum and maximum value of the respective dimension, leading to $0 \leq C1 \leq 0.33 < C2 \leq 0.66 < C3 \leq 1$ in the case of three classes for the mode. The separation based on the extent was performed in the same manner on the interval $(0, 0.7]$, containing all extent values present in the data.

The classifications using optimal parameters for all clustering methods are depicted in figure 4.7. As before, band 1 and band 17 showed only minor differences in classification results, therefore only the results for band 17 are presented. Optimization was performed as shown above. All hit scores (individual and total) are presented in table 4.2.

Evidently, an intuitive clustering along the extent performs the best for classification, followed by the k-means method. The total accuracy to predict the right class is 14% higher for the extent separated case than for the k-means, which in turn is 8% more accurate than the classes with discrete modes. In detail the separation into classes defined by their relative vertical extent has individual classification accuracy

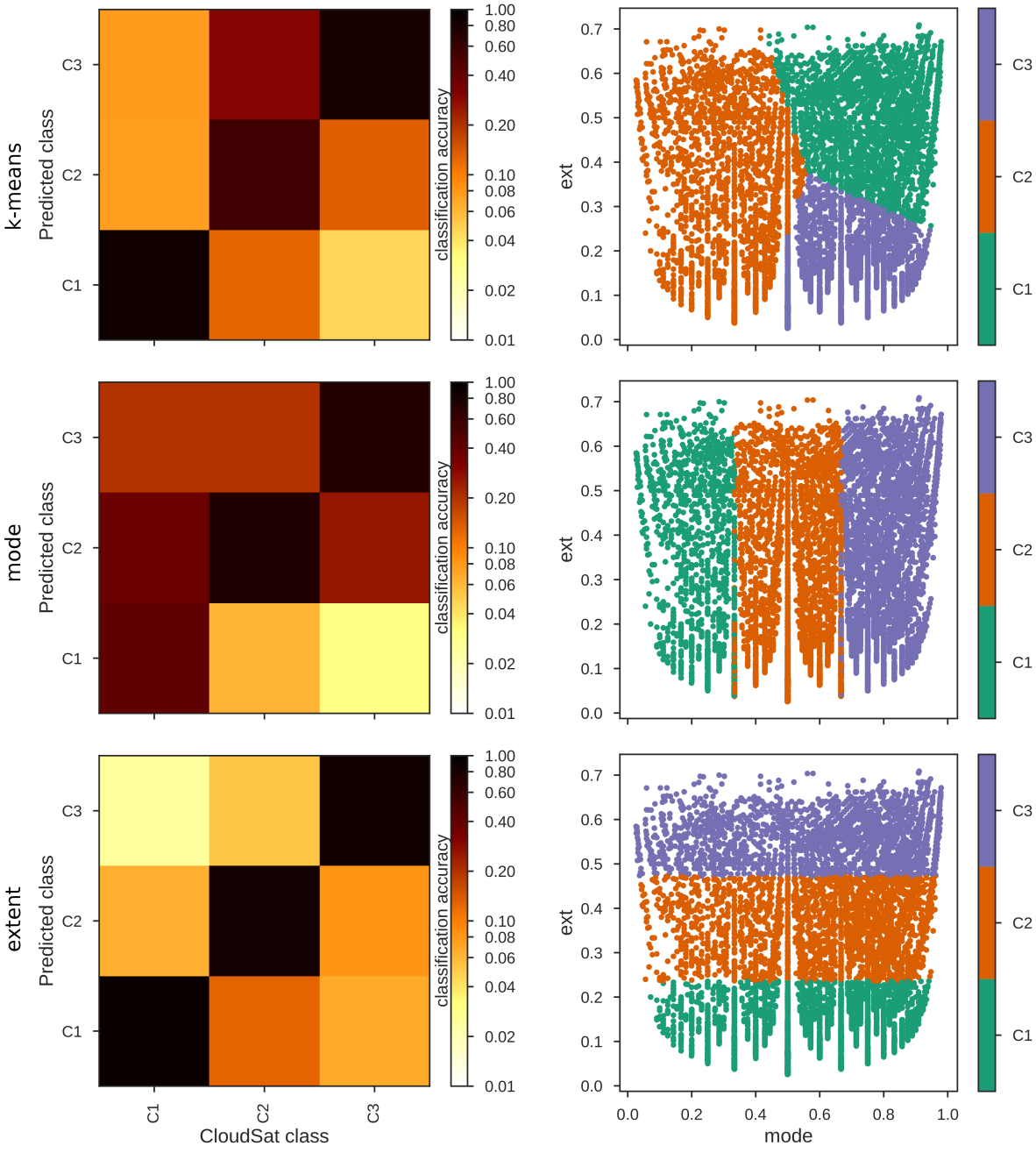

Fig. 4.7.: Top: 2D-histograms of the classification accuracy for 3 clustered classes. Bottom: Clustered data points for classification into three classes through (left) k-means clustering, (middle) manually along the mode of optical thickness and (right) along the relative vertical extent.

	C1	C2	C3	total
k-means	0.451	0.729	0.737	0.696
mode only	0.584	0.837	0.868	0.777
extent only	0.940	0.916	0.842	**0.918**

Tab. 4.2.: Classification accuracy of individual classes and total for k-means clustered and manually clustered data points.

ranging between 84.2% and 94.0%, while classes defined by mode values has high probabilities to detect C2 and C3 with 83.7% and 86.8%, but fails to consistently detect C1. The k-means based assignments shows high scores for classes C2 and C3, both with high values for the mode and separated by the cloud vertical extent. Class C1, which envelops all possible extents, is most often misplaced. The results for the manually grouped data-sets are in agreement with the k-means results in so far as classes separated by the extent are more reliably classified.

When the number of classes is increased for each separation scheme the associated classification accuracy decreases, as can be seen in figure 4.8. Increasing the number of possible labels simultaneously increases the possibility to wrongfully classify a difficult case by chance. For the manually grouped data-sets, a number of two different classes naturally exhibits even higher classification scores, while k-means shows a decrease in overall performance for two labels compared to three. The classification by extent appears to be more robust towards the addition of classes with a decrease in total classification accuracy by 13% compared to the decrease by 17% and 24% for the k-means and mode clustered cases, respectively. The number of labels one should use is highly dependent on the intended use of the assigned labels, e.g. as first guess for an optimal estimation three distinct labels can already have a positive impact on further retrievals if otherwise there is no vertical information. On the other hand, if the geometrical thickness of a cloud should be estimated based on the texture, the cloud top height has to be known, since in this work extent and mode are defined as relative parameters. Assuming an exemplary cloud with top at $800hPa$, the texture based geometrical thickness for a case with three distinct classes can only be estimated with an accuracy of $216hPa$. Doubling the amount of classes changes the probability of assigning the right class to approximately 82% and increases the accuracy of estimated cloud geometrical thickness to $108hPa$.

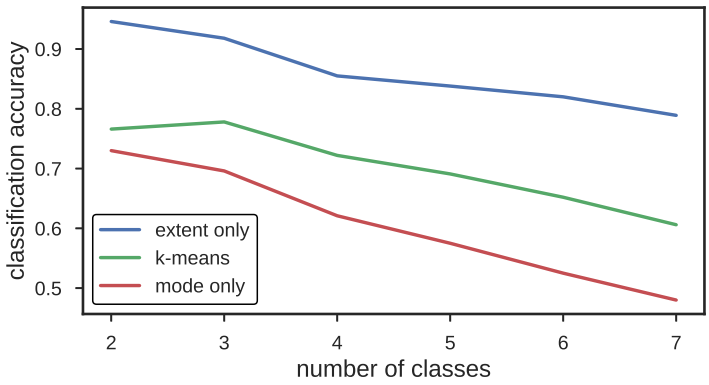

Fig. 4.8.: The average classification accuracy for increasing number of possible labels. Division by the extent in blue, by mode in red and through k-means clustering in green.

4.5 Impact of Surface Types

In a next step the performance of the classification method was examined for different kinds of surface types. Certain scenarios may complicate the classification, as a surface, which is nearly as bright as the clouds, or the inhomogeneity of the surface is imposing on the retrieved texture parameters. This way, the impact of surface albedo and surface texture can be studied and the applicability of the method estimated. The studied scenes are presented in figure 4.9 and situated over the Taklamakan desert in Asia (green), Greenland (orange) and over the South American rain forest (purple). This aspect of the study was performed with the 1km resolution and spectral information of band 17, since no major differences between the resolutions and spectral channels concerning classification were found. The classification was performed using a window size of $120km$ edge length, inter-pixel distance $d = 2$ and a radiometric resolution of 64 grey-levels. In figure 4.10 a typical scene from the individual regions as well as the classification scores into cloud types are presented. For each surface type an individual random forest was trained.

The overall performance is roughly the same between all surface types, but the individual classification differs strongly. The vegetated surface has the darkest albedo and is closest to the ocean case but the classification is the worst of all scenes with a total classification accuracy of 85.3%. Cloud typing above snowy surface is slightly better with a prediction accuracy of 86.6% and the performance is the best

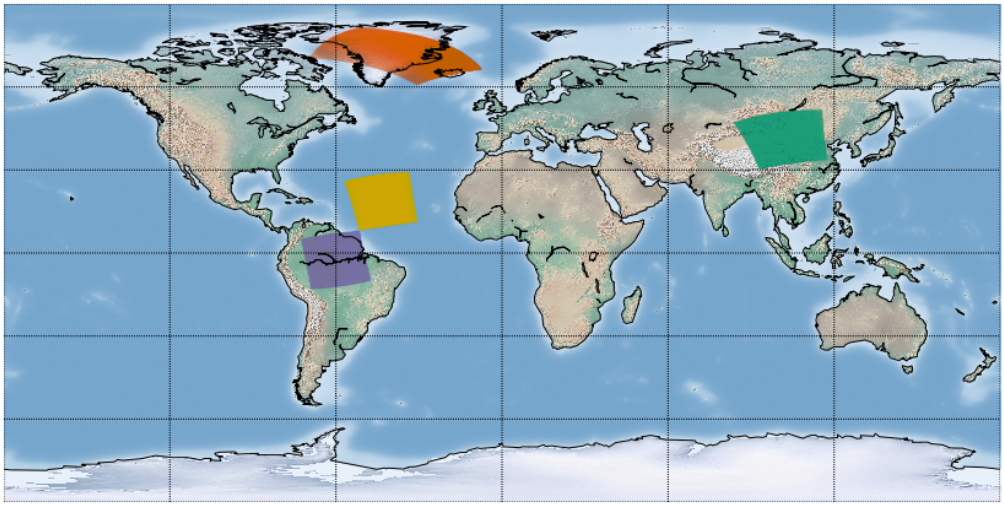

Fig. 4.9.: Arrangement of the studied regions. The studied region of the previous sections is marked in yellow. Scenes above the desert are from the Taklamakan desert in Asia, marked in green, and snowy surfaces are taken from orbits over Greenland (orange). The forest scene is situated over South America (purple).

for the desert case with 88.6%. When looking at the individual classification scores for each cloud type it stands out that the problematic cloud types depend on the surface type. For the Taklamakan desert cumulus clouds are often misclassified as stratocumulus and altostratus and deep convective clouds are mostly interpreted as altostratus. It should be noted that only 188 cumulus pixel (according to CloudSat) were apparent in the data and 35% of those were misclassified. Since the test data set should show similar pixel densities for each type as the training data, one can assume that the amount of cumulus pixel in the training is too small to be representative. The overall prediction accuracy of the rain forest scene is the lowest while the two-dimensional histogram in fig 4.10 does not convey that impression. The classification over south America has no clear worst cloud type and the lowest prediction score is archived for altocumulus with an accuracy of 79.6%, which is the highest minimum out of all surface types. The smaller spread in individual accuracy is accompanied by overall lower classification scores (the highest score is for cirrus clouds with 89.0%, while all other scenes have maximum between $94\% - 95\%$). The lower scores are caused by a misclassification of all cloud types toward deep convective clouds.

In the case over Greenland, for the human observer ass well as satellite remote sensing it can be hard to distinguish cloud from the snow covered ground, since the spectral signature is similar and in thermal infrared the cloud temperature can be

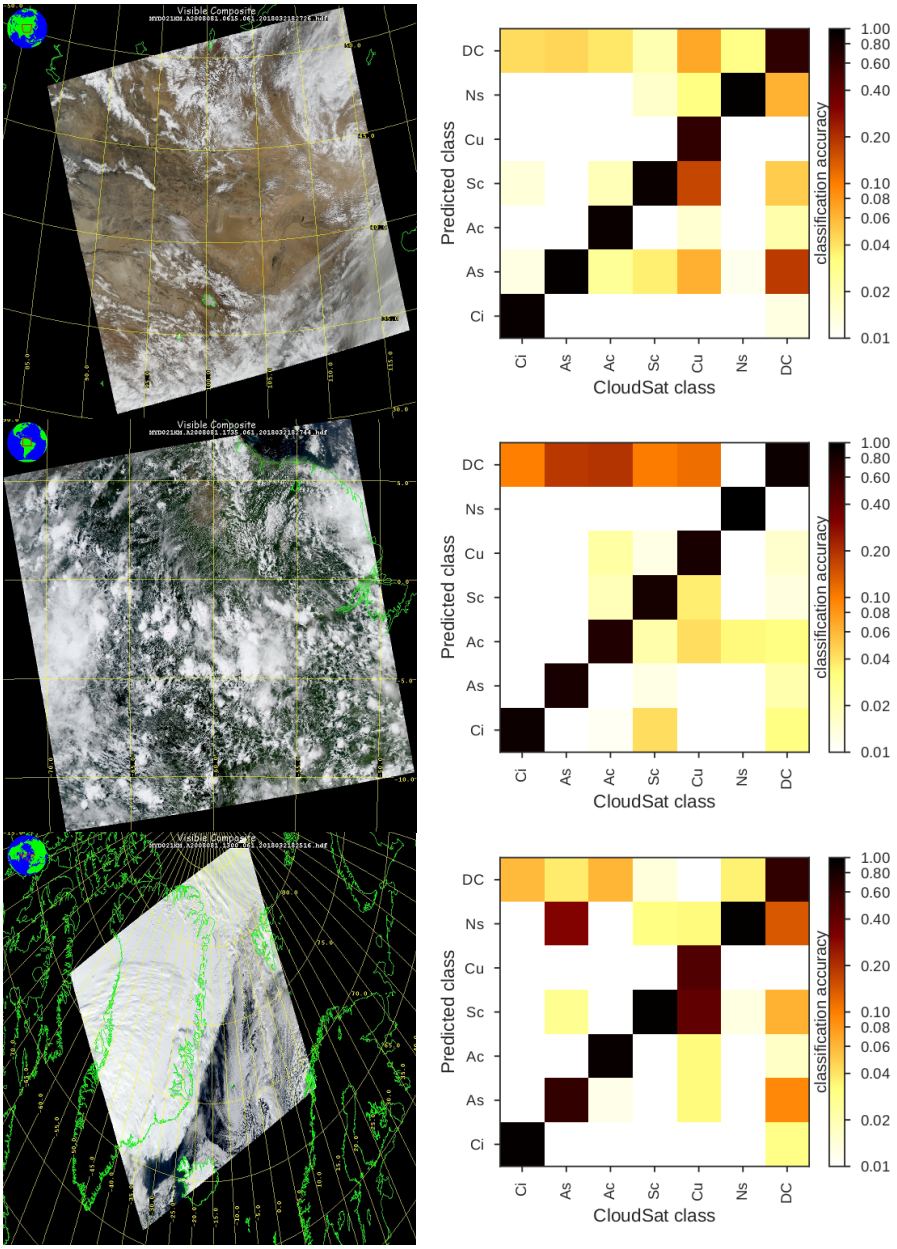

Fig. 4.10.: Right column: RGB image of typical scenes from the studied regions taken from the NASA Level-1 Atmosphere Archive & Distribution System Distributed Active Archive Center at Goddard Space Flight Center (LAADS DAAC `https://ladsweb.modaps.eosdis.nasa.gov/`). Left column: Classification scores of the cloudy pixels into cloud types. From top to bottom: Desert scene over Asia, South American rain forest and the snowy landscape of Greenland.

		C1	C2	C3	total
desert	k-means	0.746	0.598	0.648	0.665
	mode only	0.336	0.762	0.706	0.684
	extent only	0.840	0.854	0.849	**0.848**
forest	k-means	0.746	0.597	0.717	0.694
	mode only	0.361	0.697	0.601	0.597
	extent only	0.819	0.727	0.862	**0.807**
snow	k-means	0.439	0.690	0.833	0.707
	mode only	0.176	0.620	0.733	0.648
	extent only	0.788	0.856	0.706	**0.805**

Tab. 4.3.: Classification accuracy of individual classes and total for k-means clustered and manually clustered data points for the three studied surface types.

close to the surface temperature. Nevertheless, the texture based approach is able to predict the same cloud type as the active instrument in 86.6% of the measurements. Here, altostratus, cumulus and deep convective clouds are the most difficult to identify.

When applying the classification into extents, modes of optical depth and k-means clusters the surface types show similar results to the previously studied water surface. A classification into different groups of vertical extent is by far the most successful with a prediction accuracy between 84.5% (for the desert surface) and 80.5% for the snowy landscape. The two-dimensional histograms can be found in the Appendix figure A.8- A.10.

4.6 Conclusions

The purpose of this study was the development of a preprocessor for cloud parameter retrievals in the O_2 A absorption band to support the determination of cloud top height and cloud optical depth with a priori estimates about the vertical structure of the clouds. We limited the available spectral channels to the visible and near infrared to conform with OLCI's capabilities.
In a first step, we showed that cloud typing into 7 distinct cloud classes based on textural features could reproduce the cloud classification results of CloudSat's 2-B CLDCLASS product to a high degree for scenes over the open ocean. Further, the

impact of variable parameters for the GLCM was studied, finding that the applied window size is by far the most important parameter in this scope. Also, the difference in spatial resolution was considered, only resulting in a variation of classification results, when the radiometric resolution was high enough, i.e. for a maximum number of grey-levels greater than 90. This texture based method has the most difficulties for the classification of cumulus clouds, while all other cloud types are labelled with comparable precision.

Performance of different spectral bands exhibits only minor changes in the classification for MODIS band 1 versus band 17, but the optimal parameter set for band 17 comes with a smaller grey-level co-occurrence matrix by a factor of 4 and smaller window sizes, thus reducing computational effort greatly. This fact should not be neglected, since the GLCM analysis is generally slower than other common methods, like grey-level difference vector and Fourier transform analysis.

Furthermore, we studied the classification of clouds into groups with similar vertical features based on horizontal structures. Three different schemes of clustering the relative vertical extent and the mode of optical thickness into groups were applied. In the process horizontal texture features showed a strong relation towards the relative extent of a cloud while there seems to be a much weaker connection towards the distribution of optical depth inside the cloud. The k-means clustering algorithm, basically giving a mixture of extent and mode clustering, confirmed these findings by displaying good classification results for classes separated by extent values and a worse accuracy for classes with differing modes. Therefore, the prediction of the vertical extent of a cloud based on its horizontal structure is possible, and with a reduced accuracy, the estimation of the distribution of optical depth can also be achieved. Increasing the number of clusters yielded a decreasing performance of classification. For the application the number of groups should depend on the use of the information and requirements for further processing.

Also the impact of different surface types underlying the cloud scene was studied. All scenes above land surfaces show a decreased classification accuracy, whether for cloud typing or classification into defined vertical extents, than in the case above ocean. Suggesting that the dark, nearly non-reflecting water surface is the ideal background for the classification method. The bright surfaces of desert and snow covered ground show cloud typing precision of 88.6% and 86.6% respectively, implying that the impact of a bright but homogeneous surface on the texture parameters impairs the method only by a small degree. One possible explanation is the used spectral region inside the water vapour absorption band. The qualitative comparison of images from spectral band 1 and 17 demonstrated that in band 17 the contrast of cloudy parts in the image is enhanced, which is attributed to the influence of water

vapour absorption at this particular wavelength. Therefore, even if the surface has a similar brightness to the clouds, the texture features should distinctly different. However, each surface type had its own individually trained random forest, specialized in the observed scenario. Applying a generalized classifier for all types will most certainly yield worse results.

The forest case has the lowest total prediction accuracy, suggesting that the homogeneity of the surface albedo can have a stronger impact on the classification than the actual magnitude, but this effect has to be studied in more detail to make a meaningful statement.

The classification into distinct vertical extents is $7\% - 10\%$ worse compared to the water surface, depending on surface type.

Moreover, the influence of solar elevation was not isolated during this study, whereas all available solar zenith angles did enter into the data set. The effect of solar elevation should be similar to a change in viewing angle, in so far that the contrast and the accompanied observed texture may vary with solar zenith angle. A possible way to improve the classification further, is to train the random forest classifiers for certain solar zenith angles only.

5 Intercomparison of Cloud Property Retrievals and Evaluation of an OLCI Prototype Algorithm

For the Sentinel 3 series of ESA satellites the MERIS cloud top height retrieval in the O_2 A band is expanded for the Ocean Land Colour Instrument, including the two additional channels number 14 and 15 alongside the MERIS heritage channels 12 and 13 in the retrieval. Evaluation of the retrieval including the new parametrization for the cloud vertical extinction profile, introduced in chapter 3, is performed. Focus is on the quality of cloud top height, mode and extent values compared to the active instrument Cloud Profiling Radar onboard of CloudSat. As a point of reference a comparable validation study for the MERIS and AATSR *ctp* product, based on the algorithm FAME-C, is presented.

5.1 Cloud Top Pressure Retrieval

The retrieval of cloud top heights by satellite remote sensing is an active field in the earth observation sciences. Besides the actively sensed cloud top by radar and lidar, several passive cloud top height retrievals are common, which are based on different spectral and spatial information. The measurement of the thermal emission from clouds inside an atmospheric window can be compared to the clear sky thermal emission, yielding, converted through vertical atmospheric temperature profiles, a cloud top height. Similarly, the CO_2 absorption band around $14\mu m$ can be used to infer the cloud top temperature/pressure/height with the so called CO_2 slicing method (Menzel et al., 1983), (Wylie and Menzel, 1999). The techniques, based on thermal infrared radiation, work well for high clouds but suffer from a decrease in sensitivity for the lower atmospheric regions. Further, with Raman-scattering techniques (Joiner et al., 2004) and stereoscopic (Ilanthiryan et al., 1992)

measurements it is also possible to retrieve information about the cloud top height. More recently, polarimetric methods (Knibbe et al., 2000) (Buriez et al., 1997) and the O_2-O_2 absorption technique (Acarreta et al., 2004) have proven to be capable to retrieve cloud top heights from remote sensing data. These numerous techniques differ in their sensitivities as well as spatial and temporal coverage leading to different strengths and weaknesses. Through evaluation and intercomparison of cloud data products new insights can be gained.

The O_2 A band method is known since the 1960s (Yamamoto and Wark, 1961) and was since then theoretically studied by various authors: Wu (1985), Fischer and Grassl (1991), Fischer et al. (1991), O'Brien and Mitchell (1992) and Kuze and Chance (1994). The first operational cloud top height products with the O_2 A band method were based on Global Ozone Monitoring Experiment (GOME) (Burrows et al., 1999) and POLarization and Directionality of the Earth's Reflectances (POLDER) (Buriez et al., 1997) measurements. For the Medium Resolution Imaging Spectrometer (MERIS) the Insitute for Space Sciences at the Freie Universität Berlin developed a cloud top height retrieval making use of MERIS' O_2 A Band channel (Preusker et al., 2010). The retrieval was further advanced by Carbajal Henken et al. (2014) towards a synergistic cloud property retrieval, using MERIS and the Advanced Along-Track Scanning Radiometer (AATSR), called FAME-C (Freie Universität Berlin AATSR MERIS Cloud). Here, in a first step a Bayesian cloud detection scheme based on several AATSR and MERIS channels is applied (Hollstein et al., 2015). Next, AATSR's near-infrared and visible channels are used to retrieve cloud phase, cloud optical thickness, and effective radius. In a third step the micro physical and optical cloud properties are input for two subsequent retrievals were the cloud top height is computed for MERIS and AATSR separately. Underlying the retrieval is an optimal estimation with pre-computed look up tables from radiative transfer simulations with MOMO.

5.2 Validation of FAME-C

Validation of the FAME-C algorithm was performed on a Level 2 product basis, as part of the project Cloud CCI by ESA, where close to 10 years of processed ENVISAT data is part of the produced climate data record. As a reference data set the combined product of CloudSat and CALIPSO 2B-GEOPROF-LIDAR was chosen. The 2B-GEOPROF-LIDAR provides the number of cloud layers, the vertical resolved cloud fraction as well as the top and base height of each cloud layer. Additionally,

the 2B-TAU product of CloudSat is utilized for the detection of unsuited co-locations, based on the optical depth of individual cloud layers. On one hand, does the O_2 A band method have difficulties when retrieving the cloud top pressure of multi-layer clouds for dual-layer with $\tau > 2$ (Preusker and Lindstrot, 2009) for the upper layer. On the other hand, surpasses the sensitivity to hydrometeors of both active sensors MERIS' capabilities. Therefore, multi-layer clouds with $\tau_{up} < 2$ as well as single-layer clouds with an optical depth of $\tau < 1$ are excluded from the comparison. The validation study relies on the years 2006-2009, including 326 cross-sections between ENVISAT and the A-train were the co-location fulfills additional conditions besides the cloud filtering:

- spatially, the nearest neighbour for each MERIS pixel is chosen under the condition that the distance between measurements has to be less than $300\ m$

- temporally, the maximum offset between both satellite orbits at the point of cross-section can not be more than 3 minutes to ensure that the cloud scene has not changed significantly. If during a cross-section the limit for the time difference is exceeded the valid part of the orbit still enters the validation study.

- highly reflecting and cold surfaces, such as sea ice and snow covered ground are a known source of uncertainty for the FAME-C retrieval, for AATSR as well as MERIS. Unfortunately, the orbits of ENVISAT and the A-train limits cross-sections to the polar region around $70°$ latitude. Therefore, above average amounts of snow and ice covered surface would enter the comparison, leading to a systematic bias for the validation. In order to avoid this problem, only bare ground and water surface are included. Criterium for the surface cover is the sea-ice and snow cover flag of FAME-C, which is derived from the atmospheric reanalysis data ERA-interim.

The methods for AATSR and MERIS retrieve different physical properties of the cloud. AATSR yields a cloud top temperature, while MERIS measurements result in a cloud top pressure. For easier comparison, ERA-Interim data by the European Centre for Medium-Range Weather Forecasts (ECMWF) is used in order to convert both measurements into heights based on the vertical atmospheric profiles of pressure and temperature at the respective position and point in time.

5.2.1 Validation of Cloud Fraction

Validation of the cloud detection algorithm in FAME-C is performed against the vertical resolved cloud fraction (cf) from the combined radar-lidar product 2B-GEOPROF-LIDAR. Therefore, the highest cloud fraction along the column was compared to the FAME-C cloud area fraction. As metrics, the probability of detection (*POD*) as well as the false alarm rate (*FAR*) and the Hanssen-Kuiper skill score (*KSS*) are applied, which are calculated as:

$$POD_{+/-} = \frac{n_{(++)/(--)}}{n_{(++)/(--)} + n_{(+-)/(-+)}}$$

$$FAR_{+/-} = \frac{n_{(+-)/(-+)}}{n_{(++)/(--)} + n_{(+-)/(-+)}}$$

$$KSS = \frac{n_{(++)} * n_{(--)} - n_{(+-)} * n_{(-+)}}{(n_{(++)} + n_{(+-)}) * (n_{(--)} + n_{(-+)})}$$

with n being the frequency of occurrence for an event and the indices denoting if the measurement of FAME-C and CloudSat/CALIPSO are either positive or negative, i.e. the number of measurements, where both products mark a measurement as cloudy is given by the hits $n_{(++)}$ and clear by correct negatives $n_{(--)}$. The frequency of disagreement is given by false alarms $n_{(+-)}$ and misses $n_{(-+)}$. The Hanssen-Kuipers skill score accounts for the random chance of a prediction being right and can take values between -1 and 1, whereby 0 represents no skill. A value of 1 shows absolute agreement between reference and prediction and has a POD of 1, while -1 means no agreement coupled with a FAR of 1.
FAME-C as well as CloudSat provide their cloud fractions as a real number between 0 and 1, that is converted into a discrete state of cloudy and clear with the arbitrary breakpoint at cf=0.5. The results are summarized in figure 5.1 in form of a 2-dimensional histogram. The agreement between both sets of measurement for the cloudy instance is good. In approximately 90% of the cloud flagged measurements of FAME-C CloudSat also detected a cloud. However, for clear labelled measurements of FAME-C's cloud detection, the CloudSat cloud detection agrees in approximately 60%, while in the remaining 40% a cloud was detected by CloudSat. The internal comparison of Cloud CCI data records found similar results for FAME-C. In the Product Validation and Intercomparison Report (PVIR)(Stapelberg et al., 2018) of the Cloud CCI project FAME-C has shown the least amount of clouds in the tropics

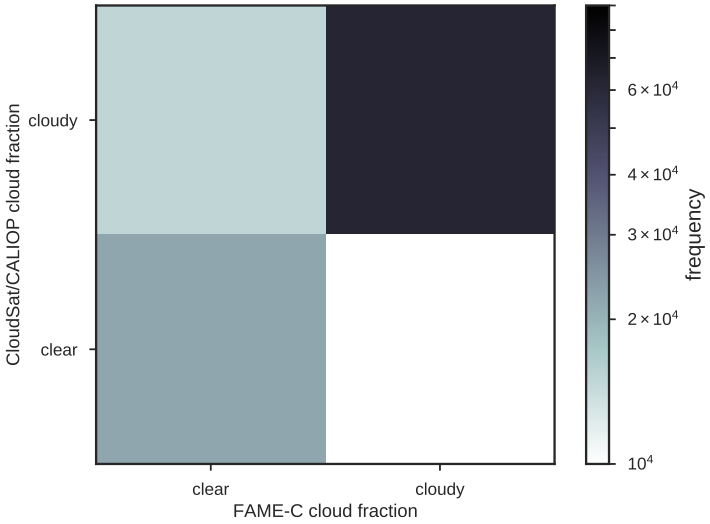

Fig. 5.1.: 2D-histogram of CloudSat/CALIOP cloud fraction compared to FAME-C. The continuous cloud fractions was discretized into $clear \leq 0.5 < cloudy$.

	POD	FAR	KSS
cloudy	0.90	0.10	0.57
clear	0.59	0.41	

Tab. 5.1.: Probability of detection, false alarm rate and Hanssen-Kuipers skill score for FAME-C cloud fraction related to the CloudSat/CALIOP measured cloud fraction.

and at the poles, regarding all participating cloud products.
Combining the PODs and FARs of FAME-C yields a Hanssen-Kuipers skill score of *KSS*=0.57, which shows a moderate agreement between products. The *KSS* as well as the *POD* and *FAR* are summarized in table 5.1.

5.2.2 Validation of Cloud Top Height

Because of the applied restrictions, a total of 17732 co-located measurement for the AATSR cloud top heights and 7649 for MERIS cloud top heights are found. The number of MERIS measurements is lower, caused by less converged retrievals in this region, which could be an effect of low solar elevations, where the O_2 A band method is affected by poor lighting conditions. In figure 5.2 the comparison between FAME-C MERIS and AATSR *cth* to CloudSat/CALIOP *cth* is presented. As accuracy metric the

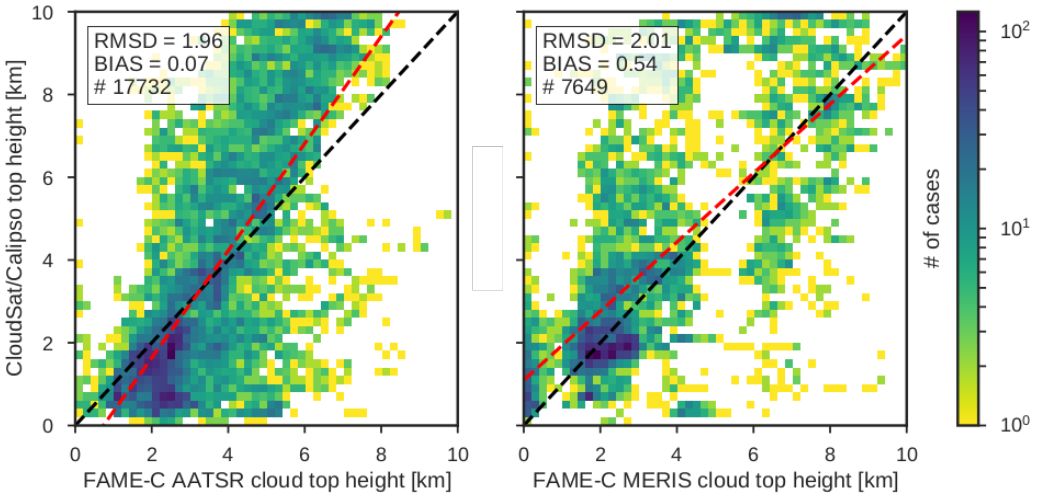

Fig. 5.2.: Comparison of FAME-C *cth* based on AATSR (left) and MERIS (right) measurements with CloudSat/CALIOP combined product 2B-GEOPROF-LIDAR. The measurements have a maximal temporal offset of 3min and optically thin ($\tau < 1$) single-layer clouds as well as multi-layer clouds with an optically thick upper layer ($\tau > 2$) were filtered out. Bias and RMSD are in units of [km].

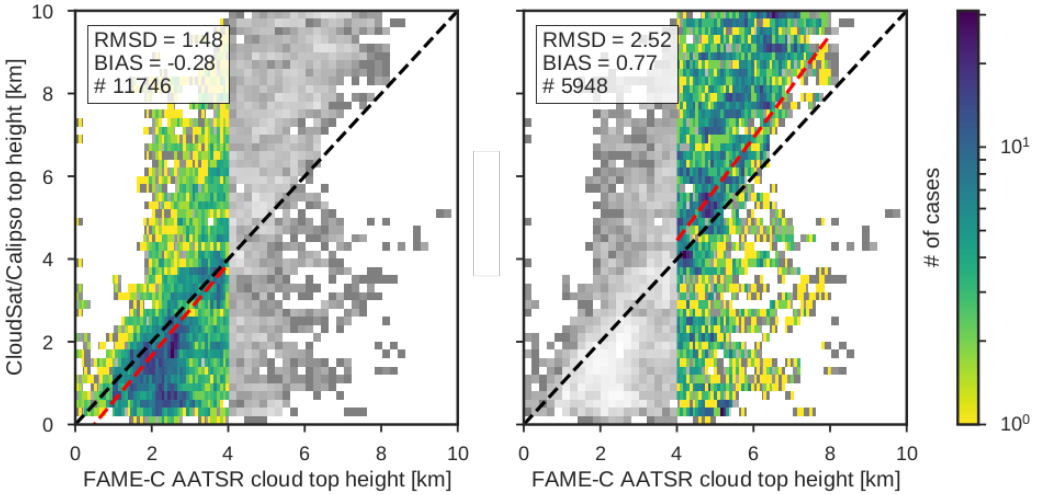

Fig. 5.3.: Comparison of FAME-C *cth* based on AATSR with CloudSat/CALIOP combined product 2B-GEOPROF-LIDAR. Left for clouds with an AATSR retrieved height below 4km and right above 4km. The bias and RMSD calculation is based on the coloured measurements. Bias and RMSD are in units of [km].

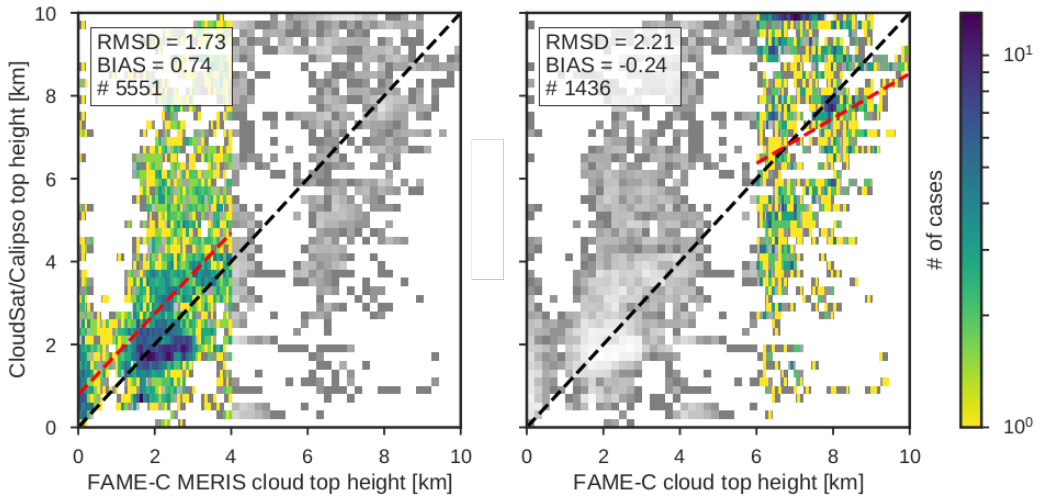

Fig. 5.4.: Similar to 5.3, but for MERIS. Left for clouds with an retrieved height below 4km and right above 6km. The heights between 4km and 6km neglected. Bias and RMSD are in units of [km].

common measure of bias and the bias corrected root-mean-square deviation (RMSD) are employed.

$$BIAS = \frac{\sum_i^n \bar{y}_i - y_i}{n} \tag{5.1}$$

$$RMSD = \frac{\sum_i^n (\bar{y}_i - y_i + bias)^2}{n} \tag{5.2}$$

Here, $\bar{y}$ is the reference data set of CloudSat/CALIPSO and y the FAME-C product, while n is the number of co-located measurements.

The comparison shows, that the bias corrected root-mean-square deviation in cloud top heights between CloudSat and FAME-C AATSR as well as MERIS is around $2\ km$, but the data has next to no bias for AATSR and a bias of $bias = 0.54\ km$ for MERIS. Systematically, FAME-C underestimates cloud top heights with MERIS compared to active sensor, which is expected considering that active sensors can sense optically very thin parts of the clouds. The low bias of the AATSR *cth* is an effect of systematic over estimation of *cth* for low clouds paired with and under estimation for high clouds. Separating the data for low and high clouds reveals information about the actual biases between retrievals. In figure 5.3 the same comparison is presented, but separated at a height of $4\ km$. The considered measurements for bias and RMSD are coloured, the remaining data points are shown in grey. Here, the small negative bias of $-0.28\ km$ for low clouds (left side) becomes visible, which is due to temperature

inversions, which may lead to ambiguous conversion of cloud top temperature to cloud top height. Also, a systematic underestimation of cloud top heights for high clouds (right side) by $0.77\ km$ is apparent, which can be caused by the emission of lower cloud layers in the signal.
The same analysis is shown in figure 5.4 for the FAME-C MERIS *cth* retrieval. In the case of MERIS the underestimation of cloud top heights by $0.54km$ (see fig. 5.2) is caused by an under estimation of *cth* for low clouds between $0\ km$ and $4\ km$ heights by $0.74\ km$ (left side, fig 5.4), while for high clouds (right side, fig 5.4) a small negative bias of $bias = -0.24\ km$ is found. The region of cloud top heights from $4\ km - 6\ km$ is excluded, because few clouds were retrieved by FAME-C MERIS in this region.
Overall, both retrievals perform reasonably well and have a similar RMSD as the MODIS cloud top height products to the CloudSat CPR measurements (Weisz et al., 2007).

5.3 Evaluation of OLCI Cloud Retrieval

As seen in the sensitivity study in chapter 3, the adapted cloud property retrieval for OLCI has the potential for additional information in the state vector. However, the amount of degrees of freedom displays, that more than two independent parameters can only be retrieved for some select cases, i.e. for low optically thick clouds over dark surfaces. In this evaluation the importance of vertical information about the cloud extinction profile for the retrieval algorithm will be analysed by comparing OLCI measurements to CloudSat CPR data. The previously employed combined radar-lidar product was not continued after a battery anomaly in 2011, where CloudSat lost formation with the A-Train for some time and is therefore not available for the OLCI measurement period. Instead, only CPR measurements are used in the form of the 2B-GEOPROF product. Suitable cross-sections with the A-Train are even less frequent for OLCI than for MERIS. Combining less frequent satisfactory cross-sections and additionally a shorter overlap in measurement period for OLCI and the CPR (3 1/2 year for MERIS and the CPR, while OLCI and the CPR provided measurements for the same period for 1 1/2 years) makes a pure statistical assessment of OLCI retrieved cloud properties unfavourable. Therefore, this study will evaluate the OLCI algorithm in a case study. The investigated cross-section happened on the 12th of

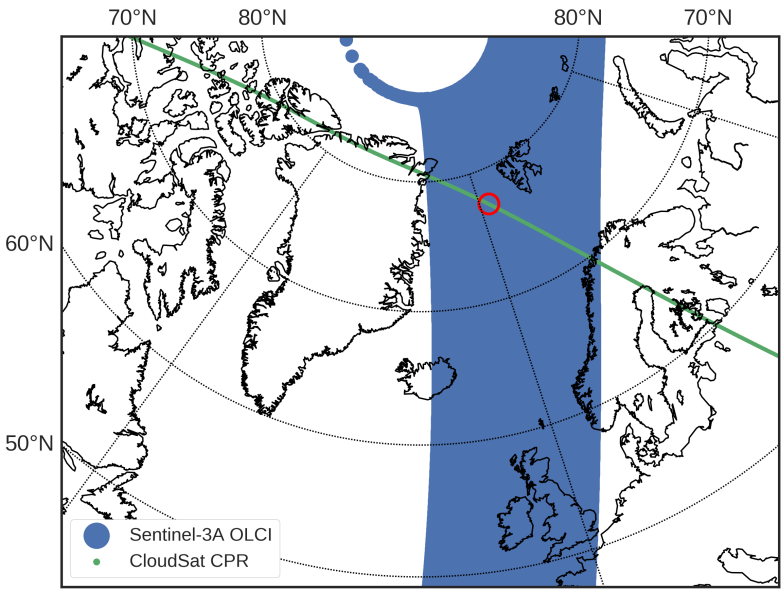

Fig. 5.5.: Case study area for Sentinel-3A OLCI (blue) and CloudSat CPR (green) cross-section on 11/06/2016. Main focus of this assessment study is on the region between latitudes of 77° and 77.4° (red circle).

June 2016 in the northern hemisphere between the coasts of Norway and Greenland (see figure 5.5).

5.3.1 Qualitative Analysis of OLCI Cloud Properties

The mean temporal offset between both overpasses is 2min. 27sec. and this part of the study will focus on the region of the cross-section between latitudes of 77° and 77.5°, highlighted with the red circle in figure 5.5. In this region the a high cloud fraction with an average optical depth could be found, which is ideal for a first study of the retrieval.

The considered CPR measurement, presented in figure 5.6, is the layer optical depth. Cloud top height as well as cloud bottom height as a substitute for the vertical extent are defined as the first and last layer of a single-layer cloud with an optical depth $\tau \geq 0.1$. For the position of the mode, the layer optical depth is approximated with a beta function to be consistent with the radiative transfer simulations, where the mode is then given by equation 3.2. The comparison between CloudSat and

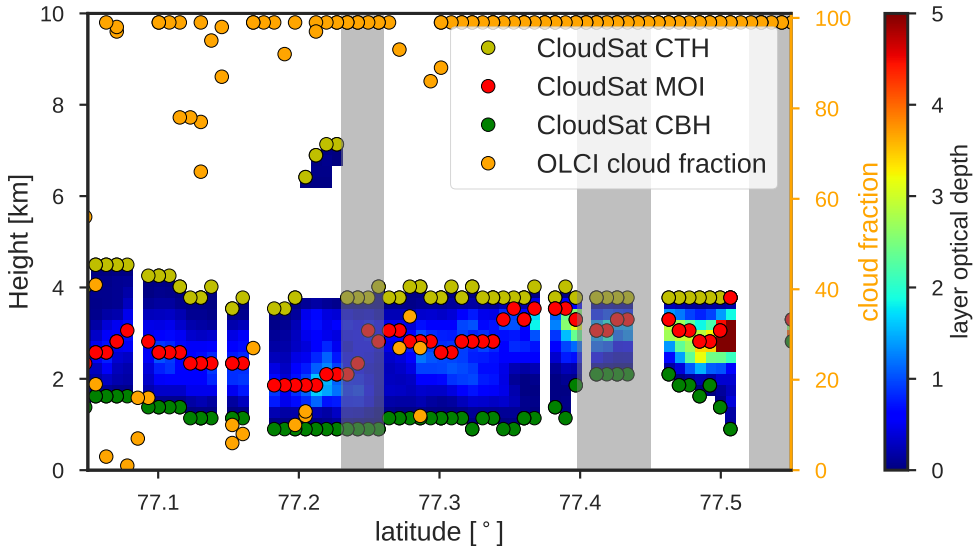

Fig. 5.6.: CloudSat CPR layer optical depth measurement for the studied case between latitudes of 77° and 77.45°. Height (yellow), bottom (green) and mode (red) are overlayed. Orange dots mark the OLCI cloud fraction for the scene according to the right axis. The grey sectors mark areas, where retrieved the optical depth does not agree according to 5.7.

OLCI data is performed on the basis of absolute positions for extent and mode in the atmosphere. Describing the vertical extinction profile with relative parameters is a convenient way for the radiative transfer simulations and build up of the LUT (absolute values would lead to non rectangular LUT or empty grid points), but carries no physical information without knowledge of the cloud top pressure. A comparison with absolute values reveals more information about the performance of the retrieval concerning the vertical structure of the cloud even when the cloud top pressure differs. Therefore, the extent will be displayed by the cloud bottom height (*cbh*).

As a first step in the evaluation, the cloud optical depth from CloudSat is compared to OLCI's as shown in fig. 5.7. On one hand, the optical depth retrieval from an atmospheric window channel is quite reliable and should be consistent with CloudSat. Therefore, deviations for the optical depth can be an indicator for an error in the retrieval or a significant change in the observed clouds, which as consequence could mean that the time between satellite overpasses is too high. On the other hand, when the OLCI retrieved (green dashed line) cloud optical depth for a measurement is high, while the total optical depth for CloudSat does not show the same trend the difference can be an indicator for a saturation of the CPR signal. The CPR has a high sensitivity to optically thin clouds compared to passive imagers, but also

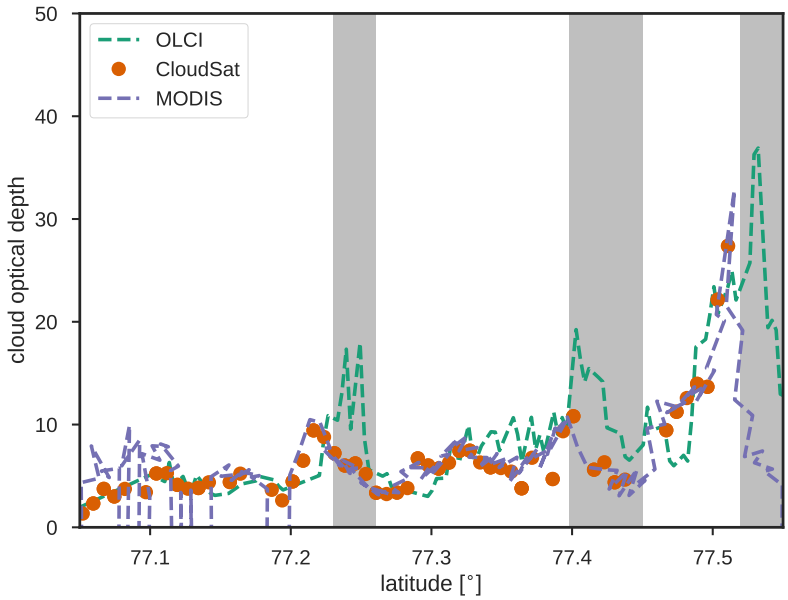

Fig. 5.7.: CloudSat (orange circles), MODIS (purple dashed line) and OLCI (green dashed line) cloud optical depth as retrieved for the studied scene between latitudes of 77° and 77.5°. Grey areas mark a significant difference in *COD* between OLCI and A-train measurements.

has problems with retrieving the lower layers of clouds when the cloud optical depth is too high. In order to separate both cases, MODIS cloud optical depth (purple dashed line) was included in the comparison and measurements, where $\tau_{MODIS} \approx \tau_{OLCI} \gg \tau_{CloudSat}$ are only compared in cloud top height. There is a good agreement between OLCI and CloudSat/MODIS cloud optical depth for most of the scene, except for highlighted areas in grey, where the OLCI retrieval yields higher values for the cloud optical depth. For each highlighted area the MODIS and CloudSat *cod* displays similar features shifted to southern latitudes, giving the impression of being caused by temporal and/or spatial offset between OLCI and the A-train. Considering figure 5.6, the first difference around 77.25° is likely caused by the thin cirrus cloud, which moved to slightly higher latitudes between the CloudSat and OLCI overpasses. Similarly, the second and third area, in which a noticeable difference can be found, corresponds to the region with broken cloud fields in the CloudSat data. However, the OLCI cloud detection did yield a cloud fraction of 100% for those regions, implying that the spatial distribution of the cloud is different in both measurements. When using MODIS pixel, which are positioned $3km$ more westwards, both *COD* measurements agree better, further supporting the assumption

	$ctp \pm \sigma_{ctp}$	$cod \pm \sigma_{cod}$	$ext \pm \sigma_{ext}$	$moi \pm \sigma_{moi}$
1	(CldSat±100) hPa	10±100	0.5±0.5	0.5±0.5
2	(500±500) hPa	10±100	0.5±0.5	0.5±0.5
3	(500±500) hPa	10±100	0.5±0.1	0.5±0.1

Tab. 5.2.: A priori state and error co-variance for the three different cloud top retrievals based on OLCI measurements.

of a minor offset between cross-sections (see appendix, figure A.7). In the following qualitative analysis, even areas with diverging *cod* were included, because they can yield information if one keeps in mind that the prior state vector as well as the assumption of a single-layer cloud may be incorrect.

The cloud parameter retrieval for OLCI was performed with three different initiation conditions in the form of a priori state and a priori error co-variance matrix (details in table 5.2). In the first case the OLCI retrieval was forced to yield *ctp* in a range of 100hPa around the CloudSat *ctp* (yellow dots in figure 5.6), in order to study the derivation of cloud vertical extinction profiles, when the cloud top height is known prior to the retrieval. The retrieved cloud properties can be seen in fig. 5.8 in the top most panel. The number of converged retrievals is generally lower for the first case compared to the others, which indicates that the measured radiance of OLCI has no match in the LUT at those exact cloud top heights. The detailed range in normalized radiance compared to the actual measurements are presented in the section 5.3.2. However, the retrieval tends to place the cloud top height as low as possible, within the allowed margin of $100hPa$ for optically thin clouds. Also, in the optically thin regime, cloud bottom height fits the CloudSat measurement well, but the maximum of optical depth is placed to low. In the northern part of the scene, where the clouds optical depth is larger, the *moi* well as the *cth* agree well with CloudSat, but a higher cloud bottom is retrieved. The impact of the cirrus cloud, marked by the left grey zone, is clearly visible by a small increase in all three parameters, due to a retrieval of a mixture of both clouds. The same scene with different prior assumptions yields figure 5.8(case 2). Here, all 4 parameters were unrestricted due to a large variance as presented in the second row of tab. 5.2. Now, the cloud top pressure is clearly underestimated, while the mode is placed in a similar position to the first case. The extent is found to be $0.3 \leq ext \leq 0.5$, whereby the lower values appear for optically thicker clouds, which leads to a higher cloud bottom height as the CloudSat measurements would suggest. Furthermore, in the right grey zone a retrieval of cloud properties was successful yielding cloud properties consistent with the neighbouring soundings.

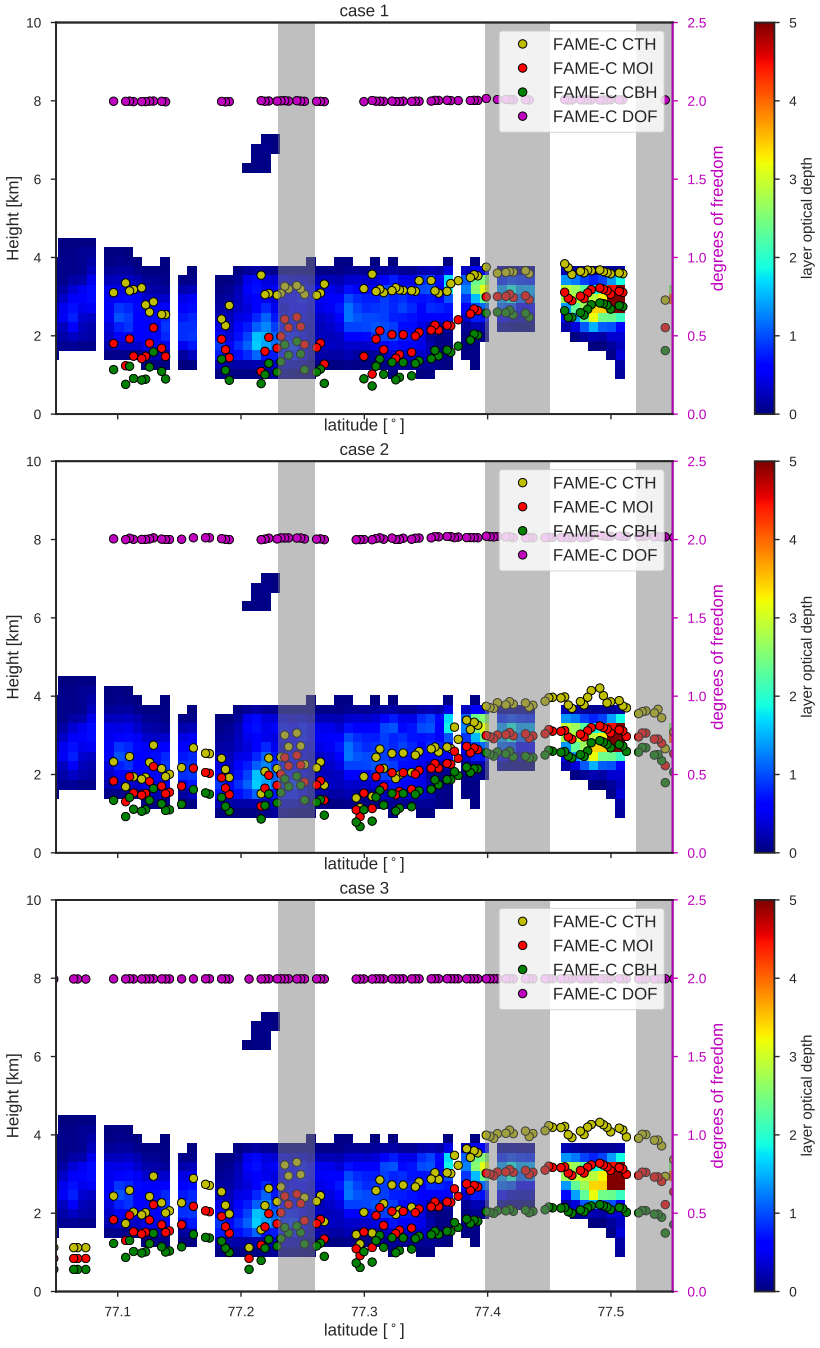

Fig. 5.8.: CloudSat CPR layer optical depth measurement for the studied case between latitudes of 77° and 77.5°. Cloud top height (yellow), bottom (green) and mode (red) of the OLCI cloud property retrieval are overlayed. The degrees of freedom for each successful measurement is shown in purple. Top, middle and lower panel represent different initialization conditions for the retrieval (see tab. 5.2).

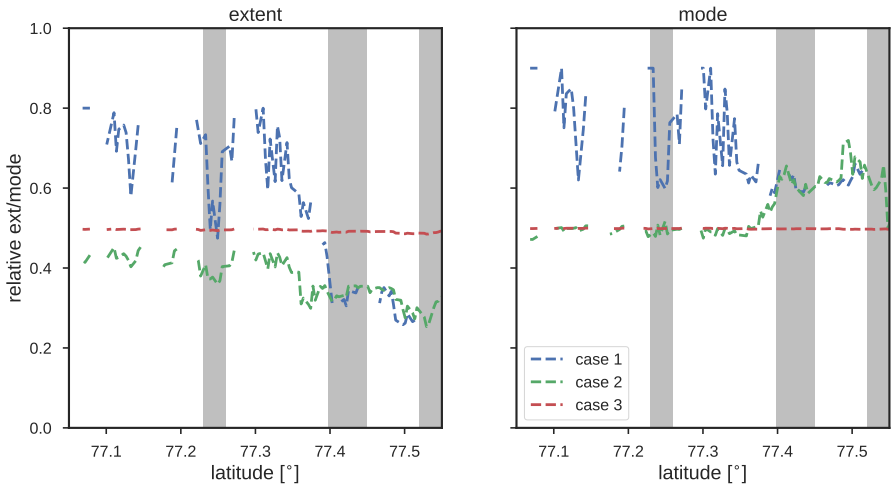

Fig. 5.9.: Relative values for the retrieved extent (left) and mode (right). The blue line (1) is the CloudSat-like measurement, red (2) is for no restrictions on the state vector and green is calculated with no variation in mode and extent. Gaps in the data are caused by non-convergence of the optimal estimation algorithm.

In the last studied case of fig. 5.8(case 3) the mode and extent were fixed to a value of *ext*=*moi*=0.5, simulating a retrieval similar to FAME-C for MERIS with *ctp* and *cod* as primary variables. This particular value was a choice based on the *ctp* results of the second case, to force the retrieval towards higher cloud top heights. The resulting *ctp* are slightly larger in the optical thin part, compared to the second case, and even higher for the optically thicker part. The bottom height demonstrates a better agreement with CloudSat, while the mode is almost the same. Interestingly, in the middle grey zone, cloud optical depth from OLCI deviates by up to $+100\%$ towards the reference, but the agreement in the other cloud properties is the best for the considered sector in all three retrieval runs.

The degrees of freedom for all three cases are nearly constant at $d_s = 2$, i.e. two independent parameters can be retrieved, whereby one degree of freedom is needed for the retrieval of cloud optical depth leaving one for a combination of *ctp*, *ext* and *moi*. A consequence of the under determined retrieval is, that the optimal estimation approach settles at or near the a priori state. During the iteration to find the optimal state vector, the step direction is given by the largest gradient in the look up table scaled with the error co-variance matrix (see equation 2.21). As shown in chapter 3, the highest gradient is often along the dimension of cloud top pressure, which is then the direction of preference for the optimal estimation to find a suitable state. Coupled with the amplified ambiguity caused by the additional parameters, the possibility of accomplishing the convergence criterium without the need to vary

extent and mode is increased, which is why the algorithm retrieves a state more often around the a priori values of *ext* and *moi*. This becomes clearer, when comparing the dynamic range of extent and mode for the three studied OLCI retrieval runs. The relative values of mode and extent for all retrieval runs are presented in fig. 5.9. Here, gaps in the graphs are caused by non converged retrievals as well as cloud free measurements. Case 3, where mode and extent should be constant behaves as intended and shows only minor adjustments in both values. However, when appointing a cloud top height (case 1, blue line) to the retrieval, mode and extent are varied considerably between values of 0.35 and 0.8 for the extent and 0.5 and 0.9 for the mode. Contrary, without constraints, both parameters associated with the vertical extinction profile show smaller variations over the scene. Here, the extent varies between 0.25 and 0.45, while the mode takes values between 0.49 and 0.76. It is noticeable, that in case 2 both parameters show low variations for the part of the scene with optically thin clouds (south of $77.4°$), which increases with the optical depth. In order to obtain cloud vertical extinction profiles through passive remote sensing the amount of information entering the retrieval has to be increased, either by including additional radiation measurements from different spectral regions, e.g. infrared radiation, as used for cloud top temperature retrievals, is a likely candidate due to its different absorption behaviour in water clouds or by appointing cloud top pressure and cloud optical depth beforehand as prior knowledge from an independent instruments' cloud retrieval based on a different technique. For OLCI SLSTR would be a likely candidate.

5.3.2 Points of Non-Convergence

In the following the measurements of figure 5.8 (top panel), where no convergence is achieved will be studied in more detail. As mentioned before, the fact that the retrieval did not converge indicates, that the associated combination of radiances from channels 12-15, for these particular viewing geometries, solar elevation and surface characteristics, is absent in the look up table. Therefore, the cloud parameters, with the cloud top height taken from CloudSat measurements and the optical depth from the MODIS retrieval, are used as input in the forward operator, an n-dimensional interpolation in the look up table. In figure 5.10 the studied scene is presented, with converged and not converged measurements as yellow and red circles, respectively. Below, each channel radiance is given by coloured circles representing the measured values, which are normalized by the solar constant, while the blue area marks the possible spread in radiance of the forward model. The spread is achieved by running

the forward model with the brightest and darkest configuration for this particular cloud top height and optical depth, i.e. with *ext*=*moi*=0.1 and *ext*=*moi*=0.9. High values are related to an idealized cloud with next to no geometrical extent, which reduces penetration depth and yields higher TOA radiances as the counterpart with *ext*=*moi*=0.9, where the cloud is spread over the whole remaining atmosphere and the optical depth is concentrated on the bottom. Measurements without convergence outside of the marked grey areas are most likely associated with cloud free atmosphere at the time of OLCI's overpass and will not be further discussed here. The impact of the different forward model runs is visible in channel 13, which has the highest sensitivity towards the cloud parameters, while channel 14 and channel 15 exhibit smaller/no changes in TOA radiance with changing cloud vertical profile. Considering only the red circles in the grey areas, the non-converged measurements can be attributed solely to channel 13, where the measured radiance is lower than simulated. The overestimation of radiance in this case can have several causes. On one hand it can be an artefact caused by the offset between satellite overpasses, leading to forcible retrieval of a wrong cloud top pressure. On the other hand if the applied distribution of optical depth with a beta function is fundamentally wrong for those particular points, no suitable radiance will be found in the look up table. The region with the cirrus cloud is explained by the first scenario, where the offset between measurements forces the retrieval to detect a cloud top height, which does not match the signal, because of outdated CloudSat information. Nevertheless, even without offset the thin cirrus on top of the cloud would be a problem, because *ctp* measurements of multi-layer clouds, without a method to detect those beforehand, is problematic for passive imagery and in this particular retrieval has not been considered in the underlying radiative transfer simulations.
Also, the impact of the optical depth on the spread of the forward model is apparent, insofar as for optically thicker clouds the sensitivity to geometrical extent and distribution of optical depth increases, i.e. for optically thin clouds no impact on the vertical extinction profile can be detected.

5.3.3 Quantitative Evaluation of Cloud Properties

Additionally, the deviations between OLCI and CloudSat measurements was quantified for the complete cross-section as shown in fig 5.11. For the reminder of the comparison co-locations are excluded if either a multi-layer cloud, as indicated by CloudSat, is present or the difference in retrieved cloud optical depth exceeds 10% of τ_{olci} or $\Delta\tau = 1$, whichever is larger. The associated results are summarized in

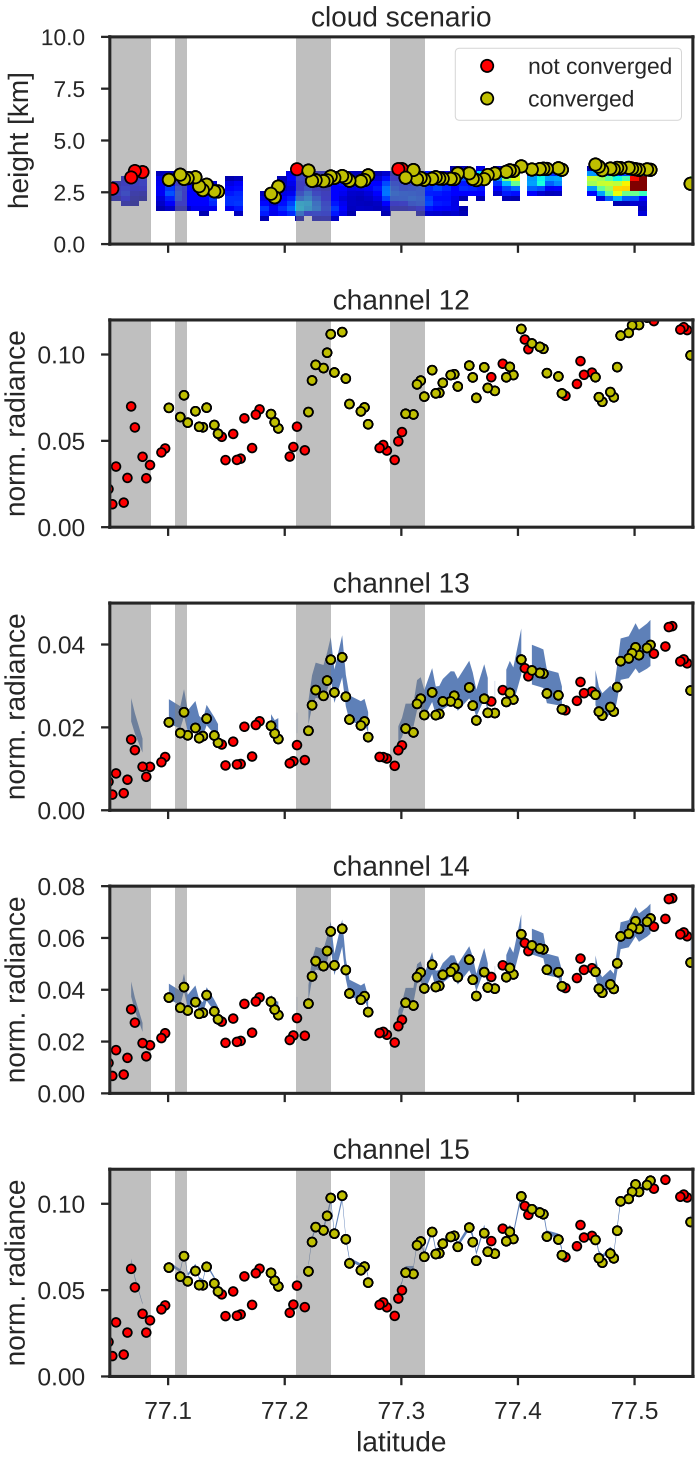

Fig. 5.10.: Studied cloud scene with retrieved cloud top height (first panel). Normalized radiance for the Channels 12 (second panel), 13 (third panel), 14 (fourth panel) and 15 (last panel) of the OLCI retrieval forced to mirror CloudSat cloud top heights. The blue area represents the possible spread in the LUT's by variation of the mode and extent. Converged measurements are presented in yellow, while not converged ones are marked in red. Not converged measurements outside the grey zones correspond to cloud free soundings.

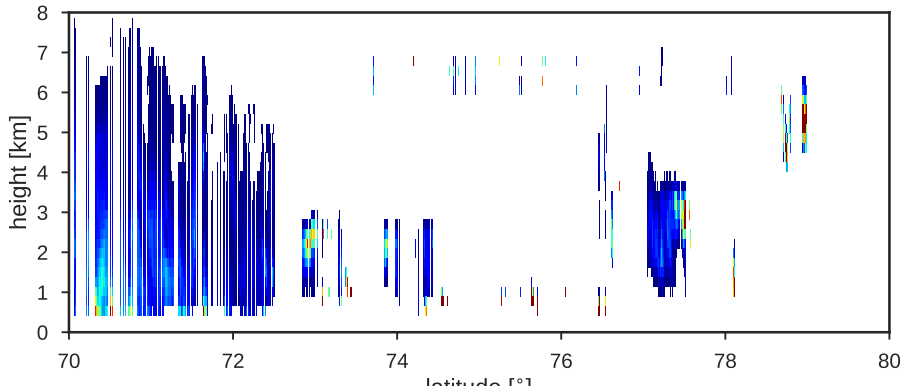

Fig. 5.11.: Layer optical depth of CloudSat for the entire cross-section with OLCI on the 12^{th} of June 2016.

fig. 5.12. The case number refers to tab. 5.2, as for the qualitative analysis. Case 1 naturally shows the best agreement with CloudSat for the cloud top height, since the CloudSat measurement was used in the a priori state. However, cloud bottom height and position of the mode of optical depth also demonstrate the lowest root-mean-square deviation of all cases. However, including the CloudSat cloud top height in the prior state vector leads to the largest bias of all bottom heights and modes. In case 2, the agreement between measurements decreases, especially for cloud top height, where $rmsd = 1.26km$ and $bias = -0.38km$, i.e. without constraints the cloud top height is underestimated for this case. For cloud bottom height and mode position, the mean difference compared to CloudSat is at $1.50km$ and $1.52km$, respectively. In this scenario the extent is systematically overestimated by $0.21km$, while the mode has a small bias of $-0.03km$. In case 3, cloud top height has a similar agreement with a rmsd of $1.27km$, but the top of the cloud is systematically placed $0.32km$ lower in the OLCI retrieval. Extent and mode have the same values in rmsd and bias as in case 2.

Comparing case 2 $\&$ 3 with the FAME-C validation of the MERIS *cth* product, shows a clear improvement in mean difference as well as bias. However, it has to be noted that the underlying number of data points going into each comparison is significantly different. Only clouds with a cloud top between $2km$ and $8km$ were present in the evaluation, and most of them had a cloud bottom height below $2km$. Especially high and optically thin clouds were sparse in this study, which is considered to be one of the more problematic cloud scenarios for the O_2 A band method.

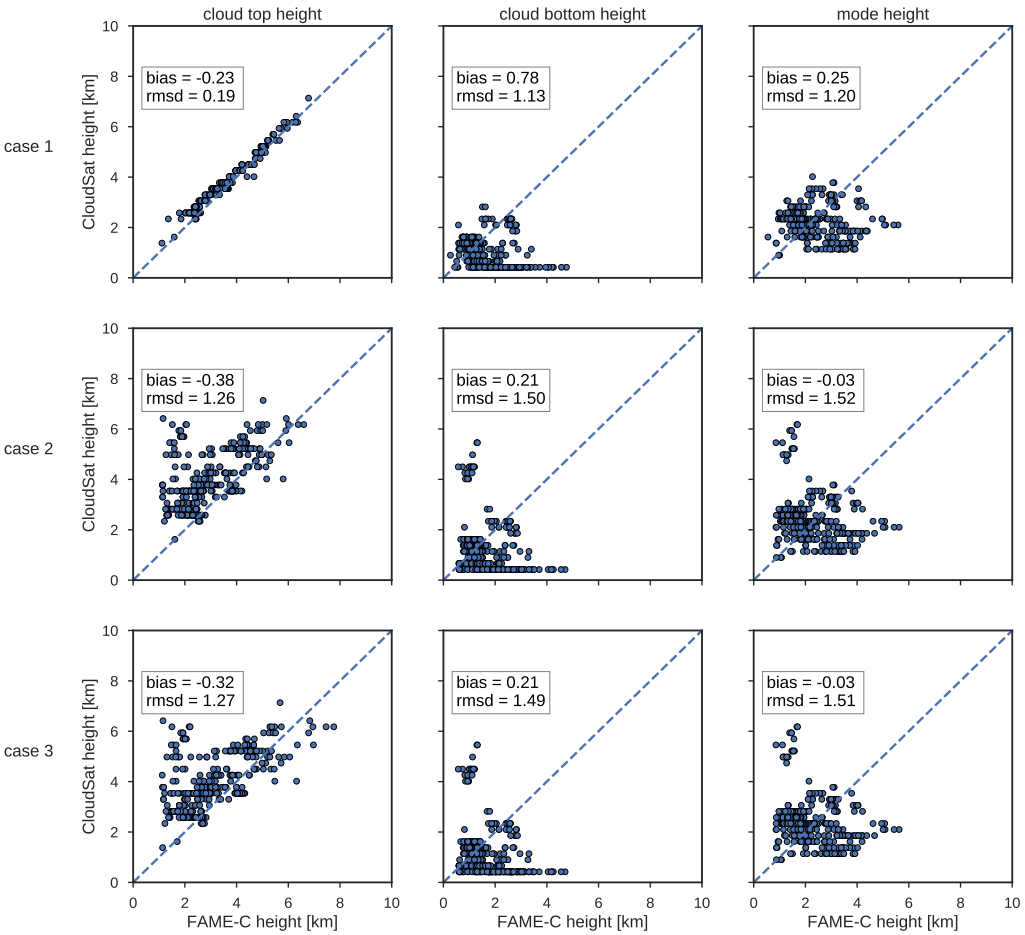

Fig. 5.12.: Comparison of heights for cloud top (left), bottom(middle) and mode(right) between CloudSat and OLCI for three different OLCI retrieval runs.

5.4 Conclusion

In this study the cloud fraction as well as the cloud top height of the FAME-C retrieval by Carbajal Henken et al. (2014) was compared to the CloudSat/CALIOP based 2B-GEOPROF-LIDAR product. Due to the orbital cross-sections of the participating satellites, the study was limited to cross-sections north of $60°$ latitudes with all its problems like low solar elevation and snow/ice. The evaluation of cloud fraction revealed, that FAME-C's cloud detection misses around 40% of the clouds, which are detected by the active instruments, but has a low number of falsely classified clouds. Further, the comparison of cloud top heights for the FAME-C MERIS as well as AATSR revealed a mean difference for both instruments of around $2\ km$, with a small bias of $540m$ for the MERIS based retrieval. Also, when breaking down the comparison into low and high clouds, contrary offsets could be found for each regime. AATSR has shown to overestimate low clouds, while underestimating high clouds and MERIS vice versa.

For a first indication of performance, the evaluation of the adapted cloud top height retrieval for the MERIS successor OLCI against CloudSat only products was carried out. Due to sparse cross-sections between Sentinel-3A and CloudSat the study focused on a single overlap in the North Atlantic ocean. Difference in both measurements could be found, that are attributed to temporal and spatial offset between measurement, which was considered during the interpretation of the results.

Qualitative analysis of the cross-section revealed, that a higher cloud optical depth increases the quality of the retrieved cloud parameters, by decreasing signal contamination by the surface and increasing the sensitivity to cloud properties. Furthermore, cloud top pressure is systematically underestimated, if the retrieval is not forced to yield a comparable cloud top heights to CloudSat. However, if the cloud top height is forced onto a certain value the retrieval of the cloud vertical extinction profile improves. Detailed inspection of the cloud vertical extent and mode during the retrieval showed, that the algorithm tends to be modest when varying these parameters, except when those are the only variables available. Extent and mode of optical depth show a similar mean deviation to the CloudSat measurements as the cloud top height.

Measurements that had no successful convergence in the retrieval were studied by employing the retrievals forward model. It was found, that those data points exhibit smaller top of atmosphere radiances in channel 13 than previously simulated, which can be an indicator of insufficient model for the distribution of optical depth inside the cloud for this particular scene.

Comparing the evaluation results of OLCI to FAME-C an improvement in the mean difference and systematic bias of cloud top height can be noted. Further improvements, like the optimization of the distribution of optical depth, are promising to increase the agreement between OLCI and active instruments. Because of the lack of information content in the measurement, the OLCI retrieval technique may better suited as a vertical profile retrieval with the cloud top height as auxiliary parameter taken from a independent instrument with a different retrieval technique like SLSTR. Otherwise, the amount of information has to be increased by adding radiative measurements in other spectral regions, which is of interest for further studies regarding the O_2 A band technique.

6 Validation of CC4CL Top of Atmosphere Fluxes

The retrieval of radiative fluxes is a field in remote sensing with high requirements towards accuracy. The absolute value of the imbalance in energy flux can be as small as the uncertainties of the retrieval technique, as seen in section 1.1. The radiative flux is defined as the integral over the amount of power, which is radiated through an area. In case of the atmospheric radiative flux two quantities are of interest, the incoming solar flux measured at the top and bottom of atmosphere, yielding the amount of absorbed energy in the atmosphere and the upward directed radiative flux yielding the outgoing energy.
Satellite remote sensing measurements are normally limited to one instrument with a well-defined viewing direction. If the radiance would be independent of the viewing geometry, the radiative flux would be represented by a single measurement from an arbitrary viewing direction. However, atmospheric and surface scattering creates directions of preference, thus rendering the direct measurement of the radiative flux technically impossible. This so called anisotropy of irradiance is the desired quantity, to transform a point measurement into a flux. Different techniques have been developed to retrieve the radiative flux at the top of atmosphere. In this study the TOA short- and longwave flux products of the Cloud CCI project are validated against fluxes derived by the Clouds and the Earth's Radiant Energy System (CERES). The presented results are also part of the "*Validation Report (VAL) - CC4CL TOA FLUX*" for Cloud CCI, at: `http://www.esa-cloud-cci.org/?q=documentation`

6.1 CERES

CERES is a broadband radiometer operated by NASA on-board the polar orbiting science satellites Terra (EOS-AM) & Aqua (EOS-PM). CERES measures the radiation leaving the earth at the top of atmosphere. Its biaxial scan mode provides angular flux information, which is used to determine the outgoing short- and longwave flux on a global scale. CERES measures radiation in three different channels, a shortwave

channel to measure reflected sunlight, a longwave channel to measure Earth-emitted thermal radiation in the 8-12 μm "window" region, and a total channel to measure all wavelengths of radiation. In this study the SSF1deg (single scanner footprint, 1° x 1° resolution) Edition 4 product of CERES Aqua is used, containing diurnally corrected monthly averages of radiative fluxes at the top of atmosphere, as well as the SSF (single scanner footprint) level 2 product for individual scene studies. In the following the short wave and longwave fluxes will be compared to MODIS Aqua based fluxes retrieved with CC4CL.

6.2 CC4CL & BUGSrad

The Community Cloud retrieval for Climate (CC4CL, Sus et al. (2017);McGarragh et al. (2017))is part of the Cloud CCI project for the creation of a Thematic Climate Data Record (TCDR). CC4CL is a community code used to retrieve cloud properties from AVHRR, MODIS and (A)ATSR/SLSTR measurements. The cloud and aerosol properties in CC4CL are derived by the Optimal Retrieval of Aerosol and Cloud (ORAC (Thomas et al., 2009)). Cloud and aerosol retrievals are radiatively consistent inside CC4CL, through the simultaneous retrieval of all properties using all available instrument channels. In a post processing step the cloud and aerosol information is used to run the BUGSrad algorithm (Stephens et al., 2001).
BUGSrad is a radiative transfer model assuming a plane-parallel atmosphere with a two-stream approximation and a correlated-k distribution for atmospheric absorption coefficients. It was initially developed for the use in a community base atmosphere model (CAM) (Collins et al., 2004). BUGSrad uses the information about cloud and aerosols together with auxiliary data containing visible and near infrared surface albedo and surface temperature, vertical profiles of temperature, humidity and ozone and more (for a full list consult the Algorithm theoretical basis document ATBD, Christensen et al. (2016)), to compute the broadband top and bottom of atmosphere radiative flux.

6.3 Point Spread Function

The CERES footprint is defined by the point spread function (PSF), which describes the CERES instruments response to the radiation field. The PSF is defined in angular space, which leads to a constant field of view in angular space of $1.3°$ along-track and

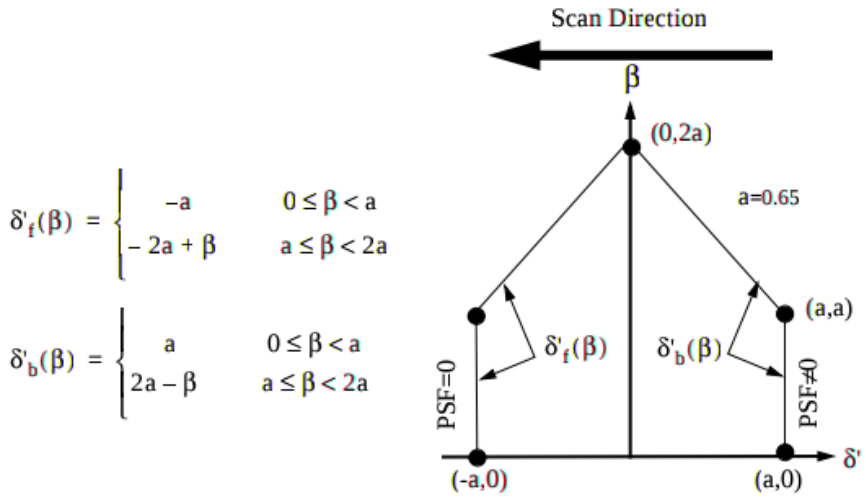

Fig. 6.1.: CERES field of view. δ' is the along-scan angle, β the cross-scan angle and indices f and b denote the forward and backward boundaries. From Green and Wielicki (1997).

$2.6°$ cross-track, which varies in surface area. The CERES footprint has an elliptic form with a size of 32km (along track) and 31km (across track) at nadir for EOS Aqua and Terra, which corresponds to an equivalent area circle with a diameter of 32km (Green and Wielicki, 1997). For a viewing angle of $\theta = 70°$ the footprint already has a size of 328km $\times$ 82km. In order to compare MODIS pixel based TOA fluxes with CERES derived fluxes the PSF has to be considered, during the averaging of the high resolved data.

The field of view is presented in fig 6.1. Here, δ' is the along-scan angle, β the cross-scan angle and indices f and b denote the forward and backward boundaries, respectively. With these definitions for the FOV the PSF can be written as:

$$P(\delta', \beta) = \begin{cases} 0, & \|\beta\| > 2a \\ 0, & \delta' < \delta'_f(\beta) \\ F[\delta' - \delta'_f(\beta)], & \delta'_f(\beta) \leq \delta' \leq \delta'_b(\beta) \\ F[\delta' - \delta'_f(\beta)] - F[\delta' - \delta'_b(\beta)], & otherwise \end{cases} \tag{6.1}$$

with the function F being an exponential polynomial (for further details consult the source material (Green and Wielicki, 1997)). Since CERES and MODIS share the same satellite the along and across scan angles can be easily calculated for each imager pixel, followed by the associated PSF. If an imager pixel is inside a CERES footprint, can be evaluated by testing the PSF against the 95%-energy PSF

of CERES (footprint of the size that 95% of radiative energy is considered). If $P(\delta', \beta)_{imager} \geq P_{95\%}$ an imager pixel is within the CERES footprint and will enter the weighted sum:

$$\bar{x} = \frac{\sum_{i,j} w_{ij} x_{ij}}{\sum_{i,j} w_{ij}}, \tag{6.2}$$

whereby x is the parameter from the imager data, that should be averaged over the CERES footprint and w is the discrete weight given by the PSF. Normally this equation would be an integral over the FOV, but the spatial resolution of an imager creates a discrete field of values to be averaged and the integral can be converted to a sum, where the weight depends on the cross-scan and along-scan angle. The number of discreet weights depends hereby on the spatial resolution of the imager.

6.4 Shortwave and Longwave TOA Annual Means

The comparison of TOA fluxes between CERES and CC4CL was performed on an annual level for the year 2008. The monthly means from the SSF1deg product were averaged and spatially interpolated on a 0.5°x 0.5° grid to accommodate the CC4CL resolution. Also, a diurnal cycle correction was applied to the CC4CL data, which is based on diurnal TOA flux cycles observed with the Geostationary Earth Radiation Budget instrument (GERB), in the form of correction factors to mimic a 24h sampling (from personal correspondence with Martin Stengel). Individual correction factors were applied for either clear sky (not part of this study) or all-sky measurements, separated again into measurements over land and sea. The values for each correction factor are shown in table 6.1. The presented values are only valid for equator crossing times similar to the Aqua satellite at 1:30 p.m: Figure 6.2 shows the shortwave outgoing TOA flux of CERES as well as CC4CL. The left column shows the CC4CL product with diurnal cycle correction, the right one without. Top row is the ESA CCI product derived with CC4CL, in the middle the CERES product and the last row shows the difference between both data sets as Cloud CCI – CERES. When the ESA CCI product is not diurnally cycle corrected, the SW flux estimates are

all-sky	land	sea
shortwave	0.668	0.795
longwave	0.987	0.998

Tab. 6.1.: All-sky correction factor for short- and longwave to account for the diurnal cycle in TOA flux (personal correspondence with Martin Stengel).

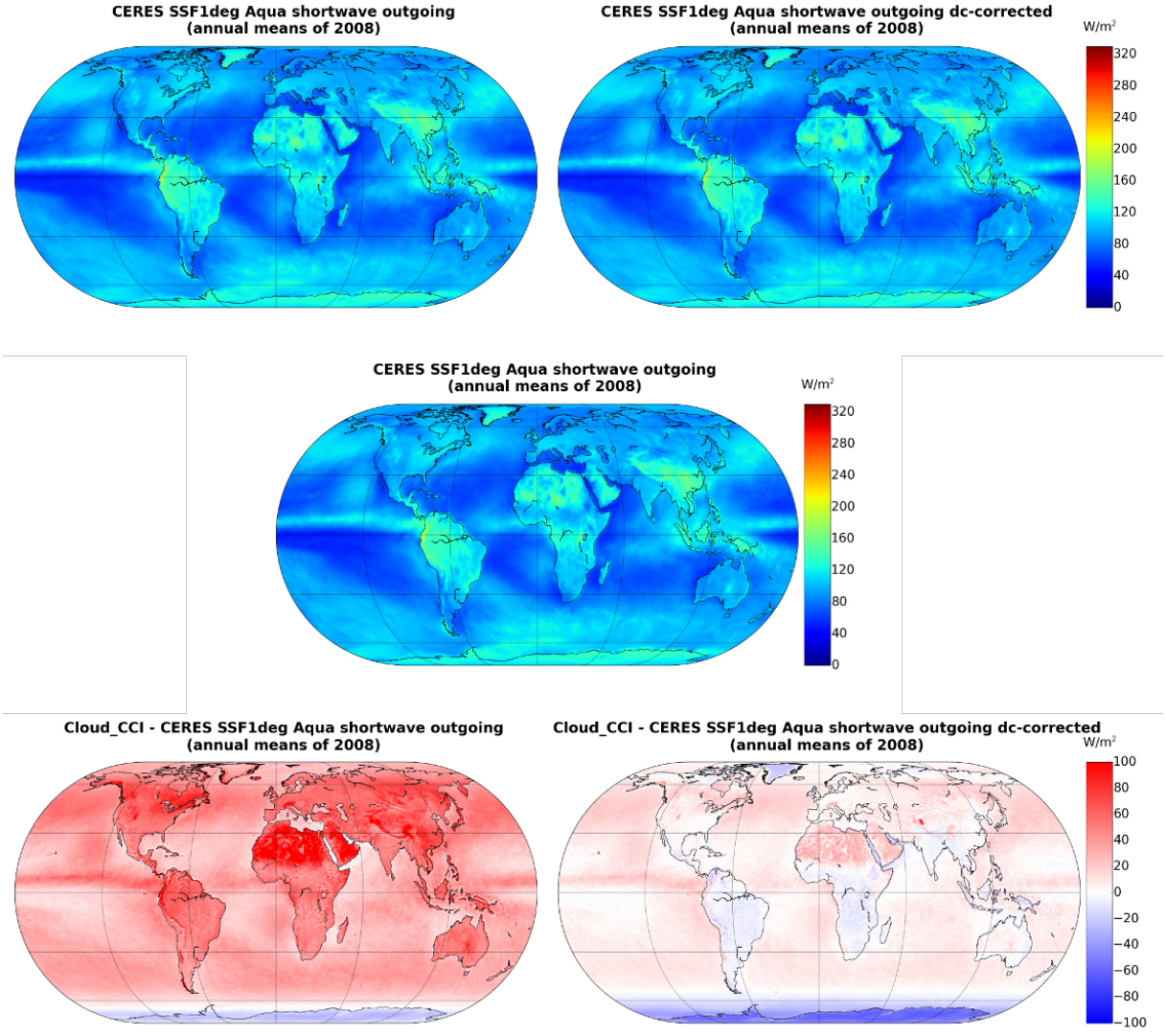

Fig. 6.2.: Shortwave TOA flux comparison for the annual averages of 2008: On the right column are diurnally corrected flux estimates, on the left without correction. From top to bottom are shown the: (1) Cloud CCI MODIS product (2) CERES SSF1deg (3) Cloud CCI MODIS – CERES SSF1deg.

more than $100W/m^2$ higher than the retrieved flux from CERES. An overestimation of the annual shortwave flux is not surprising since the MODIS Aqua measurements take place at 1:30 pm local time, near the maximum of short wave flux during a day and are not representative of an average daily flux. Applying the diurnal cycle correction produces a better agreement between the ESA CCI product and CERES. The difference Cloud CCI – CERES is within mostly within $20W/m^2$ globally, except for a region in central Asia, where the difference in flux still exceeds 100 W/m^2. While the difference between both products is characterized by a positive bias in the northern hemisphere and a small negative bias over land in the southern hemisphere, regions with high temporal snow coverage e.g. Greenland and the Antarctic show a large negative bias. Comparisons between ESA CCI and CERES longwave TOA flux show similar patterns globally (fig. 6.3) and with a difference of up to $25W/m^2$. The diurnal cycle correction as only a small impact on the flux, since the correction factors are close to 1, because the dynamic range of the longwave flux is rather small in comparison to its absolute values. While the uncorrected flux shows positive biases over Africa, South America and the Antarctic, applying the diurnal cycle correction almost removes those features completely. In the longwave regime the ESA CCI product derives smaller TOA fluxes on a global scale as produced by the CERES SSF1deg data set.

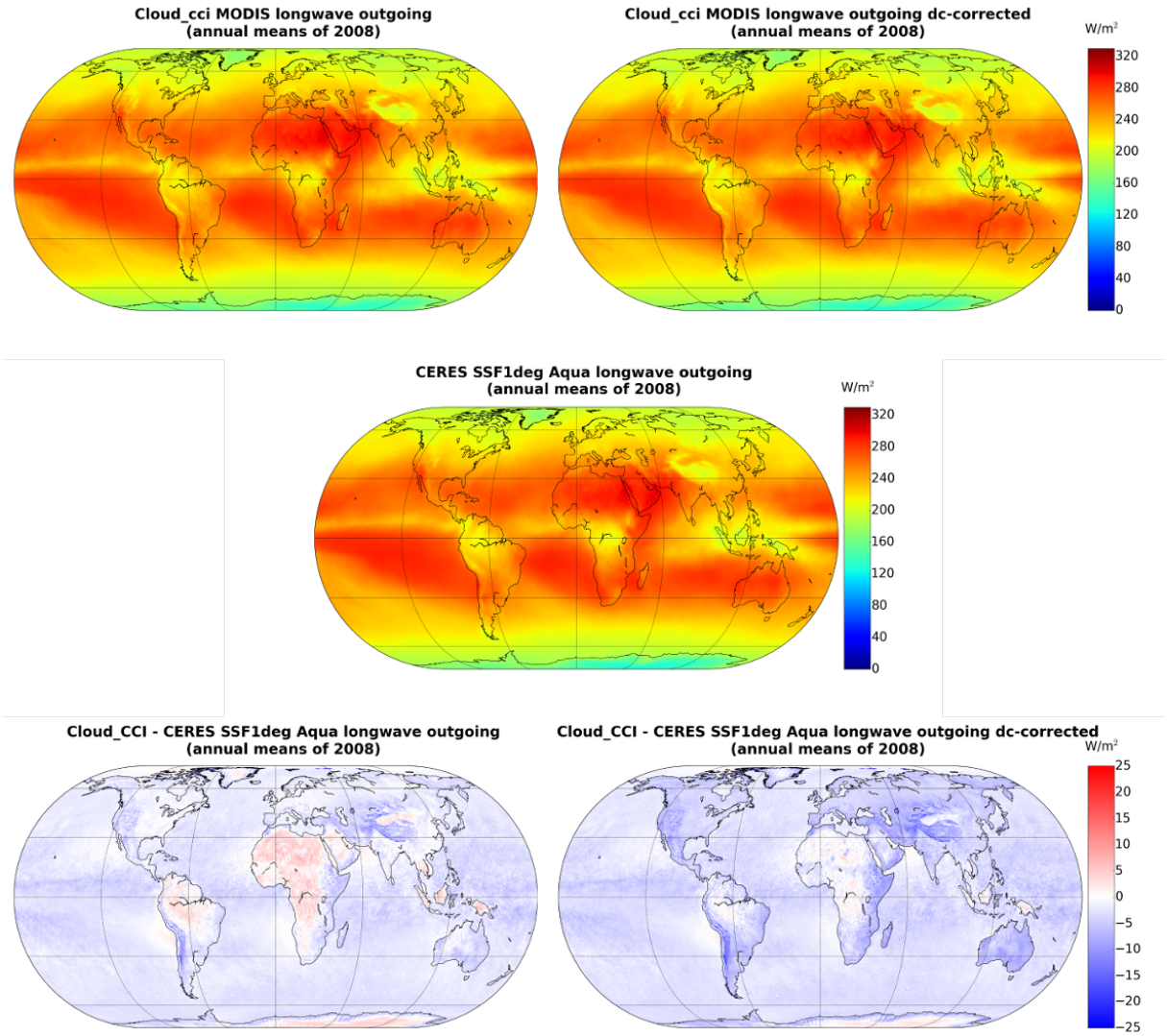

Fig. 6.3.: Longwave TOA flux comparison for the annual averages of 2008: On the right column are diurnally corrected flux estimates, on the left without correction. From top to bottom are shown the: (1) Cloud CCI MODIS product (2) CERES SSF1deg (3) Cloud CCI MODIS – CERES SSF1deg.

#	surface type
1	evergreen needleleaf forest
2	evergreen broadleaf forest
3	deciduous needleleaf forest
4	deciduous broadleaf forest
5	mixed forest
6	mixed shrubland/grassland
7	shrubland
8	wooded tundra
9	savanna
10	grassland
11	wetland
12	cropland and pasture
13	urban and built-up land
14	cropland/grassland mosaic
15	snow/ice
16	barren or sparsely vegetated
17	water bodies
18	mixed tundra

Tab. 6.2.: Surface types as used in the CERES retrieval. Surface types 1-17 correspond to those defined by the INternational Geopshere-Biosphere Programme (IGBP)

6.5 TOA Instantaneous Shortwave and Longwave Fluxes

In order to compare the instantaneous short- and longwave fluxes two case studies were performed: One MODIS granule from the 20th of February 2008 over Greenland (see figure 6.4) and another from the 20th of March 2008 above central Africa (fig. 6.5). The collocation was performed according to section 6.3. The scatter plots in figure 6.4 (left column) show a high correlation between the CERES and ESA CCI with a Pearson correlation coefficient of 0.93 for the short- and longwave fluxes. Colourized are the surface types used by CERES as an indicator if any type of surface causes a systematic bias between both products (see table 6.2 for definitions). In the middle and right column of figure 6.4 the ESA CCI flux and the difference of ESA CCI-CERES are depicted. Here, BUGSrad refers to the used radiative transfer model in the CC4CL retrieval of ESA CCI. As seen in comparison of the annual average, the shortwave TOA flux of ESA CCI is smaller than the retrieved flux from CERES for snow covered ground. In the longwave regime the scene shows a prominent positive bias towards CERES in the inner part of Greenland, while the longwave

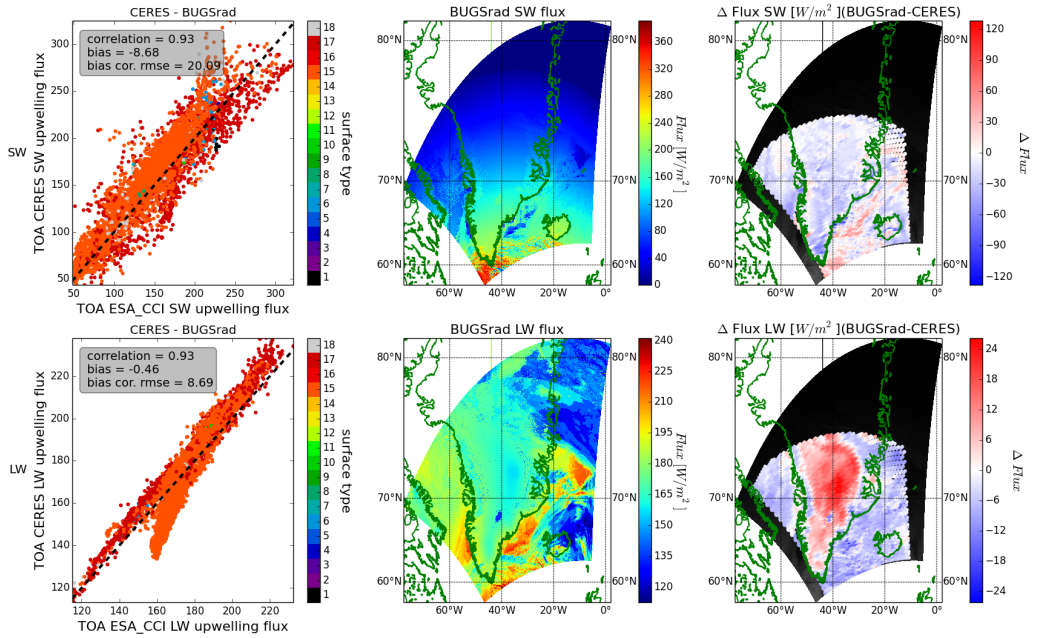

Fig. 6.4.: Shortwave TOA flux comparison between ESA CCI and CERES SSF. The presented scene is from the 20th of February 2008, covering the southern part of Greenland.

radiative flux from coastal regions and the surrounding water bodies is lower in the ESA CCI product. In the case of central African scene in figure 6.5, the Pearson correlation coefficients are also high with c = 0.98 for the shortwave and c = 0.99 in the longwave. The bias between both products is for the shortwave at $17.15\ W/m^2$ and for the longwave $-7.61\ W/m^2$. The shortwave retrieval shows a positive bias for most of the MODIS granule, with a strong negative bias in the upper left corner. Looking into the cloud parameters going in the CC4CL retrieval the negative bias coincides with ice-particle clouds. Due to a bug in the LUT's of the cloud product the MODIS Aqua cloud retrieval of ESA CCI yields on average higher cloud effective radii for ice particles as MODIS collection 6 (see Cloud CCI PVIR, Stapelberg et al. (2018): figure 4-62), altering the radiative properties of the cloud and therefore will cause deviations from the CERES product. In the longwave regime the retrieval yields lower values as CERES, agreeing with the comparison of the annual averages. In both scenes no specific surface type correlates with the found differences in top of atmosphere flux.

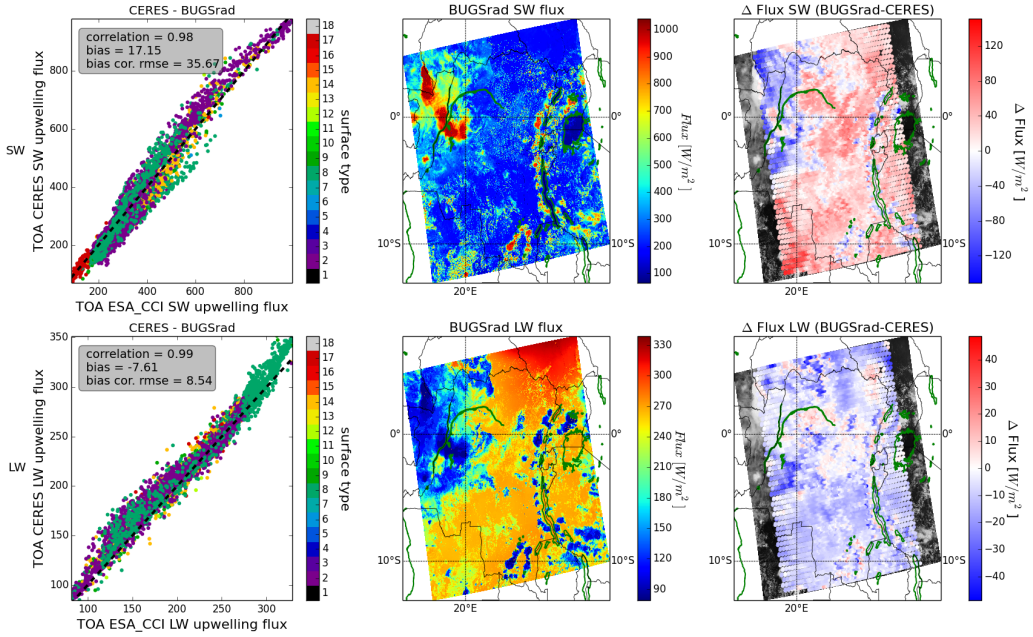

Fig. 6.5.: Shortwave TOA flux comparison between ESA CCI and CERES SSF. The presented scene is from the 20th of March 2008, above central Africa.

6.6 Summary

In this study, the ESA CCI TOA short- and longwave flux was compared to the CERES derived values. The annual average of 2008 did show a large positive bias for most of the globe, with the exception of the Antarctic were a negative bias could be found. Longwave flux on the other hand are globally dominated by a slight negative bias. However, applying the simple diurnal cycle correction reduces the bias considerably for the shortwave flux, while the longwave flux impacted less. After the correction, the difference in shortwave flux is mostly within $20W/m^2$, whereby the CC4CL based flux retrieval yields consistently lower values for regions with a high temporal snow/ice coverage.
Instantaneous flux retrievals did show a similar behaviour. In the inland of Greenland the shortwave flux was underestimated compared to CERES, while the longwave flux was overestimated in this region. For the central African case the shortwave mainly showed a larger flux as CERES, except in the north-western part of the scene, where a high coverage of ice clouds was apparent. An error in the underlying cloud retrievals LUT at the time of this study, yielded higher cloud effective radii, which then affects the retrieved TOA shortwave flux. Longwave flux correlates well with the annual comparison, insofar as that the flux is underestimated for the ESA CCI retrieval.
Overall, the ESA CCI retrieval produces TOA flux values which deviate strongly from the CERES retrieved values by up to $\pm 10\%$.

7 Summary & Outlook

The impact on cloud vertical extinction profiles and cloud extent on the retrieval of cloud top pressure with the O_2 A band method are known for more than 20 years (Fischer and Grassl, 1991). Also in climate models the respresentation of vertical distribution of clouds in the atmosphere has proven to be a large source of error, which is strongly evaluated in the last years due to the data provided by the CloudSat and CALIPSO missions (Stein et al. (2015), Bodas-Salcedo et al. (2011), Naud et al. (2010)). While the active instruments inherently provide vertical profiles of the atmosphere, it is not as easy to retrieve the vertical structure of the cloud from passive instruments measurents in the O_2 A band. Various studies employing different instrumental possibilities have been performed in order to improve cloud property retrievals. Sanghavi et al. (2015) and Richardson et al. (2018) make use of hyperspectral measurements in the O_2 A band with the Orbiting Carbon Observatory-2 (OCO-2), when retrieving cloud properties. In their works the different strengths of the individual absorption lines is used, in order to better determine cloud top pressure and vertical extent and optical depth. Ferlay et al. (2010) made use of the multidirectional measurements of POLDER-3/PARASOL in order to derive a cloud vertical extent, which lead combined with their findings that the retrieved cloud pressure corresponds well with the cloud middle to an improved cloud top pressure retrieval. This work focused on including cloud vertical extinction profiles into the established method of the O_2 A band retrieval for cloud top heights. The main questions to be investigated were:

- the impact of cloud vertical profiles on the quality of cloud top heights.

- the possibility of an expansion of the well-known retrieval towards the derivation of simultaneous cloud top height, cloud optical depth and cloud vertical profile through the use of additional spectral measurements in the O_2 A band, as featured by the Ocean and Land Colour Instrument on board of the European Space Agencies satellite series Sentinel-3.

- the support of such a retrieval by providing a priori information by other means.

Therefore, a sensitivity study based on radiative transfer simulations was performed, using a parametrized representation of the cloud vertical extent based on the geometrical thickness and distribution of cloud optical depth. The study revealed, that the sensitivity of the top of atmosphere signal, given by the channel ratios between absorption channel and atmospheric window channel, towards the vertical extinction profile is similar to the sensitivity towards the cloud top pressure and when not included in the underlying model is the largest source of uncertainty for the retrieval.
However, an analysis of the degrees of freedom for the optimal estimation based retrieval revealed, for most cloud scenarios two independent parameters can be determined by the information from all four OLCI channels. One of these degrees of freedom has to be used for the cloud optical depth, leaving one for a combination of cloud top pressure, extent and mode.
In a next step, a pre-processor was developed to support the proposed cloud property retrieval with a priori knowledge of the cloud vertical extinction profile. The approach uses texture analysis of a cloudy pixel's vicinity based on a single band radiance. A random forest classifier then assigns a class label based on the calculated texture parameters. This method was able to reproduce CloudSat based cloud classification to a high degree as well as assign labels, based on discrete values of cloud vertical extent or mode, to clouds. The applied technique is elementary, since the classification is based on the texture parameters of a single spectral channel only. Also, the studied spectral bands were limited to the visible and near infrared spectrum to mimic OLCI's capabilities. A more advanced technique including the combination of several spectral channels as well as raw radiances might lead to further improvements.
Evaluation of the OLCI cloud property retrieval with CloudSat measurements supported the results of the previous studies. In three variants of the OLCI retrieval the least agreement with CloudSat for mode, cloud top and bottom height was achieved when none of the parameters was confined. The best results were achieved, when the cloud top height, through the a priori state, was forced to yield CloudSat like values. However, an overall improvement between the agreement of CloudSat and the O_2 A band method could be seen when comparing the results of the FAME-C MERIS retrieval with OLCI. The amount of data points for OLCI are not comparable with MERIS' amount of data, though the better agreement indicates that the inclusion of vertical profile, combined with the additional absorption channels, yields an

improvement in the cloud top height derivation. Therefore, further studies have to be performed to better quantify the influence of the retrieval modifications.
In the end, a validation study for the ESA Climate Change Initiative Cloud (CCI Cloud) top of atmosphere radiative flux product is presented. As reference data set the Clouds and the Earth's Radiant Energy System (CERES) was used. The flux retrieval algorithm is part of the Community Code for Climate (CC4CL). The comparison of annual global flux estimates pointed out, that the derived shortwave fluxes are underestimated over snowy surfaces, while globally the flux is slighty overestimated. Longwave fluxes are generally underestimated in CC4CL. Instantaneous flux estimates showed differences in the bias corrected root-mean-square deviation by up to $35W/m^2$ in the shortwave and $8.5W/m^2$ in the longwave regime. Especially, snow covered surfaces lead to an overestimation of the longwave flux in the instantaneous data set. Overall, the annual averages show good agreement with CERES, reproducing the spatial distribution well. However, the instantaneous fluxes show large deviations in some cases. At least part of the deviations are originating from the differently retrieved cloud properties underlying the fluxes, showing clearly that there is still a need to improve cloud property retrievals in order to ensure accurate radiative flux retrievals.
A possibility for the improvement of cloud data products is a synergistic retrieval using OLCI and SLSTR similar to the FAME-C algorithm of Carbajal Henken et al. (2013). Here, either the cloud top height retrieved with SLSTR could be used as an input parameter of the OLCI retrieval, effectively fixing this parameter in the further calculation in order to retrieve only information about the vertical extinction profile. Another approach could be to integrate the SLSTR channels, performing a simultaneous retrieval of cloud top height, optical depth and vertical extinction profile. A well performing cloud property retrieval for the Sentinel-3 series instruments will yield a high temporal and spatial coverage with the four planned similar satellites in orbit at the same time, furthering our understanding of the processes in Earth's atmosphere.

Appendix

A

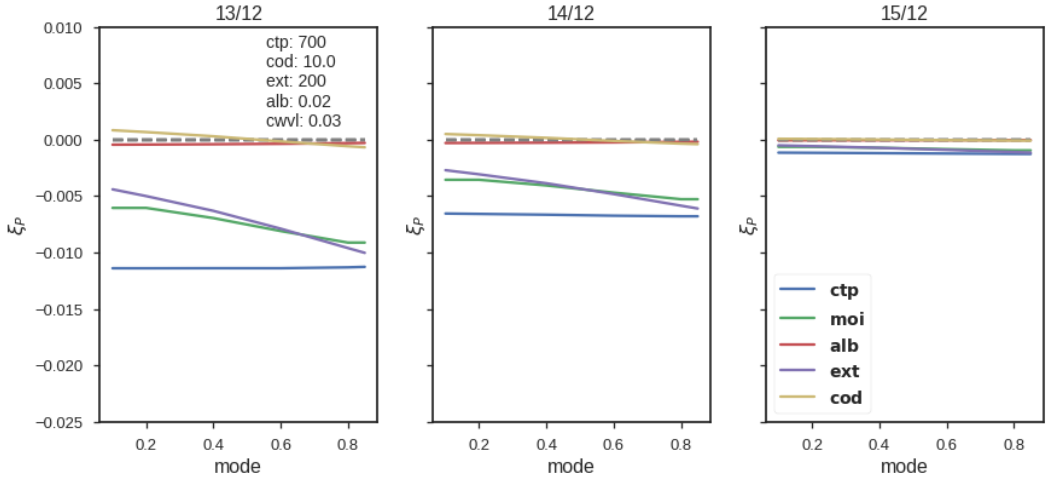

Fig. A.1.: Sensitivities of TOA radiances depending on the vertical distribution of cloud optical depth for a cloud with $ctp = 700hPa$, $\tau = 10$, an vertical extent $ext = 200$ and an underlying surface albedo of $\alpha = 0.02$ for channel ratios 13/12 (left), 14/12 (middle) and 15/12 (right).

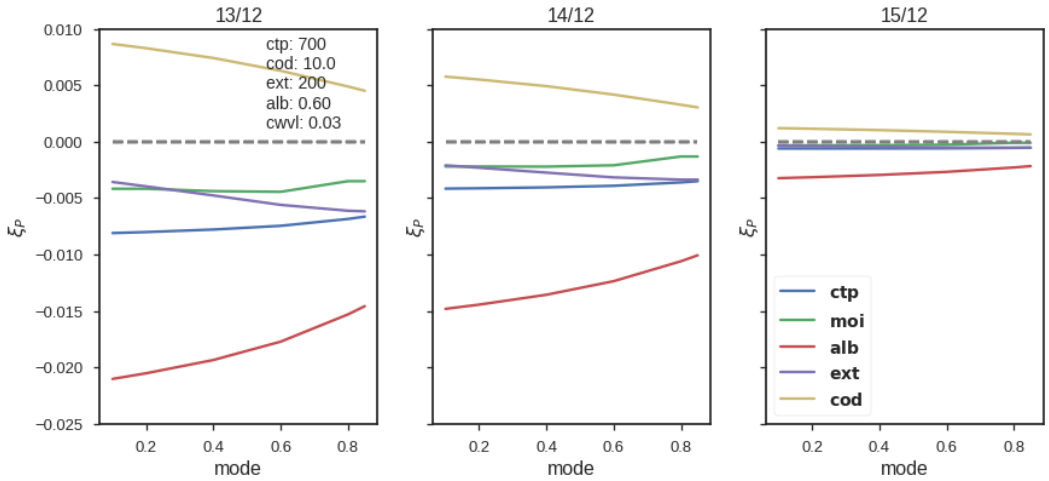

Fig. A.2.: Sensitivities of TOA radiances depending on the vertical distribution of cloud optical depth for a cloud with $ctp = 700hPa$, $\tau = 10$, an vertical extent $ext = 200$ and an underlying surface albedo of $\alpha = 0.6$ for channel ratios 13/12 (left), 14/12 (middle) and 15/12 (right).

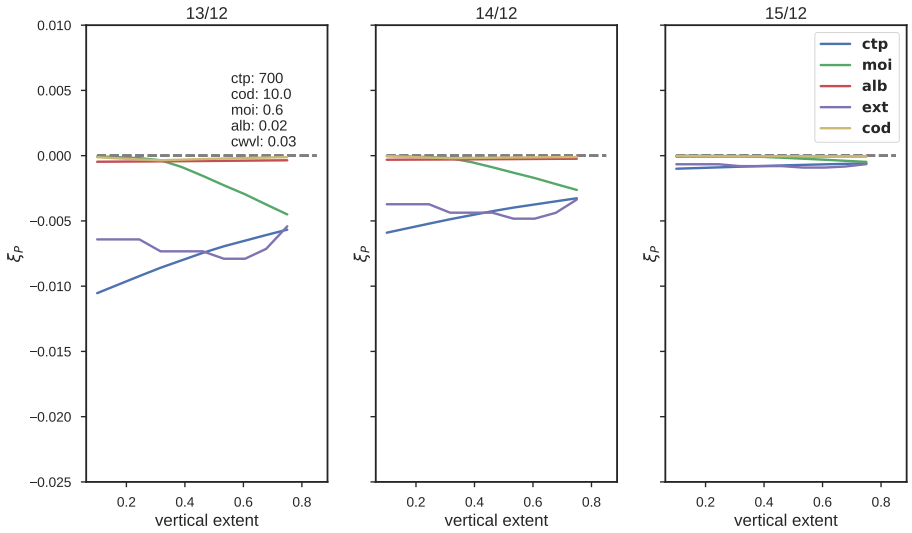

Fig. A.3.: Sensitivities of TOA radiances depending on the vertical extent of a cloud with $ctp = 700hPa$, $\tau = 10$, an mode of $moi = 0.6$ and an underlying surface albedo of $\alpha = 0.02$ for channel ratios 13/12 (left), 14/12 (middle) and 15/12 (right).

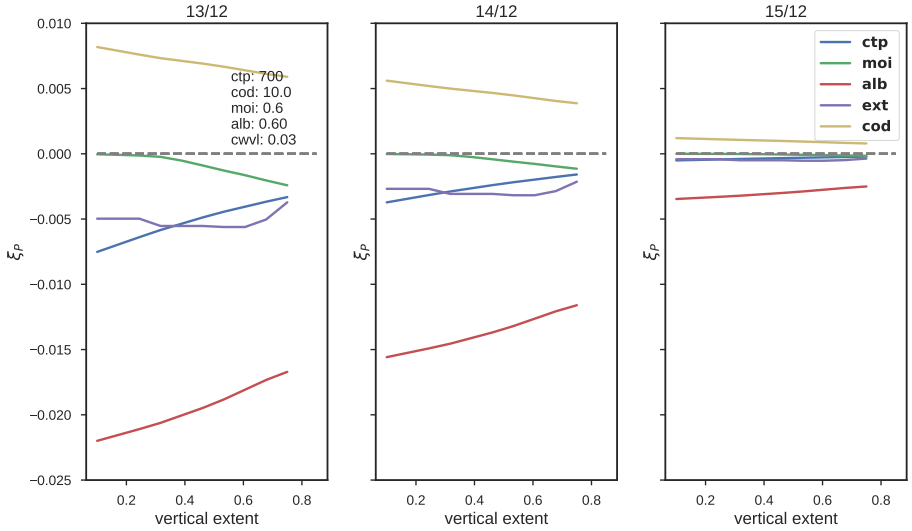

Fig. A.4.: Sensitivities of TOA radiances depending on the vertical extent of a cloud with $ctp = 700hPa$, $\tau = 10$, an mode of $moi = 0.6$ and an underlying surface albedo of $\alpha = 0.6$ for channel ratios 13/12 (left), 14/12 (middle) and 15/12 (right).

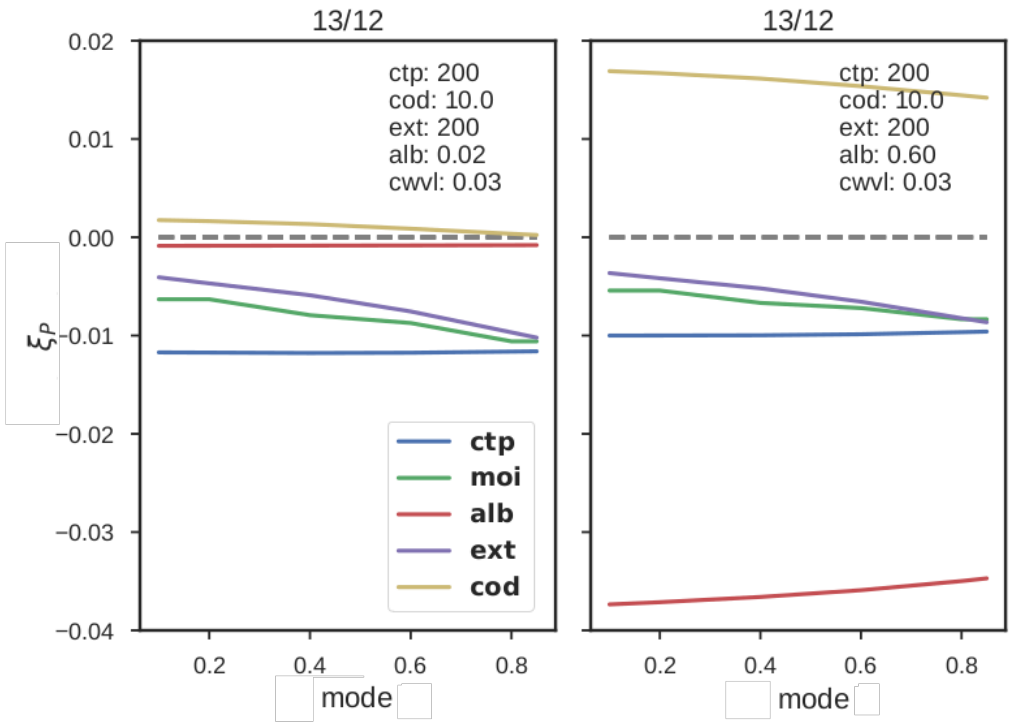

Fig. A.5.: Sensitivities of TOA radiances depending on the vertical distribution of cloud optical depth for a cloud with $ctp = 200hPa$, $\tau = 10$, an vertical extent $ext = 200$ and an underlying surface with $\alpha = 0.02$ (left) and $\alpha = 0.6$ (right).

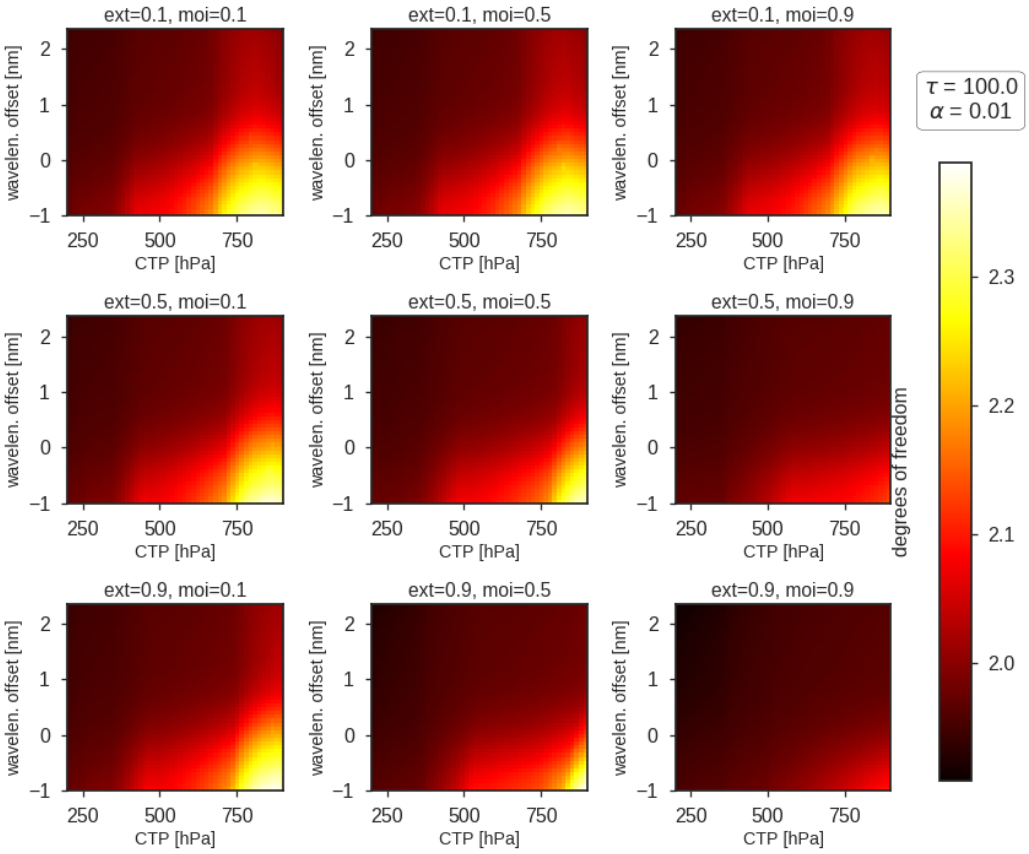

Fig. A.6.: Degrees of freedom for a measurement of a cloud with $\tau = 100$ and surface albedo $\alpha = 0.01$ depending on the central wavelength of the OLCI channels as well as the cloud top pressure. The degree of freedom is presented for different combinations of cloud vertical extent and mode of optical depth.

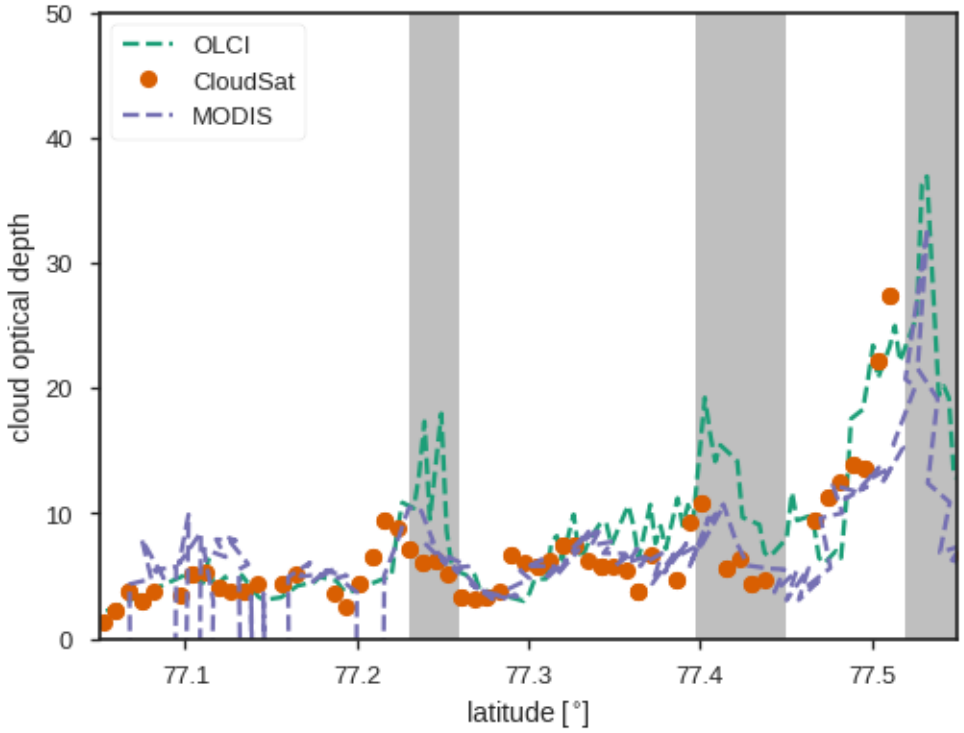

Fig. A.7.: CloudSat (orange circles), MODIS (purple dashed line) and OLCI (green dashed line) cloud optical depth as retrieved for the studied scene between latitudes of 77° and 77.5°. Here, the compared MODIS pixel is shifted by 3km westwards. Grey areas mark a significant difference in *COD* between OLCI and A-train for the unshifted case.

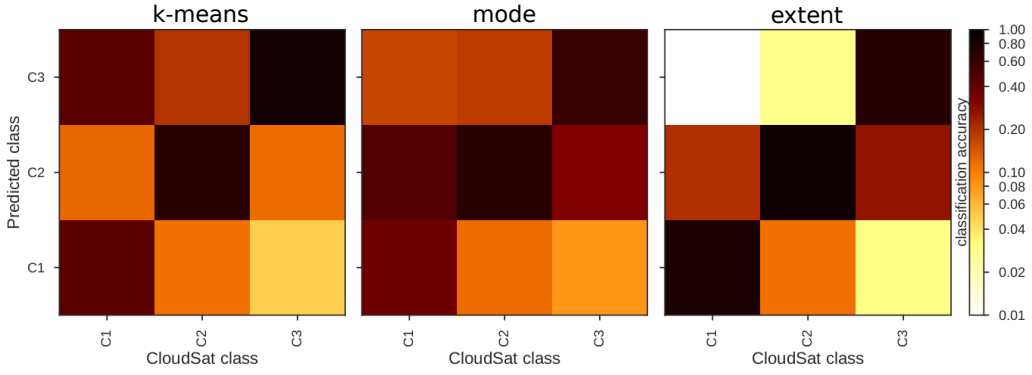

Fig. A.8.: 2-D histograms of classification into groups seperated by k-means clustering (left), mode (middle) and extent(right) for scenes above snow covered surface. Presented is the classification accuracy of each class.

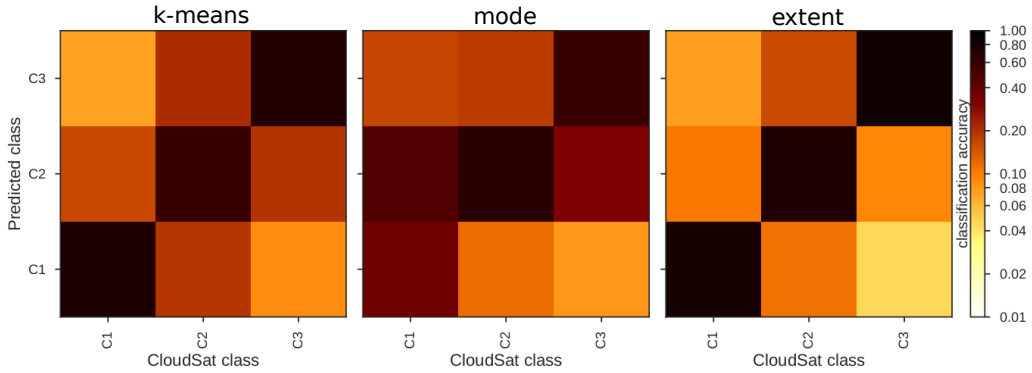

Fig. A.9.: 2-D histograms of classification into groups seperated by k-means clustering (left), mode (middle) and extent(right) for scenes above vegetated surface. Presented is the classification accuracy of each class.

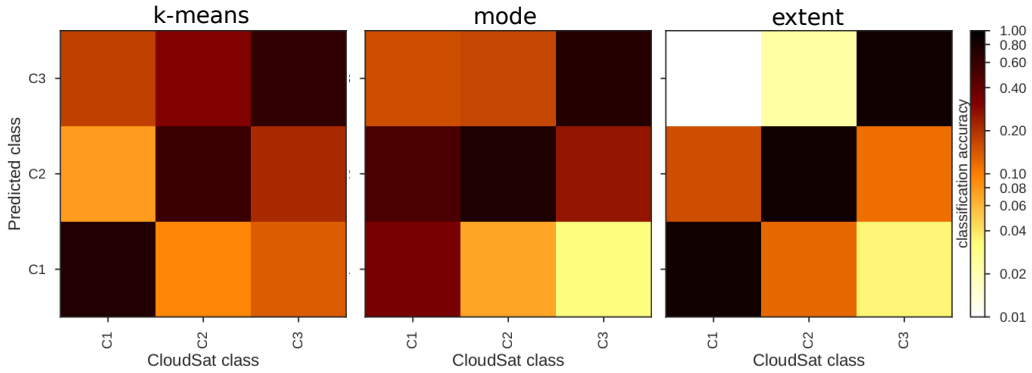

Fig. A.10.: 2-D histograms of classification into groups seperated by k-means clustering (left), mode (middle) and extent(right) for scenes above desert surface. Presented is the classification accuracy of each class.

Bibliography

Acarreta, J. R., Haan, J. F. D., and Stammes, P.: Cloud pressure retrieval using the O2-O2 absorption band at 477 nm, Journal of Geophysical Research: Atmospheres, 109, doi:10.1029/2003JD003915, URL https://agupubs.onlinelibrary.wiley.com/doi/abs/10.1029/2003JD003915, 2004.

Albrecht, B. A.: Aerosols, Cloud Microphysics, and Fractional Cloudiness, Science, 245, 1227–1230, doi:10.1126/science.245.4923.1227, 1989.

Augusteijn, M. F., Clemens, L. E., and Shaw, K. A.: Performance evaluation of texture measures for ground cover identification in satellite images by means of a neural network classifier, IEEE Transactions on Geoscience and Remote Sensing, 33, 616–626, doi:10.1109/36.387577, 1995.

Barkstrom, B. R., Harrison, E. F., Lee III, R. B., and Team, E. S.: Earth Radiation Budget Experiment, Eos, Transactions American Geophysical Union, 71, 297–304, doi:10.1029/EO071i009p00297, URL https://agupubs.onlinelibrary.wiley.com/doi/abs/10.1029/EO071i009p00297, 1990.

Bennartz, R. and Fischer, J.: A modified k -distribution approach applied to narrow band water vapour and oxygen absorption estimates in the near infrared, Journal of Quantitative Spectroscopy and Radiative Transfer, 66, 539–553, doi:10.1016/S0022-4073(99)00184-3, 2000.

Bodas-Salcedo, A., Webb, M. J., Bony, S., Chepfer, H., Dufresne, J. L., Klein, S. A., Zhang, Y., Marchand, R., Haynes, J. M., Pincus, R., and John, V. O.: COSP: Satellite simulation software for model assessment, Bulletin of the American Meteorological Society, doi:10.1175/2011BAMS2856.1, 2011.

Bohren, C. F. and Nevitt, T. J.: Absorption by a sphere: a simple approximation, Appl. Opt., 22, 774–775, doi:10.1364/AO.22.000774, URL http://ao.osa.org/abstract.cfm?URI=ao-22-6-774, 1983.

Breiman, L.: Random Forests, Machine Learning, 45, 5–32, doi:10.1023/A:1010933404324, URL https://doi.org/10.1023/A:1010933404324, 2001.

Buriez, J. C., Vanbauce, C., Parol, F., Goloub, P., Herman, M., Bonnel, B., Fouquart, Y., Couvert, P., and Seze, G.: Cloud detection and derivation of cloud properties from POLDER, International Journal of Remote Sensing, 18, 2785–2813, doi:10.1080/014311697217332, URL https://doi.org/10.1080/014311697217332, 1997.

Burrows, J. P., Weber, M., Buchwitz, M., Rozanov, V., Ladstätter-Weißenmayer, A., Richter, A., DeBeek, R., Hoogen, R., Bramstedt, K., Eichmann, K.-U., Eisinger, M., and Perner, D.: The Global Ozone Monitoring Experiment (GOME): Mission Concept and First Scientific Results, Journal of the Atmospheric Sciences, 56, 151–175, URL https://doi.org/10.1175/1520-0469(1999)056<0151:TGOMEG>2.0.CO;2, 1999.

Carbajal Henken, C. K., Lindstrot, R., Filipitsch, F., Walther, A., Preusker, R., and Fischer, J.: FAME-C: Retrieval of cloud top pressure with vertically inhomogeneous cloud profiles, AIP Conference Proceedings, 1531, 412–415, doi:10.1063/1.4804794, 2013.

Carbajal Henken, C. K., Lindstrot, R., Preusker, R., and Fischer, J.: FAME-C: cloud property retrieval using synergistic AATSR and MERIS observations, Atmospheric Measurement Techniques, 7, 3873–3890, doi:10.5194/amt-7-3873-2014, URL https://www.atmos-meas-tech.net/7/3873/2014/, 2014.

Carbajal Henken, C. K., Doppler, L., Lindstrot, R., Preusker, R., and Fischer, J.: Exploiting the sensitivity of two satellite cloud height retrievals to cloud vertical distribution, Atmospheric Measurement Techniques, 8, 3419–3431, doi:10.5194/amt-8-3419-2015, URL https://www.atmos-meas-tech.net/8/3419/2015/, 2015.

Christensen, M. W., Poulsen, C., McGarragh, G., and Grainger, R. G.: Algorithm Theoretical Basis Document (ATBD) of the Community Code for CLimate (CC4CL) Broadband Radiative Flux Retrieval (CC4CL-TOAFLUX) module, Tech. rep., ESA

Cloud CCI, available at: http://www.esa-cloud-cci.org (last access: 25 May 2018), 2016.

Collins, W. D., Rasch, P. J., Boville, B. A., Hack, J. J., Mccaa, J. R., Williamson, D. L., Kiehl, J. T., Briegleb, B., Bitz, C., jiann Lin, S., Zhang, M., and Dai, Y.: Description of the NCAR community atmosphere model (CAM3.0), Tech. rep., National Center For Atmospheric Research, 2004.

Colman, R.: A comparison of climate feedbacks in general circulation models, Climate Dynamics, 20, 865–873, doi:10.1007/s00382-003-0310-z, URL https://doi.org/10.1007/s00382-003-0310-z, 2003.

Doppler, L., Carbajal Henken, C., Pelon, J., Ravetta, F., and Fischer, J.: Extension of radiative transfer code MOMO, matrix-operator model to the thermal infrared – Clear air validation by comparison to RTTOV and application to CALIPSO-IIR, Journal of Quantitative Spectroscopy and Radiative Transfer, 144, 49 – 67, doi:https://doi.org/10.1016/j.jqsrt.2014.03.028, URL http://www.sciencedirect.com/science/article/pii/S0022407314001447, 2014a.

Doppler, L., Preusker, R., Bennartz, R., and Fischer, J.: k-bin and k-IR: k-distribution methods without correlation approximation for non-fixed instrument response function and extension to the thermal infrared—Applications to satellite remote sensing, Journal of Quantitative Spectroscopy and Radiative Transfer, 133, 382 – 395, doi:https://doi.org/10.1016/j.jqsrt.2013.09.001, URL http://www.sciencedirect.com/science/article/pii/S0022407313003567, 2014b.

Ebert, E. E.: A Pattern Recognition Technique for Distinguishing Surface and Cloud Types in the Polar Regions, Journal of Climate and Applied Meteorology, 26, 1412–1427, doi:10.1175/1520-0450(1987)026<1412:APRTFD>2.0.CO;2, URL https://doi.org/10.1175/1520-0450(1987)026<1412:APRTFD>2.0.CO;2, 1987.

Ebert, E. E.: Analysis of Polar Clouds from Satellite Imagery Using Pattern Recognition and a Statistical Cloud Analysis Scheme, Journal of Applied Meteorology, 28, 382–399, doi:10.1175/1520-0450, 1989.

Fell, F. and Fischer, J.: Numerical simulation of the light field in the atmosphere–ocean system using the matrix-operator method, Journal of Quantitative Spectroscopy and Radiative Transfer, 69, 351 – 388, doi:https://doi.

org/10.1016/S0022-4073(00)00089-3, URL http://www.sciencedirect.com/science/article/pii/S0022407300000893, 2001.

Ferlay, N., Thieuleux, F., Cornet, C., Davis, A. B., Dubuisson, P., Ducos, F., Parol, F., Riédi, J., and Vanbauce, C.: Toward New Inferences about Cloud Structures from Multidirectional Measurements in the Oxygen A Band: Middle-of-Cloud Pressure and Cloud Geometrical Thickness from POLDER-3/PARASOL, Journal of Applied Meteorology and Climatology, 49, 2492–2507, doi:10.1175/2010JAMC2550.1, URL https://doi.org/10.1175/2010JAMC2550.1, 2010.

Fischer, J. and Grassl, H.: Detection of Cloud-Top Height from Backscattered Radiances within the Oxygen A Band. Part 1: Theoretical Study, Journal of Applied Meteorology, 30, 1245–1259, doi:10.1175/1520-0450(1991)030<1245:DOCTHF>2.0.CO;2, URL https://doi.org/10.1175/1520-0450(1991)030<1245:DOCTHF>2.0.CO;2, 1991.

Fischer, J., Cordes, W., Schmitz-Peiffer, A., Renger, W., and Mörl, P.: Detection of Cloud-Top Height from Backscattered Radiances within the Oxygen A Band. Part 2: Measurements, Journal of Applied Meteorology, 30, 1260–1267, doi:10.1175/1520-0450(1991)030<1260:DOCTHF>2.0.CO;2, URL https://doi.org/10.1175/1520-0450(1991)030<1260:DOCTHF>2.0.CO;2, 1991.

Foster, M. J. and Heidinger, A.: PATMOS-x: Results from a Diurnally Corrected 30-yr Satellite Cloud Climatology, Journal of Climate, 26, 414–425, doi:10.1175/JCLI-D-11-00666.1, URL https://doi.org/10.1175/JCLI-D-11-00666.1, 2013.

Gleckler, P. J., Randall, D. A., Boer, G., Colman, R., Dix, M., Galin, V., Helfand, M., Kiehl, J., Kitoh, A., Lau, W., Liang, X., Lykossov, V., McAvaney, B., Miyakoda, K., Planton, S., and Stern, W.: Cloud-radiative effects on implied oceanic energy transports as simulated by Atmospheric General Circulation Models, Geophysical Research Letters, 22, 791–794, doi:10.1029/95GL00113, 1995.

Green, R. and Wielicki, B. A.: Clouds and the Earth's Radiant Energy System (CERES) Algorithm Theoretical Basis Document - Convolution of Imager Cloud Properties With CERES Footprint Point Spread Function (Subsystem 4.4), Tech. rep., Atmospheric Sciences Division, NASA Langley Research Center, Hampton, Virginia, 1997.

Hanel, R. A.: Determination of cloud altitude from a satellite, Journal of Geophysical Research, 66, 1300–1300, doi:10.1029/JZ066i004p01300, URL https://agupubs.onlinelibrary.wiley.com/doi/abs/10.1029/JZ066i004p01300, 1961.

Hansen, J. E.: Multiple Scattering of Polarized Light in Planetary Atmospheres Part II. Sunlight Reflected by Terrestrial Water Clouds, Journal of the Atmospheric Sciences, 28, 1400–1426, doi:10.1175/1520-0469(1971)028<1400:MSOPLI>2.0.CO;2, URL https://doi.org/10.1175/1520-0469(1971)028<1400:MSOPLI>2.0.CO;2, 1971.

Hansen, J. E. and Travis, L. D.: Light scattering in planetary atmospheres, Space Science Reviews, 16, 527–610, doi:10.1007/BF00168069, URL https://doi.org/10.1007/BF00168069, 1974.

Haralick, R. M., Shanmugam, K., and Dinstein, I.: Textural Features for Image Classification, IEEE Transactions on Systems, Man, and Cybernetics, SMC-3, 610–621, doi:10.1109/TSMC.1973.4309314, 1973.

Heinle, A., Macke, A., and Srivastav, A.: Automatic cloud classification of whole sky images, Atmospheric Measurement Techniques, 3, 557–567, doi:10.5194/amt-3-557-2010, 2010.

Hollmann, R., Merchant, C. J., Saunders, R., Downy, C., Buchwitz, M., Cazenave, A., Chuvieco, E., Defourny, P., de Leeuw, G., Forsberg, R., Holzer-Popp, T., Paul, F., Sandven, S., Sathyendranath, S., van Roozendael, M., and Wagner, W.: The ESA Climate Change Initiative: Satellite Data Records for Essential Climate Variables, Bulletin of the American Meteorological Society, 94, 1541–1552, doi:10.1175/BAMS-D-11-00254.1, URL https://doi.org/10.1175/BAMS-D-11-00254.1, 2013.

Hollstein, A.: Vector Radiative Transfer and its Application to the Remote Sensing of Aerosols and Hydrosols, Ph.D. thesis, Freie Universität Berlin, 2013.

Hollstein, A., Fischer, J., Carbajal Henken, C. K., and Preusker, R.: Bayesian cloud detection for MERIS, AATSR, and their combination, Atmospheric Measurement Techniques, 8, 1757–1771, doi:10.5194/amt-8-1757-2015, URL https://www.atmos-meas-tech.net/8/1757/2015/, 2015.

Ilanthiryan, S., Mathur, A. K., and Agarwal, V. K.: Cloud height determination using satellite stereoscopy from Along Track Scanning Radiometer onboard ERS-1 satellite: A simulation study, Journal of the Indian Society of Remote Sensing, 20, 51–63, doi:10.1007/BF02991885, URL https://doi.org/10.1007/BF02991885, 1992.

IPCC: Climate Change 2013: The Physical Science Basis. Contribution of Working Group I to the Fifth Assessment Report of the Intergovernmental Panel on Climate Change, Cambridge University Press, Cambridge, United Kingdom and New York, NY, USA, doi:10.1017/CBO9781107415324, URL www.climatechange2013.org, 2013.

Joiner, J., Vasilkov, A. P., Flittner, D. E., Gleason, J. F., and Bhartia, P. K.: Retrieval of cloud pressure and oceanic chlorophyll content using Raman scattering in GOME ultraviolet spectra, Journal of Geophysical Research: Atmospheres, 109, doi:10.1029/2003JD003698, URL https://agupubs.onlinelibrary.wiley.com/doi/abs/10.1029/2003JD003698, 2004.

Kandel, R., Viollier, M., Raberanto, P., Duvel, J. P., Pakhomov, L. A., Golovko, V. A., Trishchenko, A. P., Mueller, J., Raschke, E., Stuhlmann, R., and the International ScaRaB Scientific Working Group (ISSWG): The ScaRaB Earth Radiation Budget Dataset, Bulletin of the American Meteorological Society, 79, 765–784, URL https://doi.org/10.1175/1520-0477(1998)079<0765:TSERBD>2.0.CO;2, 1998.

Khazenie, N. and Richardson, K.: Comparison of Texture Analysis Techniques in Both Frequency and Spatial Domains for Cloud Feature Extraction, International Archives of Photogrammetry and Remote Sensing, 29, 1009–1014, 1993.

Kittler, J. and Pairman, D.: Contextual Pattern Recognition Applied to Cloud Detection and Identification, IEEE Transactions on Geoscience and Remote Sensing, GE-23, 855–863, doi:10.1109/TGRS.1985.289471, 1985.

Knibbe, W. J. J., de Haan, J. F., Hovenier, J. W., Stam, D. M., Koelemeijer, R. B., and Stammes, P.: Deriving terrestrial cloud top pressure from photopolarimetry of reflected light, Journal of Quantitative Spectroscopy and Radiative Transfer, 64, 173 – 199, doi:https://doi.org/10.1016/S0022-4073(98)00135-6, 2000.

Kuze, A. and Chance, K.: Analysis of cloud top height and cloud coverage from satellites using the O2 A and B bands, Journal of Geophysical Research: Atmospheres, 99, 14 481–14 491, doi:10.1029/94JD01152, URL https://agupubs.onlinelibrary.wiley.com/doi/abs/10.1029/94JD01152, 1994.

Lindstrot, R., Preusker, R., Ruhtz, T., Heese, B., Wiegner, M., Lindemann, C., and Fischer, J.: Validation of MERIS Cloud-Top Pressure Using Airborne Lidar Measurements, Journal of Applied Meteorology and Climatology, 45, 1612–1621, doi:10.1175/JAM2436.1, URL https://journals.ametsoc.org/doi/abs/10.1175/JAM2436.1, 2006.

McClatchey, R., Fenn, R., Selby, J., Volz, F., and Garing, J.: Optical Properties of the Atmosphere, 3rd ed. Air Force Cambridge Research Laboratories, 1972.

McGarragh, G. R., Poulsen, C. A., Thomas, G. E., Povey, A. C., Sus, O., Stapelberg, S., Schlundt, C., Proud, S., Christensen, M. W., Stengel, M., Hollmann, R., and Grainger, R. G.: The Community Cloud retrieval for CLimate (CC4CL). Part II: The optimal estimation approach, Atmospheric Measurement Techniques Discussions, 2017, 1–55, doi:10.5194/amt-2017-333, URL https://www.atmos-meas-tech-discuss.net/amt-2017-333/, 2017.

Menzel, W. P., Smith, W. L., and Stewart, T. R.: Improved Cloud Motion Wind Vector and Altitude Assignment Using VAS, Journal of Climate and Applied Meteorology, 22, 377–384, doi:10.1175/1520-0450(1983)022<0377:ICMWVA>2.0.CO;2, URL https://doi.org/10.1175/1520-0450(1983)022<0377:ICMWVA>2.0.CO;2, 1983.

Mlawer, E. J., Payne, V. H., Moncet, J.-L., Delamere, J. S., Alvarado, M. J., and Tobin, D. C.: Development and recent evaluation of the MT_CKD model of continuum absorption, Philosophical Transactions of the Royal Society A: Mathematical, Physical and Engineering Sciences, doi:10.1098/rsta.2011.0295, 2012.

Naud, C. M., Del Genio, A. D., Bauer, M., and Kovari, W.: Cloud Vertical Distribution across Warm and Cold Fronts in CloudSat–CALIPSO Data and a General Circulation Model, Journal of Climate, 23, 3397–3415, doi:10.1175/2010JCLI3282.1, URL https://doi.org/10.1175/2010JCLI3282.1, 2010.

O'Brien, D. M. and Mitchell, R. M.: Error Estimates for Retrieval of Cloud-Top Pressure Using Absorption in the A Band of Oxygen, Journal of Applied Meteorology, 31, 1179–1192, doi:10.1175/1520-0450(1992)031<1179:EEFROC>2.0.CO;2, URL https://doi.org/10.1175/1520-0450(1992)031<1179:EEFROC>2.0.CO;2, 1992.

Petty, G. W.: A First Course in Atmospheric Radiation, Sundog Pub, 2006.

Plass, G. N., Kattawar, G. W., and Catchings, F. E.: Matrix Operator Theory of Radiative Transfer. 1: Rayleigh Scattering, Appl. Opt., 12, 314–329, doi:10.1364/AO.12.000314, URL http://ao.osa.org/abstract.cfm?URI=ao-12-2-314, 1973.

Polonsky, I. N., Labonnote, L. C., and Cooper, S.: Level 2 Cloud Optical Depth Product Process Description and Interface Control Document, Cooperative Institute for Research in the Atmosphere, URL http://www.cloudsat.cira.colostate.edu/sites/default/files/products/files/2B-TAU_PDICD.P_R04.20080220.pdf, 2008.

Preusker, R. and Lindstrot, R.: Remote sensing of cloud-top pressure using moderately resolved measurements within the oxygen A band - A sensitivity study, Journal of Applied Meteorology and Climatology, doi:10.1175/2009JAMC2074.1, 2009.

Preusker, R., Lindstrot, R., and Fischer, J.: MERIS Cloud-Top Pressure Algorithm Theoretical Basis Document ATBD 2.3, Tech. rep., Freie Universität Berlin, Institute for Space Sciences, URL https://earth.esa.int/documents/700255/2042855/MERIS_ATBD_2.3_v4.2+-+2011.pdf, 2010.

Ramanathan, V., Cess, R. D., Harrison, E. F., Minnis, P., Barkstrom, B. R., Ahamd, E., and Hartmann, D.: Cloud-Radiative Forcing and Climate: Results from the Earth Radiation Budget Experiment, Science, 243, 57–63, doi:10.1126/science.243.4887.57, URL http://science.sciencemag.org/content/243/4887/57, 1989.

Richardson, M., Stephens, G. L., and Stephens, G. L.: Information content of OCO-2 oxygen A-band channels for retrieving marine liquid cloud properties, Atmospheric Measurement Techniques, 11, 1515–1528, URL https://www.ingentaconnect.com/content/doaj/18671381/2018/00000011/00000001/art00076, 2018.

Rodgers, C. D.: Inverse Methods for Atmospheric Sounding: Theory and Practice, World Scientific Publishing, 2000.

Rossow, W. B. and Schiffer, R. A.: Advances in Understanding Clouds from ISCCP, Bulletin of the American Meteorological Society, 80, 2261–2288, doi:10.1175/1520-0477(1999)080<2261:AIUCFI>2.0.CO;2, 1999.

Rothman, L. S., Gordon, I. E., Babikov, Y., Barbe, A., Chris Benner, D., Bernath, P. F., Birk, M., Bizzocchi, L., Boudon, V., Brown, L. R., Campargue, A., Chance, K., Cohen, E. A., Coudert, L. H., Devi, V. M., Drouin, B. J., Fayt, A., Flaud, J. M., Gamache, R. R., Harrison, J. J., Hartmann, J. M., Hill, C., Hodges, J. T., Jacquemart, D., Jolly, A., Lamouroux, J., Le Roy, R. J., Li, G., Long, D. A., Lyulin, O. M., Mackie, C. J., Massie, S. T., Mikhailenko, S., Müller, H. S., Naumenko, O. V., Nikitin, A. V., Orphal, J., Perevalov, V., Perrin, A., Polovtseva, E. R., Richard, C., Smith, M. A., Starikova, E., Sung, K., Tashkun, S., Tennyson, J., Toon, G. C., Tyuterev, V. G., and Wagner, G.: The HITRAN2012 molecular spectroscopic database, Journal of Quantitative Spectroscopy and Radiative Transfer, doi:10.1016/j.jqsrt.2013.07.002, 2013.

Rozanov, V. V. and Kokhanovsky, A. A.: Semianalytical cloud retrieval algorithm as applied to the cloud top altitude and the cloud geometrical thickness determination from top-of-atmosphere reflectance measurements in the oxygen A band, Journal of Geophysical Research: Atmospheres, 109, doi:10.1029/2003JD004104, URL https://agupubs.onlinelibrary.wiley.com/doi/abs/10.1029/2003JD004104, 2004.

Saiedy, F., Jacobowitz, H., and Wark, D. Q.: On Cloud-Top Determination from Gemini-5, Journal of the Atmospheric Sciences, 24, 63–69, doi:10.1175/1520-0469(1967)024<0063:OCTDFG>2.0.CO;2, URL https://doi.org/10.1175/1520-0469(1967)024<0063:OCTDFG>2.0.CO;2, 1967.

Sanghavi, S., Lebsock, M., and Stephens, G.: Sensitivity analysis of polarimetric O_2 A-band spectra for potential cloud retrievals using OCO-2/GOSAT measurements, Atmospheric Measurement Techniques, 8, 3601–3616, doi:10.5194/amt-8-3601-2015, URL https://www.atmos-meas-tech.net/8/3601/2015/, 2015.

Sassen, K. and Wang, Z.: Classifying clouds around the globe with the CloudSat radar: 1-year of results, Geophysical Research Letters, 35, n/a–n/a, doi:10.1029/2007GL032591, URL http://dx.doi.org/10.1029/2007GL032591, l04805, 2008.

Schröder, M., Bennartz, R., Schüller, L., Preusker, R., Albert, P., and Fischer, J.: Generating cloudmasks in spatial high-resolution observations of clouds using texture and radiance information, International Journal of Remote Sensing, 23, 4247–4261, doi:10.1080/01431160110114547, 2002.

Stapelberg, S., Stengel, M., Schlundt, C., Karlsson, K.-G., Meirink, J. F., Poulsen, C., Bojanowski, J., and Stöckli, R.: ESA Cloud_cci Product Validation and Intercomparison Report (PVIR), Tech. rep., ESA Cloud CCI, available at: http://www.esa-cloud-cci.org (last access: 25 May 2018), 2018.

Stein, T. H. M., Parker, D. J., Hogan, R. J., Birch, C. E., Holloway, C. E., Lister, G. M. S., Marsham, J. H., and Woolnough, S. J.: The representation of the West African monsoon vertical cloud structure in the Met Office Unified Model: an evaluation with CloudSat, Quarterly Journal of the Royal Meteorological Society, 141, 3312–3324, doi:10.1002/qj.2614, 2015.

Stengel, M., Stapelberg, S., Sus, O., Schlundt, C., Poulsen, C., Thomas, G., Christensen, M., Carbajal Henken, C. K., Preusker, R., Fischer, J., Devasthale, A., Willén, U., Karlsson, K.-G., McGarragh, G. R., Proud, S., Povey, A. C., Grainger, R. G., Meirink, J. F., Feofilov, A., Bennartz, R., Bojanowski, J. S., and Hollmann, R.: Cloud property datasets retrieved from AVHRR, MODIS, AATSR and MERIS in the framework of the Cloud_cci project, Earth System Science Data, 9, 881–904, doi:10.5194/essd-9-881-2017, URL https://www.earth-syst-sci-data.net/9/881/2017/, 2017.

Stephens, G. L., Gabriel, P. M., and Partain, P. T.: Parameterization of Atmospheric Radiative Transfer. Part I: Validity of Simple Models, Journal of the Atmospheric Sciences, 58, 3391–3409, doi:10.1175/1520-0469(2001)058<3391:POARTP>2.0.CO;2, 2001.

Stephens, G. L., Vane, D. G., Boain, R. J., Mace, G. G., Sassen, K., Wang, Z., Illingworth, A. J., O'connor, E. J., Rossow, W. B., Durden, S. L., Miller, S. D., Austin, R. T., Benedetti, A., Mitrescu, C., and the CloudSat Science Team: The CloudSat

mission and the A-Train, Bulletin of the American Meteorological Society, 83, 1771–1790, doi:10.1175/BAMS-83-12-1771, URL https://doi.org/10.1175/BAMS-83-12-1771, 2002.

Stephens, G. L., Li, J., Wild, M., Clayson, C. A., Loeb, N., Kato, S., L'Ecuyer, T., Stackhouse, P. W., Lebsock, M., and Andrews, T.: An update on Earth's energy balance in light of the latest global observations, Nature Geoscience, doi:10.1038/ngeo1580, 2012.

Stubenrauch, C. J., Rossow, W. B., Kinne, S., Ackerman, S., Cesana, G., Chepfer, H., Di Girolamo, L., Getzewich, B., Guignard, A., Heidinger, A., Maddux, B. C., Menzel, W. P., Minnis, P., Pearl, C., Platnick, S., Poulsen, C., Riedi, J., Sun-Mack, S., Walther, A., Winker, D., Zeng, S., and Zhao, G.: Assessment of global cloud datasets from satellites: Project and database initiated by the GEWEX radiation panel, Bulletin of the American Meteorological Society, doi:10.1175/BAMS-D-12-00117.1, 2013.

Sus, O., Stengel, M., Stapelberg, S., McGarragh, G., Poulsen, C., Povey, A. C., Schlundt, C., Thomas, G., Christensen, M., Proud, S., Jerg, M., Grainger, R., and Hollmann, R.: The Community Cloud retrieval for Climate (CC4CL). Part I: A framework applied to multiple satellite imaging sensors, Atmospheric Measurement Techniques Discussions, 2017, 1–42, doi:10.5194/amt-2017-334, URL https://www.atmos-meas-tech-discuss.net/amt-2017-334/, 2017.

Thomas, G. E., Carboni, E., Sayer, A. M., Poulsen, C. A., Siddans, R., and Grainger, R. G.: Oxford-RAL Aerosol and Cloud (ORAC): aerosol retrievals from satellite radiometers, pp. 193–225, Springer Berlin Heidelberg, Berlin, Heidelberg, doi:10.1007/978-3-540-69397-0_7, URL https://doi.org/10.1007/978-3-540-69397-0_7, 2009.

Twomey, S.: The Influence of Pollution on the Shortwave Albedo of Clouds, Journal of the Atmospheric Sciences, 34, 1149–1152, doi:10.1175/1520-0469(1977)034<1149:TIOPOT>2.0.CO;2, 1977.

Von Bismarck, J.: Vibrational Raman Scattering of Liquid Water Quantitative Incorporation into a Numeric Radiative Transfer Model of the Atmosphere-Ocean System and Analysis of its Impact on Remote Sensing Applications, Ph.D. thesis, Freie Universität Berlin, 2016.

Wang, Z. and Sassen, K.: Level 2 Cloud Scenario Classification Product Process Description and Interface Control Document,Version 5.0, Tech. rep., Colorado State University, Cooperative Institute for Research in the Atmosphere, URL http://www.cloudsat.cira.colostate.edu/, 2007.

Weisz, E., Li, J., Menzel, W. P., Heidinger, A. K., Kahn, B. H., and Liu, C.: Comparison of AIRS, MODIS, CloudSat and CALIPSO cloud top height retrievals, Geophysical Research Letters, 34, doi:10.1029/2007GL030676, URL https://agupubs.onlinelibrary.wiley.com/doi/abs/10.1029/2007GL030676, 2007.

Welch, R. M., Sengupta, S. K., and Chen, D. W.: Cloud field classification based upon high spatial resolution textural features: 1. Gray level co-occurrence matrix approach, Journal of Geophysical Research: Atmospheres, 93, 12 663–12 681, doi:10.1029/JD093iD10p12663, URL http://dx.doi.org/10.1029/JD093iD10p12663, 1988.

Wielicki, B. A., Barkstrom, B. R., Harrison, E. F., III, R. B. L., Smith, G. L., and Cooper, J. E.: Clouds and the Earth's Radiant Energy System (CERES): An Earth Observing System Experiment, Bulletin of the American Meteorological Society, 77, 853–868, doi:10.1175/1520-0477(1996)077<0853:CATERE>2.0.CO;2, URL https://doi.org/10.1175/1520-0477(1996)077<0853:CATERE>2.0.CO;2, 1996.

Wu, M.-L. C.: Remote Sensing of Cloud-Top Pressure Using Reflected Solar Radiation in the Oxygen A-Band, Journal of Climate and Applied Meteorology, 24, 539–546, doi:10.1175/1520-0450(1985)024<0539:RSOCTP>2.0.CO;2, URL https://doi.org/10.1175/1520-0450(1985)024<0539:RSOCTP>2.0.CO;2, 1985.

Wylie, D., Jackson, D. L., Menzel, W. P., and Bates, J. J.: Trends in global cloud cover in two decades of HIRS observations, Journal of Climate, doi:10.1175/JCLI3461.1, 2005.

Wylie, D. P. and Menzel, W. P.: Eight Years of High Cloud Statistics Using HIRS, Journal of Climate, 12, 170–184, doi:10.1175/1520-0442(1999)012<0170:EYOHCS>2.0.CO;2, URL https://journals.ametsoc.org/doi/abs/10.1175/1520-0442%281999%29012%3C0170%3AEYOHCS%3E2.0.CO%3B2, 1999.

Yamamoto, G. and Wark, D. Q.: Discussion of the letter by R. A. Hanel, "Determination of cloud altitude from a satellite", Journal of Geophysical Research, 66,

3596–3596, doi:10.1029/JZ066i010p03596, URL http://dx.doi.org/10.1029/JZ066i010p03596, 1961.

List of Figures

1.1 Global annual mean energy budget of Earth for the years 2000-2010. All fluxes are in W/m^2 (Stephens et al., 2012). 2

1.2 IPCC AR5: Global average radiative forcing estimates for 2011 relative to 1750. The cloud adjustments due to aerosols form the largest uncertainty in the determined radiative forcing (IPCC, 2013). 4

1.3 Time frames for the different satellite based instruments contributing to ESA's Cloud_CCI climate data record, from Stengel et al. (2017). The NOAA (AVHRR) morning and afternoon satellite measurements are also collected in the PATMOS-x dataset. 7

2.1 Scattering phase function for different size distributions for water clouds. 16

2.2 Schematic of adding and doubling in MOMO. Each original layer is divided in 2^n elementary layers, which are than added to retrieve R, T and J. By applying the adding method for each original layer the matrix operators for the complete atmosphere are retrieved. 18

2.3 CGASA transmission calculations of the oxygen absorption band A. . . 21

2.4 Schematic of photon path length extension due to in cloud multiple scattering. The penetration depth determines the probability of multiple scattering taking place 23

3.1 Visualization of cloud extent and cloud mode. The extent (red) is the relative part of the atmosphere ranging from cloud top to surface covered by the cloud. The mode (blue) is the relative coordinate of the maximal optical depth inside the cloud, h denotes the height. 28

3.2 Left: OLCI central wavelength of instrument response function for channels 12 to 15 (top to bottom) as a function of the spatial ccd column for all 5 camera modules (M1-M5). Right: full width at half maximum for the same channels. 31

3.3 Sensitivity of the channel ratios (13/12; 14/12; 15/12, from left to right) towards changes in the atmospheric state, dependent on the central wavelength of the absorbing channels. The grey dashed line represents the nominal centre wavelength. 34

3.4 Similar to figure 3.3, but with an surface albedo $\alpha = 0.6$. 35

3.5 Similar to figure 3.4, but with an cloud top pressure of $ctp = 200hPa$. . 35

3.6 Sensitivities for low (700hPA, top) and high (200hPa, bottom) cloud with surface albedo $\alpha = 0.6$ and cloud optical depth of $\tau = 100$. 36

3.7 Sensitivities of TOA radiances depending on the vertical distribution of cloud optical depth for a cloud with $ctp = 700hPa$, $\tau = 10$, a vertical extent $ext = 200$ and an underlying surface with $\alpha = 0.02$ (left) and $\alpha = 0.6$ (right). 37

3.8 Sensitivities of TOA radiances depending on the vertical extent for a cloud with $ctp = 700hPa$, $\tau = 10$, a vertical extent $ext = 200$ and an underlying surface with $\alpha = 0.02$ (left) and $\alpha = 0.6$ (right). 39

3.9 Degrees of freedom for a measurement of a cloud with $\tau = 1.3$ and surface albedo $\alpha = 0.01$ depending on the central wavelength of the OLCI channels as well as the cloud top pressure. The degrees of freedom are presented for different combinations of cloud vertical extent and mode of optical depth. 43

3.10 Degrees of freedom for a synthetic measurement of a cloud with $\tau = 10$ and surface albedo $\alpha = 0.01$ depending on the central wavelength of the OLCI channels as well as the cloud top pressure. The degrees of freedom are presented for different combinations of cloud vertical extent and mode of optical depth. 44

3.11 Degrees of freedom for a measurement of a cloud with varying τ and *ctp* depending on the surface albedo α. The degrees of freedom are presented for $ext = moi = 0.5$ and nominal channel wavelength ($d_{wvl} = 0$). Colors represent different cloud optical depth, while the solid and dashed lines are the cloud top heights of $200hPa$ and $800hPa$, respectively. 45

4.1 Schematic for grey level co-occurrence matrix calculation. The GLCM is always a quadratic matrix with i=j and maps the co-occurrence of the grey level values at distance d and angle θ towards each other. 49

4.2 Left: Total classification accuracy for different window sizes. Classification was performed for Band 1 250m (blue), artificially binned 1km (orange) resolution and Band 17 (green). All grey-level co-occurrence matrices are calculated with $d = 2$, $\theta = 0$ and $g = 8$. Right: Classification accuracy separated for each cloud type. 54

4.3 Comparison of grey-level image of MODIS Aqua Band 1 (left) and Band 17 (right) over snow covered surface. Band 17 exhibits a higher contrast especially around clouds. Coarse parts of the images are caused by saturation of the instruments channels. 55

4.4 Classification accuracy for band 1 and band 17 depending on the maximum number of grey-levels (left). Individual classification accuracy for each cloud type. Solid lines represent the classification with texture parameters from band 1 in full resolution, dashed represent band 17. . 56

4.5 Classification accuracy for band 1 and band 17 depending on the inter-pixel distance (left). Individual classification accuracy for each cloud type. Solid lines represent the classification with texture parameters from band 1 in full resolution, dashed lines represent band 17. 58

4.6 2D-histogram of texture based cloud typing. Left: classification scores for classification by radiation from band 17. The CloudSat cloud type is along the x-axis, the predicted class through the random forest classifier along the y-axis and the classification score is shown in colour. The histogram is normalized for each column. Right: difference in classification accuracy for band 1 and band 17. Positive values (red) correspond to higher hit scores for band 1 negative (blue) to higher scores for band 17 60

4.7 Top: 2D-histograms of the classification accuracy for 3 clustered classes. Bottom: Clustered data points for classification into three classes through (left) k-means clustering, (middle) manually along the mode of optical thickness and (right) along the relative vertical extent. . . . 62

4.8 The average classification accuracy for increasing number of possible labels. Division by the extent in blue, by mode in red and through k-means clustering in green. 64

4.9 Arrangement of the studied regions. The studied region of the previous sections is marked in yellow. Scenes above the desert are from the Taklamakan desert in Asia, marked in green, and snowy surfaces are taken from orbits over Greenland (orange). The forest scene is situated over South America (purple). 65

4.10 Right column: RGB image of typical scenes from the studied regions taken from the NASA Level-1 Atmosphere Archive & Distribution System Distributed Active Archive Center at Goddard Space Flight Center (LAADS DAAC `https://ladsweb.modaps.eosdis.nasa.gov/`). Left column: Classification scores of the cloudy pixels into cloud types. From top to bottom: Desert scene over Asia, South American rain forest and the snowy landscape of Greenland. 66

5.1 2D-histogram of CloudSat/CALIOP cloud fraction compared to FAME-C. The continuous cloud fractions was discretized into $clear \leq 0.5 < cloudy$. 75

5.2 Comparison of FAME-C *cth* based on AATSR (left) and MERIS (right) measurements with CloudSat/CALIOP combined product 2B-GEOPROF-LIDAR. The measurements have a maximal temporal offset of 3min and optically thin ($\tau < 1$) single-layer clouds as well as multi-layer clouds with an optically thick upper layer ($\tau > 2$) were filtered out. Bias and RMSD are in units of [km]. 76

5.3 Comparison of FAME-C *cth* based on AATSR with CloudSat/CALIOP combined product 2B-GEOPROF-LIDAR. Left for clouds with an AATSR retrieved height below 4km and right above 4km. The bias and RMSD calculation is based on the coloured measurements. Bias and RMSD are in units of [km]. 76

5.4 Similar to 5.3, but for MERIS. Left for clouds with an retrieved height below 4km and right above 6km. The heights between 4km and 6km neglected. Bias and RMSD are in units of [km]. 77

5.5 Case study area for Sentinel-3A OLCI (blue) and CloudSat CPR (green) cross-section on 11/06/2016. Main focus of this assessment study is on the region between latitudes of 77° and 77.4° (red circle). 79

5.6 CloudSat CPR layer optical depth measurement for the studied case between latitudes of 77° and 77.45°. Height (yellow), bottom (green) and mode (red) are overlayed. Orange dots mark the OLCI cloud fraction for the scene according to the right axis. The grey sectors mark areas, where retrieved the optical depth does not agree according to 5.7. 80

5.7 CloudSat (orange circles), MODIS (purple dashed line) and OLCI (green dashed line) cloud optical depth as retrieved for the studied scene between latitudes of 77° and 77.5°. Grey areas mark a significant difference in *COD* between OLCI and A-train measurements. 81

5.8 CloudSat CPR layer optical depth measurement for the studied case between latitudes of 77° and 77.5°. Cloud top height (yellow), bottom (green) and mode (red) of the OLCI cloud property retrieval are overlayed. The degrees of freedom for each successful measurement is shown in purple. Top, middle and lower panel represent different initialization conditions for the retrieval (see tab. 5.2). 83

5.9 Relative values for the retrieved extent (left) and mode (right). The blue line (1) is the CloudSat-like measurement, red (2) is for no restrictions on the state vector and green is calculated with no variation in mode and extent. Gaps in the data are caused by non-convergence of the optimal estimation algorithm. 84

5.10 Studied cloud scene with retrieved cloud top height (first panel). Normalized radiance for the Channels 12 (second panel), 13 (third panel), 14 (fourth panel) and 15 (last panel) of the OLCI retrieval forced to mirror CloudSat cloud top heights. The blue area represents the possible spread in the LUT's by variation of the mode and extent. Converged measurements are presented in yellow, while not converged ones are marked in red. Not converged measurements outside the grey zones correspond to cloud free soundings. 87

5.11 Layer optical depth of CloudSat for the entire cross-section with OLCI on the 12^{th} of June 2016. 88

5.12 Comparison of heights for cloud top (left), bottom(middle) and mode(right) between CloudSat and OLCI for three different OLCI retrieval runs. . . 89

6.1 CERES field of view. δ' is the along-scan angle, β the cross-scan angle and indices f and b denote the forward and backward boundaries. From Green and Wielicki (1997). 95

6.2 Shortwave TOA flux comparison for the annual averages of 2008: On the right column are diurnally corrected flux estimates, on the left without correction. From top to bottom are shown the: (1) Cloud CCI MODIS product (2) CERES SSF1deg (3) Cloud CCI MODIS – CERES SSF1deg. 97

6.3 Longwave TOA flux comparison for the annual averages of 2008: On the right column are diurnally corrected flux estimates, on the left without correction. From top to bottom are shown the: (1) Cloud CCI MODIS product (2) CERES SSF1deg (3) Cloud CCI MODIS – CERES SSF1deg. 99

6.4 Shortwave TOA flux comparison between ESA CCI and CERES SSF. The presented scene is from the 20th of February 2008, covering the southern part of Greenland. 101

6.5 Shortwave TOA flux comparison between ESA CCI and CERES SSF. The presented scene is from the 20th of March 2008, above central Africa. . 102

A.1 Sensitivities of TOA radiances depending on the vertical distribution of cloud optical depth for a cloud with $ctp = 700hPa$, $\tau = 10$, an vertical extent $ext = 200$ and an underlying surface albedo of $\alpha = 0.02$ for channel ratios 13/12 (left), 14/12 (middle) and 15/12 (right). 110

A.2 Sensitivities of TOA radiances depending on the vertical distribution of cloud optical depth for a cloud with $ctp = 700hPa$, $\tau = 10$, an vertical extent $ext = 200$ and an underlying surface albedo of $\alpha = 0.6$ for channel ratios 13/12 (left), 14/12 (middle) and 15/12 (right). 110

A.3 Sensitivities of TOA radiances depending on the vertical extent of a cloud with $ctp = 700hPa$, $\tau = 10$, an mode of $moi = 0.6$ and an underlying surface albedo of $\alpha = 0.02$ for channel ratios 13/12 (left), 14/12 (middle) and 15/12 (right). 111

A.4 Sensitivities of TOA radiances depending on the vertical extent of a cloud with $ctp = 700hPa$, $\tau = 10$, an mode of $moi = 0.6$ and an underlying surface albedo of $\alpha = 0.6$ for channel ratios 13/12 (left), 14/12 (middle) and 15/12 (right). 111

A.5 Sensitivities of TOA radiances depending on the vertical distribution of cloud optical depth for a cloud with $ctp = 200hPa$, $\tau = 10$, an vertical extent $ext = 200$ and an underlying surface with $\alpha = 0.02$ (left) and $\alpha = 0.6$ (right). 112

A.6 Degrees of freedom for a measurement of a cloud with $\tau = 100$ and surface albedo $\alpha = 0.01$ depending on the central wavelength of the OLCI channels as well as the cloud top pressure. The degree of freedom is presented for different combinations of cloud vertical extent and mode of optical depth. 113

A.7 CloudSat (orange circles), MODIS (purple dashed line) and OLCI (green dashed line) cloud optical depth as retrieved for the studied scene between latitudes of 77° and 77.5°. Here, the compared MODIS pixel is shifted by 3km westwards. Grey areas mark a significant difference in *COD* between OLCI and A-train for the unshifted case. 114

A.8 2-D histograms of classification into groups seperated by k-means clustering (left), mode (middle) and extent(right) for scenes above snow covered surface. Presented is the classification accuracy of each class. . 114
A.9 2-D histograms of classification into groups seperated by k-means clustering (left), mode (middle) and extent(right) for scenes above vegetated surface. Presented is the classification accuracy of each class. . . 115
A.10 2-D histograms of classification into groups seperated by k-means clustering (left), mode (middle) and extent(right) for scenes above desert surface. Presented is the classification accuracy of each class. 115

List of Tables

2.1 Operational spectral bands of Sentinel-3A OLCI. Taken from https://sentinel.esa.int/web/sentinel/user-guides/sentinel-3-olci/overview/heritage/. 14

3.1 Summary of the changes in each parameter underlying the calculated sensitivities. 30
3.2 Simulation points for MOMO as basis for the OLCI cloud parameter retrieval. Every permutation of the shown grid points was used for a simulation. 32
3.3 State- and measurement vector of the OLCI cloud property retrieval. . 41

4.1 Feature importance for the previously found optimal set of window size, inter-pixel distance and grey-levels. Each feature importance is normalized. The highest and lowest feature importance of each band is presented in bold. 59
4.2 Classification accuracy of individual classes and total for k-means clustered and manually clustered data points. 63
4.3 Classification accuracy of individual classes and total for k-means clustered and manually clustered data points for the three studied surface types. 67

5.1 Probability of detection, false alarm rate and Hanssen-Kuipers skill score for FAME-C cloud fraction related to the CloudSat/CALIOP measured cloud fraction. 75
5.2 A priori state and error co-variance for the three different cloud top retrievals based on OLCI measurements. 82

6.1 All-sky correction factor for short- and longwave to account for the diurnal cycle in TOA flux (personal correspondence with Martin Stengel). 96
6.2 Surface types as used in the CERES retrieval. Surface types 1-17 correspond to those defined by the INternational Geopshere-Biosphere Programme (IGBP) 100

Danksagung

Ich möchte zunächst Prof. Dr. Jürgen Fischer danken, dass er mir ermöglicht hat meine Doktorarbeit am Institut für Weltraumwissenschaften anzufertigen, mir großartige Forschungsaufgaben erteilt hat und mich in meiner Zeit am Institut stets mit Rat und Tat unterstütze. Außerdem, möchte ich Prof. Dr. Ralf Bennartz danken für seine Hilfe an meiner Arbeit, seine wunderbare Vorlesung über Wolkenphysik und für die Übernahme des Zweitgutachtens dieser Dissertation. Vor allem geht mein Dank an René Preusker und Cintia Carbajal Henken, ohne deren Beistand diese Arbeit nicht möglich gewesen wäre. Natürlich danke ich auch allen anderen Kollegen für ihren Rat und die sehr willkommen Ablenkungen in anstrengenden Zeiten durch Kaffeepausen, Magnarts und Darts. Ich werde die Zeit mit euch allen sehr vermissen.